Università degli Studi di Napoli *Federico II*

Università di Camerino

DOTTORATO DI RICERCA IN QUANTUM TECHNOLOGIES

Ciclo XXXIV

Coordinatore: prof. Francesco Tafuri

Quantum Technologies with 2D- oxide materials

Settore Scientifico Disciplinare FIS / 03

Dottorando
Maria D'Antuono

Tutore
Prof. Daniela Stornaiuolo

Anni 2018/2022

Abstract

In the recent years, the continuous advancements in oxide thin films epitaxial growth and characterization techniques led to the possibility of design and control complex oxide heterointerfaces and characterize their crystal and electronic structure with atomic precision. These advancements brought to light a wealth of properties for oxide heterointerfaces and opened to new opportunities for oxide electronics and spintronics. Now the research on oxide interfaces is expanding outside the pure material science realm, entering the field of application-oriented devices.

In this thesis, the innovative and intriguing functionalities arising in an oxide system where Rashba spin-orbit coupling, magnetism, superconductivity and high-mobility are combined in the same two dimensional electron gas (2DEG) have been reported. The focus of my work has two main aspects: on one side, to study the interplay between the several ground states in the 2DEG at the $LaAlO_3/EuTiO_3/SrTiO_3$ interface; on the other, to realize nanodevices which will make these phenomena functional for new quantum electronics with advantages like scalability, easy top-down processing and possibility to manipulate the 2DEG system with unprecedented control.

AUTHOR'S DECLARATION

I declare that the work in this dissertation was carried out in accordance with the requirements of the University's Regulations and Code of Practice for Research Degree Programmes and that it has not been submitted for any other academic award. Except where indicated by specific reference in the text, the work is the candidate's own work. Any views expressed in the dissertation are those of the author.

SIGNED: ..... DATE: 09/03/2022

TABLE OF CONTENTS

PREFACE

In the latest years, with the increase in computational power and the ongoing miniaturization of electronic devices, researchers are beginning to contend with the material restrictions of silicon-based device technology. Metal-oxide-semiconductor field-effect-transistors can now be realized in the 7 nm regime; however scaling the devices channel even further will cause drain-induced barrier lowering, decrease of the threshold voltage and hot carrier effect, with a significant degradation of the devices performances. As the scaling approaches its technical and physical limits, researchers have been looking for new device configurations, alternative materials and also radically new operating principles. While traditional silicon electronics will remain dominant in consumer industry, alternative trends are emerging.

A promising approach to reduce power consumption and to increase processing capabilities is, for instance, spintronics, which involves controlling the spin of electrons or holes instead of their charge. In spintronic devices, the spin polarisation is controlled either by magnetic layers used as spin-polarisers or via spin–orbit coupling. Spin waves can also be used to carry spin current.

Transition metal oxides can play an important role in future electronics and spintronics. This class of materials is characterized by a large variety of properties which are extremely sensitive to electronic correlations, crystal symmetry and chemistry. Also the simplest binary monoxides exhibit a broad range of behaviors from insulating to metallic, magnetic, and even superconducting. These aspects open the way for the realization of all-oxide-based new electronic platform.

Purpose of this thesis

This PhD thesis is focused on the study of two-dimensional electron gas formed at the interfaces between transition metal oxides (oxide-2DEG) in the view of quantum applications and in spintronics.
In particular, I studied the heterostructure created by depositing a $LaAlO_3$/ $EuTiO_3$ bilayer on a $SrTiO_3$ single crystal (LAO/ETO/STO). As its "parent heterostructure" LAO/STO, LAO/ETO/STO shows, among other properties, superconductivity, Rashba SOC and photoconductivity. However, the addition of a delta doping layer of ETO introduces also spin polarization of the carriers.
The application of this ferromagnetic oxide 2DEG to advanced electronics requires the creation of suitably designed nanodevices. We will present a new nanofabrication technique and demonstrate its feasibility for the realization of high efficiency electric field devices, where all the mentioned properties can be tuned using a gate voltage in the hundreds of milliVolt range. We will also discuss the response of this 2DEG to visible and infrared light.

The long-term goal of the work is to establish the ground for a new electronic platform based on oxide two dimensional electron gas systems (2DEG), with advantages like scalability, easy top-down processing and possibility to control and manipulate quantum states using the gate voltage and light, in order to access new scenarios and opportunities in quantum technologies.

Organization of this thesis

The present thesis is organized in five chapters.

- Chapter 1 contains an introduction to oxide 2DES, with particular attention to LAO/STO, and a discussion of the potential applications of transition metal oxides interface for new quantum devices.

- Chapter 2 reports the electrical transport properties of the LAO/ETO/STO 2DEG. In particular, we focus on properties of interest for new small-scaled electronic devices where spin, charge and orbital correlations are involved.

Detailed characterization of Rashba spin-orbit coupling (SOC) and of ferromagnetic effects and their interplay is presented.

- Chapter 3 describes a novel nanofabrication technique for oxide interfaces patterning and the experimental results obtained by transport analysis of such nanodevices.
- Chapter 4 presents the study of the combined effect of visible light and electric field for the tuning of LAO/ETO/STO based devices. In particular, we show the possibility to tune magnetic correlations using light.
- The summary of the thesis work and future perspectives are discussed in the conclusive chapter.

CHAPTER 1

INTRODUCTION

1.1 Overview of oxide interfaces

In his Nobel lectures Herbert Kroemer famously claimed that "the interface is the device", referring to semiconductor interfaces that have been playing a crucial role in modern electronic and optoelectronic devices in the last 40 years [1].

Indeed, at the interface where two layers of different materials meet, a physics more complex than that of the single materials can arise. The interfaces between different semiconductors in modern transistors are at the base of our "Silicon Age", as they represent the nucleus of actual microelectronics. However, the current race to miniaturization is quickly approaching the fundamental physical limits of silicon based electronic devices.

A possible way to overcome the silicon limit is to use new materials and new operating principles. In this work, we focus on transition metal oxides (TMOs). As bulk, these materials present some spectacular phenomena as giant magnetoresistance, high-temperature superconductivity, ferroelectric and multi-ferroic behaviors, large-scale thermoelectric and magnetocaloric effects, resistive switching and many others. When an interface between two TMOs is created, the interplay

among the various properties leads to the creation of new and exciting properties and possibilities for electronic devices. Interfaces between TMOs are therefore another example of the richness of physics at the interface, as Kroemer observed. The rich physics of TMOs derives from the several interacting degrees of freedom (charge, orbital, spin and lattice) which can be controlled via several stimuli, as reported schematically in Fig. 1.1.

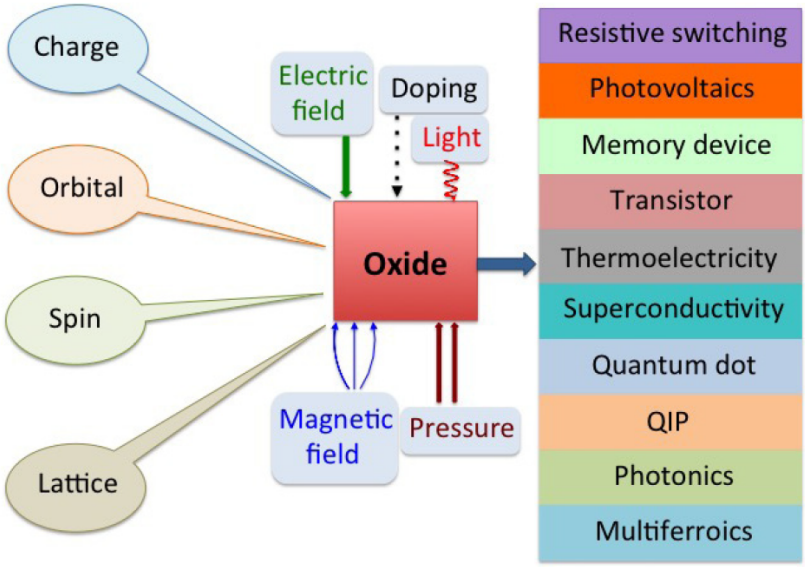

Figure 1.1: Graphical description of various interacting degrees of freedom, external controls and technological aspects of complex oxides [2]

Oxide (hetero)interface physics is dominated by electronic bands with a d orbital character. The large Coulomb repulsion between electrons located in these spatially confined orbitals, U, tends to block the motion of electrons from one atom to another, and can induce strongly correlated states, depending on the electron filling. At the interfaces, the breaking of inversion symmetry and the confinement effects add to this picture. Compared to semiconducting interfaces, transition metal oxide interfaces are characterized by strong confinement effects, due to a reduced electronic screening (~ 1-10 nm). As a consequence of aforementioned interaction new electronic, magnetic and orbital phases are generated at the interfaces of oxide heterostructures, which are very different from the bulk.
Moreover, in oxide heterointerfaces important modification of the atomic arrangements with respect to the bulk are induced. An example is the buckling of the

transition-metal-oxygen bonds and modification of the TiO_6 octhaedra rotation patterns, that sensibly influence the band ordering, for example, or even the band-symmetry in some case, affecting emerging macroscopic physical properties. As an example, we consider the $LaMnO_3/SrMnO_3$ system, where both oxides are, separately, antiferromagnet (AFM) insulators at low temperatures, while at the interface a charge transfer occurs resulting in ferromagnetism with in-plane spin alignment. Another example is represented by mixed-valence manganese (Mn) oxides, denoted by the general formula $RE_{(1-x)}D_xMnO_3$ (where RE stands for trivalent lanthanides or rare earth elements such as La, Pr, Nd and D for divalent alkaline Ca, Sr, Ba), that offer diverse phase-space structures and exciting transport properties with varying doping concentration x. Another intriguing system is the interface between insulating La_2CuO_4 and metallic overdoped $(La,Sr)_2CuO_4$. At the interface between the two materials, superconductivity is established via charge transfer. In complex oxide interfaces, unlike semiconductor compounds, all these phenomena are confined on scale of few nm near the interface, creating systems which have a two-dimensional nature. Furthermore, electrostatic doping can alter the fundamental properties of these electronic system. For example a tuning of the magnetic or superconducting transition temperatures can be achieved by electric field effect, and in some cases even phase transitions, like superconducting to insulator transitions.

Thanks to all these features, oxide 2DEG systems are viewed as promising candidates for future quantum electronics.

In the next paragraph we will briefly introduce one of the most popular oxide interface: the LAO/STO heterostructure. Among its many properties, we will focus on those of interest for quantum applications. After that, in paragraphs 1.3 and 1.4, we will describe recent experiments involving STO-based interfaces, highlighting the great progress made in the latest years in the understanding and manipulation of quantum effects in these materials.

1.2 Formation of a 2DEG at the LAO/STO interface

The properties of $SrTiO_3$ (STO) have fascinated researchers for generations. This simple perovskite material indeed shows superconductivity via doping, ferroelectricity, piezoelectricity (fig.1.2). Interest in the fundamental properties of STO was renewed recently thanks to the discovery, in 2004, of the possibility to create a two dimensional electron gas (2DEG) by depositing a thin layer of $LaAlO_3$ (LAO) on a TiO_2-terminated STO [4]. Both materials are band insulators, with band gaps of 5.6eV for LAO and 3.25eV for STO. STO is a non-polar material arising from stacking of the neutral sublayers $(SrO)^0$ and $(TiO_2)^0$ with no intrinsic charge dipole, while the LAO is composed of charged LaO^{+1} and AlO_2^{-1} layers. When a thin film of LAO is grown, in a layer-by-layer fashion, on a TiO_2 terminated $SrTiO_3$ single crystal, a potential between the higher surface and the interface builds up. This potential increases with LAO layer thickness. The divergence in potential is prevented by transferring an half electron per unit cell ($e/2$ per u.c.) from LAO to STO across the interface [5], generating a confined conducting layer. This mechanism is known as "polar catastrophe". The main proof of the validity of the polar catastrophe model comes from the observation that a minimun layer of 4 u.c. of LAO is required to induce conductivity at the LAO/STO interface. This value matches exactly with the calculated potential value required for the ignition of

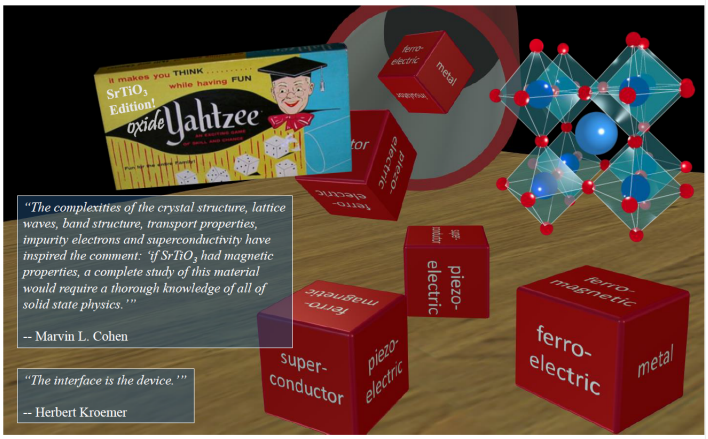

Figure 1.2: Summary of the main properties of $SrTiO_3$. Adapted from [3].

the electron transfer to the interface [6]. Another elegant confirmation of the polar catastrophe effect comes from the experiment reported in Ref. [7], where pure LAO was replaced by $(LaAlO_3)_x(SrTiO_3)_{1-x}$ (LASTO:x, i.e. LAO diluted with STO) with different values of x. In agreement with the polar catastrophe model, in this work the critical thickness for the 2DEG formation is found to scale with x.
While the polar catastrophe model is valid for crystalline LAO layers, it is also found that the interface between amorphous LAO (a-LAO) and STO can host a 2DEG [8–10]. However, in this case, the mechanism for interface conduction is related to the the doping of the topmost layers of STO via generation of oxygen vacancies, due to outward diffusion of oxygen from the substrate to the oxygen-deficient amorphous overlayer [9].

1.2.1 Band structure

In the LAO/STO 2DEG the transition metals atoms are surrounded by six O^{2-} ions and the crystal field has cubic symmetry. The cubic crystal field splits the five d orbitals into a two-fold degenerate subset, an upper energy band $e_g \equiv (d_{x^2-y^2}, d_{z^2-r^2})$ and a three-fold degenerate subset, $t_{2g} \equiv (d_{xy}, d_{yz}, d_{xz})$. Since the t_{2g} triplet is 2eV lower than the e_g doublet, it defines the conduction band minimum. At the interface the t_{2g} states degeneracy is lifted due to the perpendicular confining

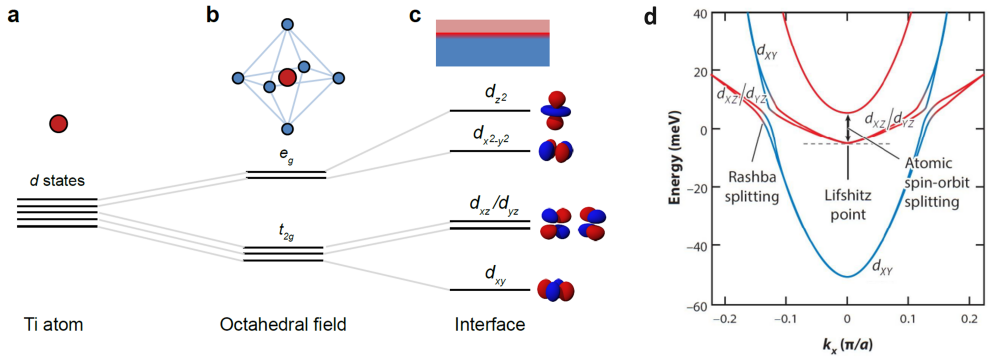

Figure 1.3: Energy levels of the Ti 3d orbitals. **a)** Isolated Ti atom. **b)** Octahedral field from a cubic perovskite. **c)** Interface: non inversion-symmetric tetragonal environment. 3d orbitals of Ti split into a less energetic triplet $t_{2g} \equiv (d_{xy}, d_{yz}, d_{xz})$ and more energetic doublet $e_g \equiv (d_{x^2-y^2}, d_{z^2-r^2})$. **d)** Band diagram including the Rashba SOC effect.

electric field (fig. 1.3). In Ref. [11] the splitting energies of the t_{2g} states was measured to be ≈ 50 meV. In summary, close to the Fermi level, the conduction band results from the overlap of the Ti-3d orbitals: the lower in energy has a $3d_{xy}$ character (with a light effective mass in the in-plane directions), while $3d_{xz,yz}$ orbitals lie higher in energy and present dispersion along the out-of-plane direction.

The band diagram described above offers the opportunity to obtain multi band transport. Electric field effect changes the carrier density shifting the Fermi level. It is possible, therefore, to change the occupancy from one-band (the d_{xy} band) to two-band (the $d_{xz/yz}$ bands) [12, 13]. The capability to control the physical properties of 2D system by applying an external electric field is of crucial importance for device applications, as it will be discussed in more details in Chapter 3.

1.2.2 Spin-orbit coupling

Another important ingredient of the physics of confined heterostructures, like the LAO/STO 2DEG, is the presence of spin-orbit coupling (SOC).
The SOC enters into the Hamiltonian of system as a relativistic correction to the Schrödinger equation, giving the SO term [14]:

$$H_{SO} = -\frac{\hbar}{4m_e^2c^2}\vec{\sigma}\cdot\vec{p}\times\vec{\nabla}V \tag{1.1}$$

where V is the electric potential of the atomic structure, $\vec{p}$ is the kinetic momentum, $\vec{\sigma} = (\sigma_x, \sigma_y, \sigma_z)$ is the vector of Pauli spin matrices, c is the speed of light, m_e is the mass of a free electron and $\hbar$ is the Planck constant.
For condensed matter systems, electrons move in a crystal potential and SO coupling arises when there is a potential gradient on average. There are usually two types of SO couplings: the first one is the Dresselhaus SO coupling which originates from the bulk inversion asymmetry (BIA), for instance in zinc blende structures, such as such as GaAs or InSb [15]. The second one is the Rashba SO coupling which is due to the structure inversion asymmetry (SIA) in quantum wells and two-dimensional electron gases [16].

In $SrTiO_3$-based oxide interfaces, the built-in electric field, $\vec{E} = E_z\vec{z}$, breaks the symmetry between the z and $-z$ direction, resulting in a Rashba SOC of the form:

(1.2) $$H_R = \alpha_R (z \times \vec{k}) \cdot \vec{\sigma}$$

where the Rashba coefficient α_R quantifies the strength of the effect. For each value of k, the eigenvalues and the energies of two spin-split bands, with opposite spin orientations are:

(1.3) $$E_{\uparrow,\downarrow}(k) = \frac{\hbar^2 k^2}{2m^*} \pm \alpha_R k$$

where k is the wavevector and m^* is the effective mass. The spin texture at the Fermi surface is plotted in Fig.1.4 a).
The spin polarization is always perpendicular to k and electrons have opposite spins. From this, a momentum dependent splitting of the two spin subbands arises, with a shift of $k_R = \pm \alpha_R m/k^2$ as illustrated in Fig. 1.4 a) for $\alpha_R > 0$. Performing a cut in the band structure at an arbitrary energy, we observe that this splitting leads to two nonequivalent Fermi contours with clockwise and counter-clockwise rotation of the spin in the k_x, k_y plane.

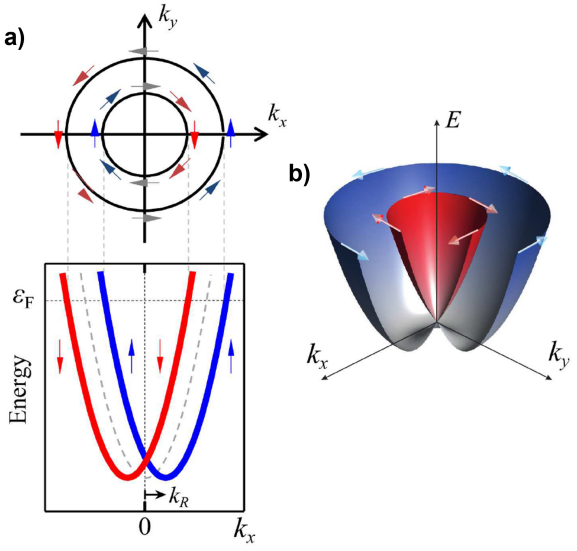

Figure 1.4: Band dispersion of a nearly free two-dimensional electron gas due to Rashba SO coupling. a) Top: At the Fermi level, the spins are locked to their momenta and counter-propagating electrons have opposite spins. Bottom: Energy dispersion for Rashba-split bands with opposite spin configurations. b) 3D representation of the band structure.

When SOC is added to the band diagram of LAO/STO, two peculiar characteristics are generated: a small spin splitting at the bottom d_{xy} band [17] and stronger splitting near the band crossing between the d_{xy} and $d_{xz/yz}$ bands, as supported by theoretical calculations and angle-resolved photoemission (ARPES) measurements [13, 18, 19] (Fig. 1.3 d). As a consequence, by modulating the Fermi level across the the different types of bands using electric field effect, the opportunity of tuning also the SOC in LAO/STO system arises.

1.2.3 Superconductivity

A few years after its discovery, the 2DEG at LAO/STO interface was found to be superconducting. The superconducting state is tunable by the gate voltage [21–23] (Fig. 1.5a)): increasing the gate voltage (electron density) produces first a rise of the critical temperature T_c, and for larger voltages, T_c decreases again, forming a dome-like superconducting region similar to that found for high temperature superconductors, with “underdoped” and “overdoped” regions [24] (Fig. 1.5 d)). Results on the critical magnetic fields reported an anisotropy for external perpendicular

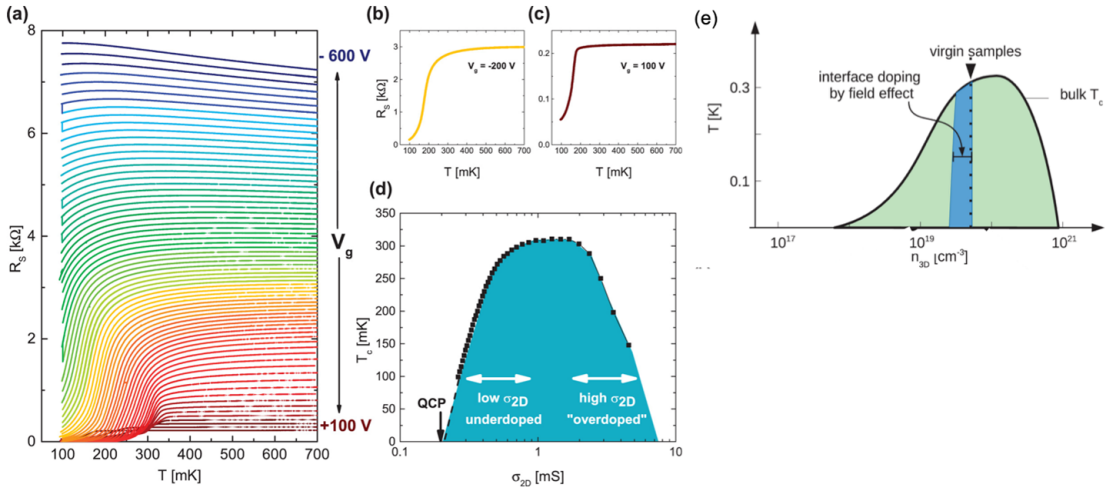

Figure 1.5: Superconducting phase diagram of LAO/STO.(a) Sheet resistance R_s versus T, upon different gate voltages (V_g). By changing V_g the critical temperature can be reduced (“depletion” state—blue curves), reaches its maximum value close to the original doping state (red curves), and decreases again (accumulation state—brown curves). Superconducting transitions for an underdoped (b) and an overdoped state (c). (d) Superconducting dome plotted vs the sheet conductance σ_{2D} (e) Superconducting dome in bulk STO (black line—green area) and LAO/STO interfaces (blue area). Adapted from Ref.[20]

and parallel magnetic fields $H_{//}c/H_{\perp}c \sim 20$ [25]. This allows to estimate a thickness of the superconducting layer at the LAO/STO(001) interface of about 10 nm, which further confirms the 2D nature of the superconductivity at the interface.
The details of superconductivity in this system, as for instance the symmetry of the order parameter, are still under debate. Firstly, we point out that in doped STO the superconducting phase develops at very low density and is stable over a wide doping range. On the other hand, at the LAO/STO interface, the superconductivity develops only over a limited carrier density range (Fig. 1.5 e)). Moreover, the combination of 2D superconductivity and Rashba SOC in LAO/STO supports the hypothesis of unconventional superconductivity [26–30], involving a complex order parameter and a possible combination of singlet and triplet spin components. Several experimental works indeed highlight unconventional superconducting effects in LAO/STO [31, 32]. In particular, in Ref. [33] the analysis of Josephson effect in LAO/STO nanoconstrictions show the presence of two superconducting gap-structures and of an unconventional superconducting channel, in parallel with a conventional one.

1.2.4 Magnetism

Despite the fact that both LAO and STO are non magnetic, there are many reports of magnetic phenomena in LAO/STO. In 2007 by Brinkman et al. [34] measured a sizable hysteresis in the magnetoresistances of LAO/STO samples and an upturn in the resistance versus temperature curve, at low temperatures. The latter behavior was attributed to Kondo effect due to magnetic impurities. Other signatures of magnetism observed are anisotropic magnetoresistance [35], direct observation of magnetization with cantilever torque magnetometry [36], anomalous Hall effect [37]. Local magnetic signals were also reported using scanning squid magnetometry [38]. The origin of these magnetic signals, however, is still debated. They could indeed be due to both intrinsic and extrinsic effects. The former includes localized carriers [39] and itinerant ferromagnetism [40]. On the other hand, extrinsic mechanisms can be linked to Sr vacancies [37], Al vacancies [41] and oxygen vacancies [42]. However a recent methodological work performed with various techniques concluded that intrinsic mechanisms are unlikely to create magnetic

effects in LAO/STO [43], while the presence of oxygen vacancies seem to account well for the phenomenology observed in the system [11].

1.3 Towards quantum nanotechnologies based on oxide 2DEG systems: state of art of nanopatterning methods and results

In the previous paragraphs we showed how oxide interfaces combine semiconducting and correlated materials properties, bringing many novel effects, able to provide capabilities not present in other solid-state platforms. In this paragraph we illustrate how some of these effects have been exploited for the formation of novel devices of interest for quantum electronics. In particular, we focus on results obtained on LAO/STO.
In spite of several challenges, in the last few years, the advancements in the nanofabrication methods allowed the realization of several types of oxide interfaces-based nanodevices. The wide range of nanodevices realized includes nanowires, nanoscale photodetectors, THz emitters and detectors, tunnel junctions, field-effect transistors, diodes, single-electron transistors, superconducting nanostructures, josephson junctions, quantum dots and quantum nanostrictions [17, 44–46].
Figure 1.6 shows a selection of them.

- By using conductive atomic-force microscope (c-AFM) technique on LAO/STO very narrow (< 10nm) channels can be "written" on the 2DEG. The group of Jeremy Levy in at the University of Pittsburgh, in particular, realized a series of exciting experiments, from the demonstration of ballistic transport in electron wave guides [47], to the realization of one dimensional superlattices, where the 1D structures can be "written" with the desired dimensions, spacing etc. This excellent level of control over 1D structures opens intriguing perspectives for the simulation of quantum systems [51] (Fig. 1.6 a)).

- Superconductivity at the nanoscale was investigated in several types of nanodevices including nanobridges [52], Dayem bridges [33], side-gate nanochannels [53] and Superconducting quantum interference devices (SQUIDs) [48].

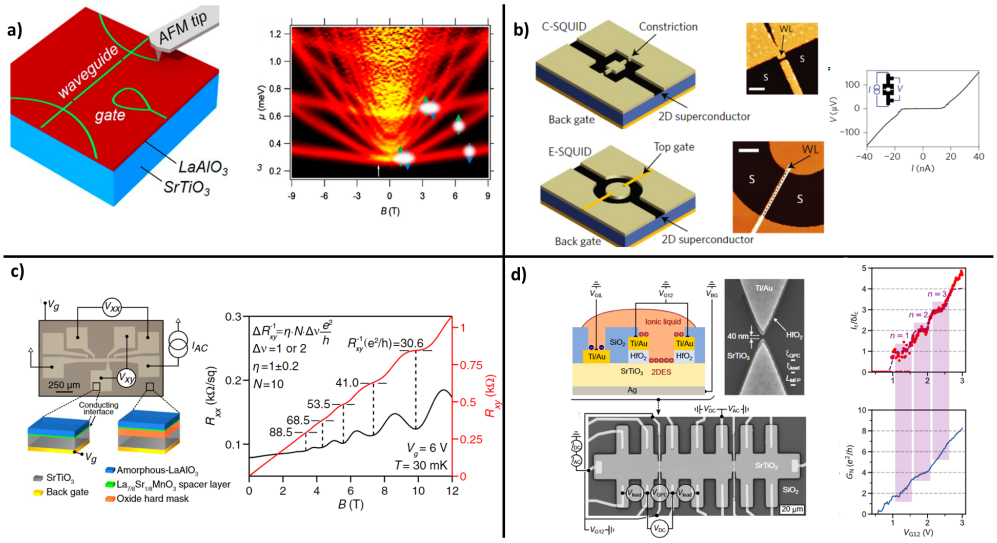

Figure 1.6: Example of quantum oxides nanodevices. a) Electron waveguides obtained with c-AFM, [47]. b) Back-gate and Top-gate SQUIDs device, adapted from [48]. c) Shubnikov–de Haas oscillations in longitudinal R_{xx} and quantized Hall resistance in a-LAO/LSM/STO [49]. d) Superconducting quantum point contacts with quantized critical supercurrent, tunable between zero and three ballistic modes by split gates [50].

The latter are shown in Fig. 1.6 b). In that case, the two junctions composing the SQUID were independently tuned via electric field effect, allowing for an exceptional control of the devices properties.

- Quantized Hall resistance, with integer step size, was observed in a STO-heterointerface. Quantized Hall effect generally requires materials with high carrier mobility, such as semiconductor heterostructures based on silicon and III-V compounds. In these systems, the conducting states derive from sp hybrid orbitals with a covalent bond nature. In contrast, the interface conductivity in STO-based heterostructures originates from less overlapping Ti 3d orbitals, where the resulting ionic bonds lead to a strong coupling between the lattice, charge and spin degrees of freedom, as described in the previous paragraph, and is usually characterized by a lower mobility. In Ref. [49] the authors introduce a thin layer of $La_{7/8}Sr_{1/8}MnO_3$ (LSM) between LAO and STO to modify the band structure of the 2DEG and increase the carriers mobility (Fig. 1.6 c)). This experiment is a beautiful example of the possibility to engineer complex oxide interfaces to modify their fundamental properties.

- By using nano-patterned top-gates directly deposited on the LAO dielectrics, confined structures can be realized. Using this method, recently, quantization of the conductance and ballistic Quantum Point Contact (QPC) LAO/STO devices were realized as shown in ref. [54], while superconducting critical current quantization was demonstrated in STO-based interface QPC devices in ref. [50] (Fig. 1.6 d)).

In summary, recent experiments on oxide 2DES show that these materials are a promising platform for the realization of quantum devices, with advantages like scalability and possibility to control and manipulate the quantum states using just the electric field effect in several possible configurations (back gate, split gate, ion liquid etc, see Chapter 3).
In the following paragraph we will focus on the additional possibilities offered by the presence, in these materials, of a sizable spin-orbit coupling.

1.4 Exploration of Spin-Orbit Coupling in oxide 2DES for spintronic devices

The use of the spin degree freedom of electrons for applications such as information storage and computing is at the heart of spintronics. Conventional spintronic devices exploit the exchange interaction between conduction electron spins and local spins in magnetic materials to create spin-polarized currents or to manipulate nanomagnets by spin-transfer from spin-polarized currents [55]. The most important spintronic device developed in the last decade is the spin-valve, made of multilayers composed by alternating ferromagnetic and non-magnetic conductive layers.
A novel route of spintronics makes use the spin-orbit coupling (SOC), instead of the magnetic exchange interaction, to generate, manipulate and read-out spin-polarized currents. This involves the interplay between charge and spin currents via spin-to-momentum coupling. SOC is the only effect able to link the electrical and magnetic properties. The many interesting phenomena and possibilities arising at oxide interefaces thanks to the presence of SOC are sketched in Fig. 1.7.

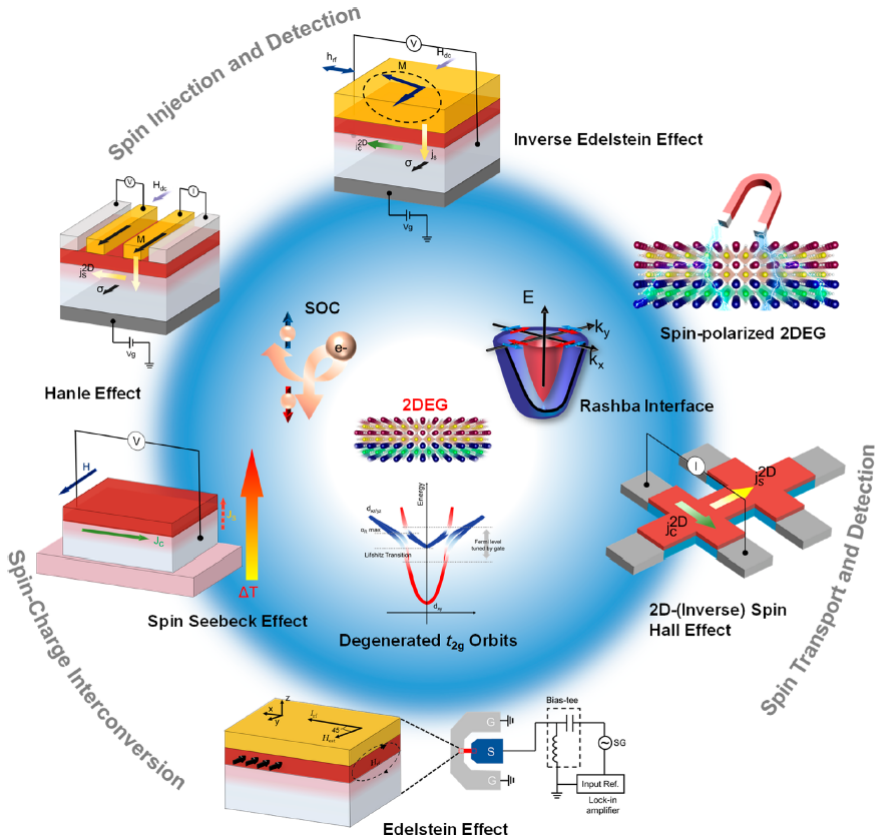

Figure 1.7: Schematic diagram of perspectives for Rashba spin-orbit coupling at oxides interfaces [56].

In the previous paragraph, we briefly discussed the Rashba SOC at the LAO/STO interface. Rashba SOC attracted great attention when Datta and Das proposed the idea of the spin transistors [57]. In these devices, the spins could be controlled during their passage from source to drain applying an electric field via the gate voltage. This effect induces a certain amount of spin precession over the length of the channel, which controls how effectively the electron can exit through the drain contact, leading to a change in resistance. As result, a low (high) resistance can be thought of as an on (off) state. The recent discovery of efficient spin-to-charge interconversion is a first step towards the application of this paradigm to oxide 2DEGs, which has attracted also the interest of companies such as Intel, IBM and Thales.

For the Rashba effect in oxides interface, the spin degeneracy is lifted, leading to concentric Fermi contours with opposite spin chirality. This gives two different

spin- to- charge conversion mechanisms (Fig. 1.8):

- **the direct Edelstein effect** A current injected along x induces a shift of the Fermi contour, generating a spin accumulation along y. This spin accumulation can diffuse towards a neighboring ferromagnetic layer, thus generating a spin current.

- **the spin Hall effect** A displacing of the Fermi contours of Δk generates a transverse spin accumulation along the perpendicular direction. This spin accumulation can start to precess around to local Rashba field to eventually align along the new spin direction. While precessing, the spins acquire a finite component along $+z$ for $k_y > 0$ and $-z$ for $k_y < 0$. The charge current applied along x thus results in the motion of electrons with opposite spins in opposite directions, i.e., in a pure spin current with a spin polarization along z.

The inverse Edelstein effect has recently been demonstrated in STO-based heterostructures [58, 59]. In these works, the injection of spin current into 2DEG

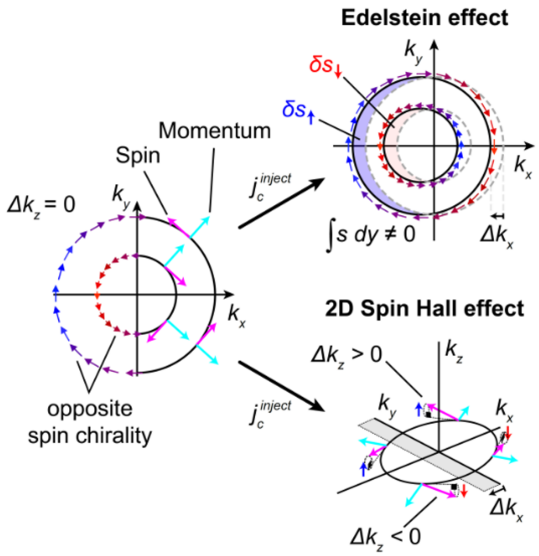

Figure 1.8: Rashba–Edelstein effect and 2D spin Hall effect

at oxides interfaces is obtained by spin pumping. For example, in Ref. [58] an external magnetic field together with radiofrequency microwaves are applied to

a ferromagnetic NiFe layer deposited on top of a LAO/STO heterostructure. In this case, the quality of the interface between the ferromagnetic film and the LAO film plays a key role in the injection of polarized carriers. When the ferromagnetic resonant condition is achieved, a pure spin current is ejected from the NiFe layer and injected into the adjacent 2DEG due to the diffusion of the accumulated spins (Fig. 1.9 a)). This spin-polarized current is then transformed into a charge current thanks to the Rashba SOC in LAO/STO, producing a lateral interfacial charge current density.

Inverse spin Hall effect has also been demonstrated in LAO/STO devices [60, 61] (Fig. 1.9 b)). An Hall-bar geometry was employed to generate a transverse spin polarized current, which in turn was detected by the inverse spin Hall effect. The observed spin precession signatures clearly demonstrated the nonlocal spin diffusion as well as effective spin charge conversion at this oxide heterointerface. A further

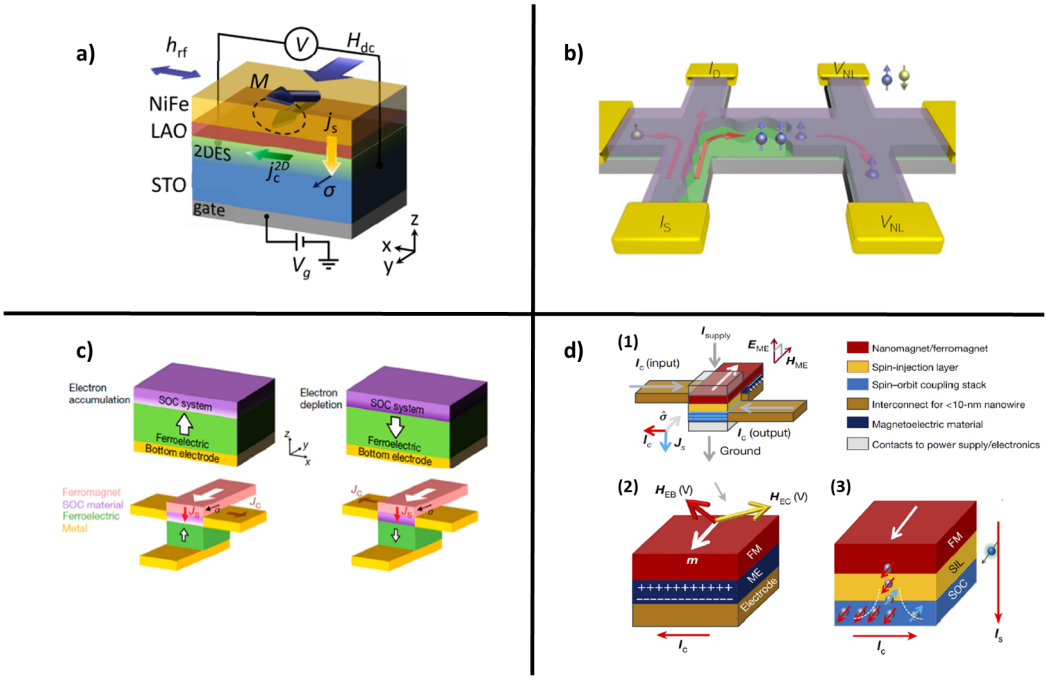

Figure 1.9: a) Configuration of the device used for the injection of a spin-polarized current into 2DEG [58] b)Schematic of spin Hall induced nonlocal spin diffusion and its measurement configuration [61], c) Basic concept of the conversion between spin current and charge current supported by ferroelectric material [62]; d) MESO device for charge-based logic computing. (1) the scheme of structure, (2) the node for magnetoelectric switching of magnetism, and (3) the node for spin-to-charge read-out [63].

advancement of these experiments can be obtained by incorporating ferroelec-

tric materials in oxide 2DEG. This addition leads to a non-volatile spin-to-charge conversion effect [62], paving a new way to low-power-consumption non-volatile spinorbitronics devices (Fig. 1.9 c)).
Recent work by Intel Corporation uses the magnetoelectric coupling to achieve the spin–charge interconversion. The magnetoelectric coupling induces a change in electric polarization with an applied magnetic field, or conversely a change in magnetization with an applied electric field. Combining this effect with SOC, a magnetoelectric spin–orbit (MESO) device is obtained, with promising applications for charge-based logic computing [63]. The MESO device sketched in Fig. 1.9 d) presents two inverters: the first node converts the input current into the magnetization of the ferromagnet and the second node converts the spin polarized current injected from the ferromagnet into charge accumulation via SOC with an output current. The output current can also be used as the input current for the next device, and consequently, a cascade logic device could be obtained.
All these devices briefly described allow for the interconversion of the electric and magnetic signals with high efficiency and low power consumption [56, 62, 64–66].
We finally point out that, as demonstrated in this paragraph, ferromagnetic and antiferromagnetic materials represent an important ingredient in spintronic devices. In the next chapters of this thesis, we will demonstrate that magnetic coupling can be added to oxide 2DEG.

1.5 Conclusions

In the last few years there were tremendous advancements in the field of oxide 2D systems. In this chapter we briefly discussed several experiments, mostly realized using oxide 2DEG based nanodevices, which highlight their great potential for advanced electronics and quantum applications. We also discussed the emerging field of spin-orbitronics, where the spin-degrees of freedom are manipulated with electric fields through the spin-momentum locking of the electrons. Further promising applications of oxide 2DES include high efficiency transistors [53, 67], photonic and high frequency applications [68, 69].
In the following chapters of this work we will introduce the properties of an oxide 2DEG system which combines the already discussed properties of LAO/STO (i.e.

superconductivity, Rashba SOC, tunability with electric field effect) with magnetic coupling. We will present theoretical and experimental characterizations of this system, and a novel nanofabrication technique, which will open the way to the exploitation of its interesting properties for quantum applications.

CHAPTER 2

PROPERTIES OF THE SPIN-POLARIZED 2DEG AT THE LAO/ETO/STO INTERFACE

In this chapter we will present a recently created oxide 2DEG which combines the properties of the LAO/STO 2DEG, described in Chapter 1, with a further degree of freedom: magnetic coupling. This is achieved by inserting a delta doping layer of $EuTiO_3$ between LAO and STO. This magnetic 2DEG has been studied using a wide range of techniques, from electrical transport down to milliKelvin temperatures, to angle-resolved photoemission spectroscopy. The experimental results are supported by Density functional theory calculations. [1]

[1] Some of the results shown in this chapters are included in a manuscript currently under review[70]

2.1 Realization of the LAO/ETO/STO 2DEG

In the previous chapter the LAO/STO 2DEG was introduced, together with its main properties and some outlooks for electronic applications. In paragraph 1.4, in particular, we discussed the importance of SOC in this system for spintronics and spin-orbitronic applications, as shown for instance in Fig. 1.7. Some recent works on the spin to charge conversion (Fig. 1.9) lead to very encouraging results. In these experiments, the addition of a magnetic layer was used to inject a spin-polarized current, which was then converted into a charge current. In the present chapter we will introduce a oxide 2DEG where the magnetic coupling is included in the system by the insertion of another oxide layer: $EuTiO_3$ (ETO).

ETO is rare earth titanate with perovskite structure. It has a cubic structure down to low temperatures with lattice parameters (a=b=c= 3.905Å) perfectly matching those of STO. Its electronic structure is also very similar to that of STO, with a broad band about 3.0 eV below the Fermi level originating from O-2p states and a conduction band formed by Ti-3d states. However, ETO possesses also a narrow Eu-4f band, below the Fermi level, located within a direct band gap of ~ 0.93 eV , much smaller than those of STO (~ 3.2 eV) and LAO (~ 5.6 eV). Bulk ETO has a G-type antiferromagnetic (AFM) ground state below the Néel temperature T_N ~ 5.5 K, which is switched to a ferromagnetic (FM) state by doping or lattice strain [73–77]. The lattice, electronic, and magnetic properties of ETO, as well as the

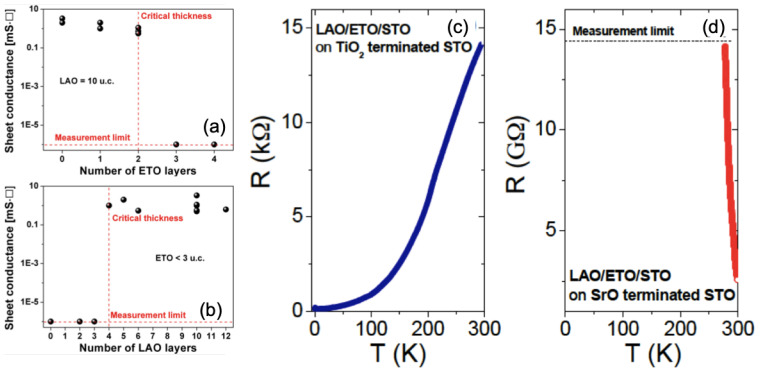

Figure 2.1: Sheet conductance of LAO/ETO/STO samples measured at room temperature (a) as a function of the number of ETO layers (LAO thickness = 4 u.c.) and (b) as a function of the number of LAO layers (ETO thickness = 3 u.c.). Resistance vs Temperature of LAO(10u.c)/ETO(2u.c. on a TiO_2 (c) and SrO (d) terminated STO substrate [71].

nonpolar character of the (001) surface, similar to STO, make it a perfect candidate as a magnetic dopant layer for LAO/STO interfaces [71].

When a thin layer of ETO is introduced between LAO and STO, a conducting interface is formed. The number of ETO layers is a crucial parameter because the conductance is present only for ETO films of 1 or 2 u.c., whereas for higher thicknesses (up to 6 u.c.) the conductance is negligible (Fig. 2.1 (a)). On the other hand by fixing the ETO thickness to 1 or 2 u.c., the conductance is finite only for LAO thicknesses equal to or larger than the critical value of 4 u.c. (Fig. 2.1 (b)), as in the case of the usual LAO/STO conductive interfaces. Furthermore, the conducting interface is present only when the STO substrate used is TiO_2 terminated (Fig. 2.1 (c) and (d)). All these elements indicate that the mechanism responsible for the formation of a 2DEG in LAO/ETO/STO is the polar catastrophe, similarly to what described for LAO/STO in the previous chapter [71].

When cooled down at milliKelvin temperatures, LAO/ETO/STO shows a superconducting transition Fig. 2.2 a)) [72]. Similarly to what happens in LAO/STO, the critical temperature T_c is modulated by the gate voltage with a maximum of 125 mK for a carrier concentration of n_{2D}=2.5 x 10^{13} cm^{-2}. This behavior is presented in Fig. 2.2 b) in the form of a "phase diagram". In the same picture, Kondo and Ferromagnetic areas are indicated. These effects will be discussed in the next

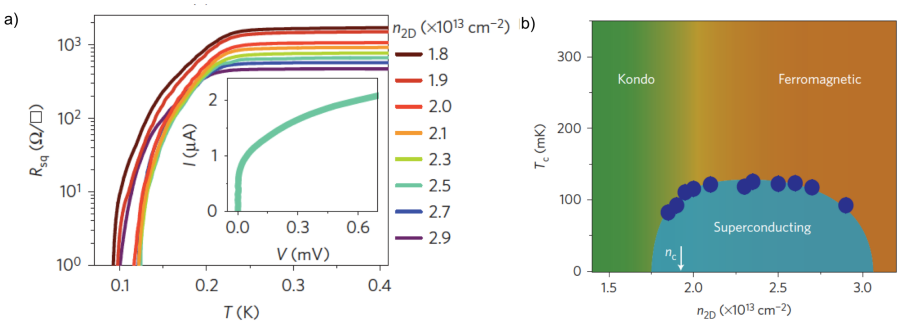

Figure 2.2: a) Sheet resistance R_{sheet} versus T for several carrier densities tuned by gate voltage (from -40V to +30 V). The inset shows a current versus voltage curve measured at 50 mK where a critical current is clearly visible. b) Phase diagram of the LAO/ETO/STO heterostructure. Blue closed circles are the zero resistance critical temperature. The areas in different colors indicates the different electronic states [72].

paragraphs.

2.2 Density functional theory calculations

The nature and properties of LAO/ETO/STO interface has been investigated via Density Functional Theory with on-site Hubbard terms (DFT+U) calculations [70]. In this paragraph we will present the main results of such investigation, which will be then compared with experimental results in the next paragraphs.
DFT+U calculations were performed on an ideal c (2x2) LAO/ETO/STO(001) heterostructure composed by 5u.c. of LAO, 2u.c. of ETO and 4u.c. of STO stacked along the c-axis, and a vacuum region of 20 Å (Fig. 2.3 (a)). Models with the Eu-ions in both AFM (G-type) and FM configurations were tested. It was found that FM solution is the lowest in energy for the system (about -20 meV per simulation cell). Figure 2.3 (b-d) summarize the main finding of the simulations. Firstly, the layer, atomic and spin resolved, local density of states (LDOS) across the interface in

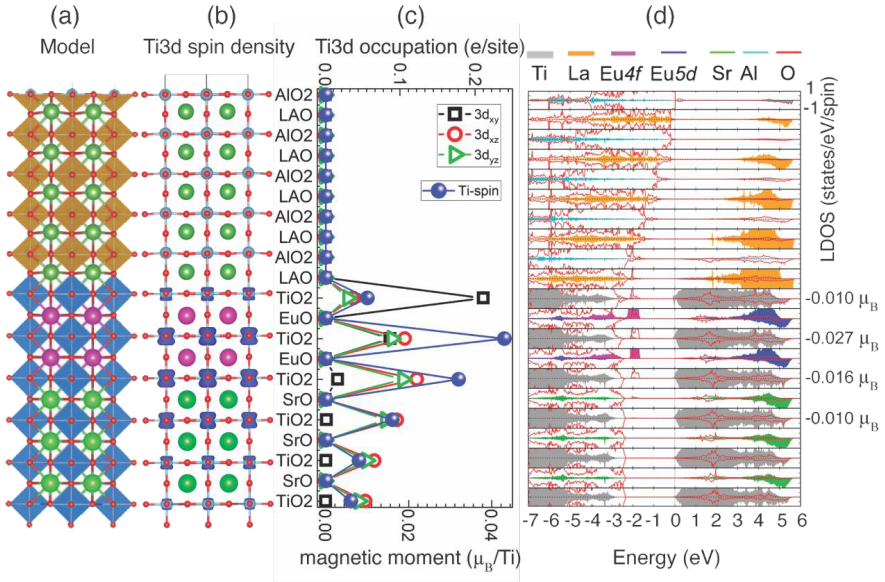

Figure 2.3: (a) Structural model of a c(2x2) LAO/ETO/STO(001) heterostructure; (b) integrated Ti-3d spin density plot across the interface; (c) orbital and layer resolved Ti-3d occupation (black squares, $3d_{xy}$, red circles $3d_{xz}$, green triangles $3d_{yz}$) and Ti-3d magnetic moment (blue circles) obtained by integrating the density of states between -0.3 eV and the Fermi energy. d) Layer-, spin- and element- resolved density of states. The color code for the partial LDOS contribution of different ions is indicated on top of the figure. On the right side of the figure, the values of the calculated oxygen-2p magnetic moment in the corresponding interfacial TiO_2 layers is indicated.

Fig. 2.3 (d)) shows an overlap between the energy positions of the O-2p band of the AlO_2 surface and of the interfacial TiO_2 3d conduction bands. This confirms that the 2DEG at the LAO/ETO/STO interface is formed through the transfer of electrons from the surface layers of LAO to the Ti-states in the ETO and STO layers, in order to eliminate the polar discontinuity at the LAO/ETO interface, analogously to what happens in LAO/STO. Fig. 2.3 (c) shows that the occupancy of the charge carrying Ti-3d states is very high within the ETO layer (black, red and green data) and expands for a few unit cells into STO. Another important information included in Fig. 2.3 (c) is that the Ti bands are spin-polarized (blue data, bottom scale), with the highest polarization within the ETO layers, which, as mentioned above, exhibit also the largest electron occupation. However, the Ti-3d magnetic moment expands also into the first three-unit cells of STO. Consequently, both ETO and topmost STO unit cells host electrons which are spin-polarized. The layer resolved map in Fig. 2.3 (d) shows also a finite spin-polarized electron density of Ti-3d, Eu-5d and O-2p states at the position of the Eu2+ peak, demonstrating a hybridization between Eu-4f, Eu-5d, O-2p and Ti-3d states.

The bands contributing to the LAO/ETO/STO 2DEG are reported in the spin resolved band structure of in Fig. 2.4 in the FM ground state (left panel) and, for comparison, in the AFM one (right panel). In both cases, the lowest lying Ti-3d band crossing the Fermi energy is a dispersive parabolic band with d_{xy} orbital

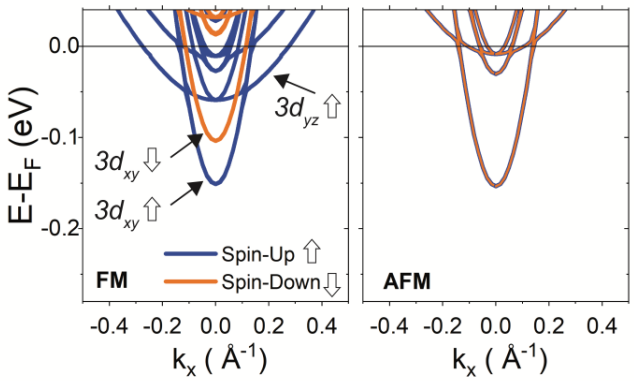

Figure 2.4: Spin-resolved band structure calculations of the Ti-3d bands around the Γ-point in a small energy range in the FM (left panel) and AFM (right panel) solutions. Note that in the FM solution, the spin-up $3d_{yz}$ band shifts to lower energy and crosses the Fermi level, while the $3d_{xy}$ spin down bands shifts-up, giving rise to an overall spin-polarization of the 2DEG.

character, which switches at larger momentum into a much flatter band indicating an avoided crossing with the heavy bands with d_{xz}, d_{yz} orbital character. This result is similar to that discussed for LAO/STO in Chapter 1 (Figure 1.3 d)). In the FM solution of the model, spin-up (blue) and spin-down (orange) bands, of both the d_{xy} and $d_{xz,yz}$ bands, are split in the whole energy range and cross the Fermi level, showing a majority of spin-polarized electrons in the system. The conduction band minimum, associated with the lowest $3d_{xy}$ band is the same in both AFM and FM phases. However, calculations show a down-shift of the spin-up $3d_{xz,yz}$ bands and more importantly a filling of these bands taking place only in the FM ground state. Thus, a FM ground state appears simultaneously with the filling of $3d_{xz,yz}$ bands at the Fermi level. This finding is extremely important for the comparison with electrical transport experiments that will be shown in the next sections.

In Summary, DFT calculations show that:

- the solution with the Eu-ions in FM configuration is the lowest in energy for the system;
- the formation of the 2DEG at the LAO/ETO/STO interface is due to the same polar catastrophe mechanism found in LAO/STO;
- spin polarized carriers, present in the ETO layer, extend in the first unit cells of STO;
- Ti $3d_{xy}$ and $d_{xz,yz}$ bands are spin-split in the whole energy range and cross the Fermi level, showing a prevalence of spin-polarized electrons in the system;
- Ferromagnetism appears simultaneously with the orbital selective filling of $3d_{xz,yz}$ bands at the Fermi level.

A fundamental point, however, is left to understand: given the non-magnetic nature of Ti-3d states, the spin-polarization observed in the results of Fig. 2.3 can only be due to a form of coupling between the magnetic Eu-4f and Ti-3d states. This is rather surprising considering that 4f orbitals are characterized by strong electron localization. In order to solve this issue, we show the spin-resolved LDOS of the ETO layers in the FM ground state in Fig. 2.5(a), obtained

by DFT+U calculations [70]. For comparison, in the same figure, also the AFM configuration is reported (panel 2.5(b)). From the calculations it can be noted that Eu-5d states, while having a much weaker spectral weight than the O-2p and Ti-3d contributions, have a strong overlap with Ti-3dt_{2g} bands in the FM ground state close and above the Fermi level. Furthermore, there is also a substantial overlap with the Eu-4f state around -2 eV, where these states also show a clear spin-polarization. All these features of the Eu-5d states are absent in the AFM solution (panel b). These results suggest that the FM-ordering of Eu_2 is mostly due to a FM interaction mediated by Eu-5d/Ti-3d hybridized states.
All the results briefly shown in this section will be now compared with spectroscopic and electrical transport measurements.

2.3 Evidences of ferromagnetic coupling in XMCD measurements

The magnetism of LAO/ETO/STO was studied by x-ray magnetic circular dichroism (XMCD) at the Swiss Light Source of the Paul Scherrer Institute. By using the sum-rules, this technique allows an estimation of the Ti and Eu magnetic moments from the analysis of the XMCD spectra acquired at the Ti-$L_{2,3}$ (2p → 3d transition)

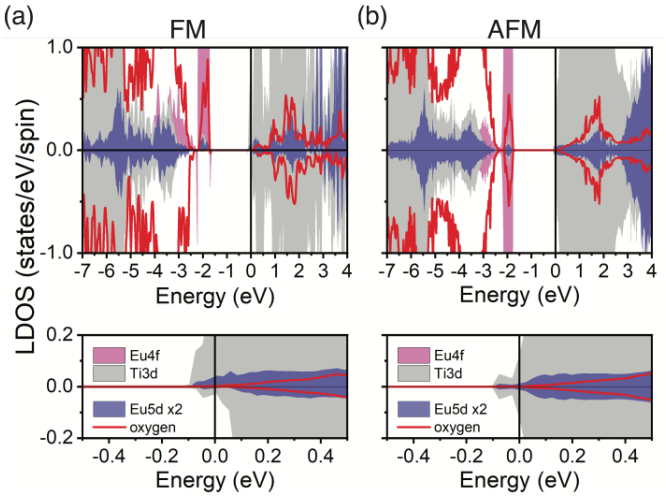

Figure 2.5: Spin-resolved density of states for ETO layers with (a) FM and (b) AFM coupling. In the FM solution we do observe a substantial spin-polarization at -2 eV of both Eu-4f (magenta) and Eu-5d (blue) states, and an overlap between Ti-3d states (grey) and Eu-5d states near and above the Fermi level.

and Eu-$M_{4,5}$ edges (3d→4f transition) [71, 72, 78]. Fig. 2.6 a) and b) report the Eu spin moment (m_{spin}) and the Ti orbital moment (m_{orb}) measured in grazing incidence conditions (almost parallel to the interface) as a function of the magnetic field and of the temperature. It is found that the Eu^{2+} spins order ferromagnetically below 6-8K with a saturation field of ~2T (green data in both panels). Interestingly, the Ti orbital moment shows similar field and temperature dependence (blue data), indicating that the two signals are linked, in agreement with the conclusions of DFT calculations (Fig. 2.5). In order to understand the origin of the Ti magnetic

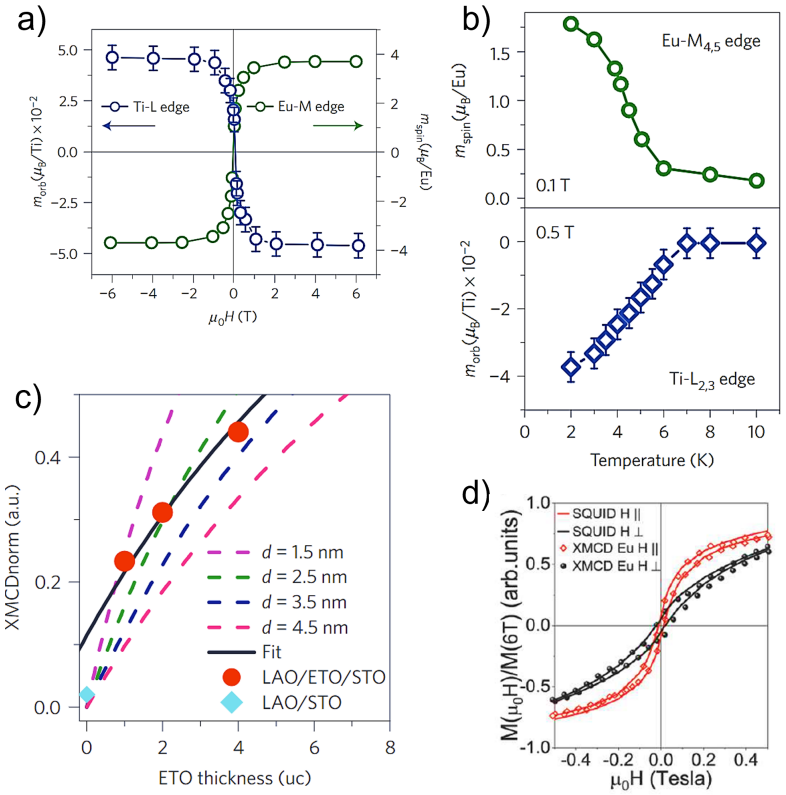

Figure 2.6: Averaged (a) magnetic field and (b) temperature dependence of the Eu spin moment (m_{spin}, green symbols) and of the Ti orbital moment (m_{orb}, blue symbols); c)XMCD amplitude of LAO/ETO/STO samples normalized to the X-ray absorption spectroscopy (XAS) intensity measured at 2 K as function of the ETO thickness (red circles). Short dashed lines are calculated profiles in the case of an XMCD coming only from ETO with different values of the probing depth. The continuous black line is a guide to the eye. In cyan we show the XMCD of a reference LAO/STO sample measured in the same conditions. d) Eu-XMCD (scatter data) and SQUID magnetization (continuous lines) as function of the magnetic field parallel (red) and perpendicular (black) to the interface. The data are normalized to the saturation value.

signal, Fig. 2.6 c) shows the amplitude of the Ti XMCD signal obtained for several LAO/ETO/STO samples with varying ETO thickness, from 1 to 4 u.c. In the case

of magnetism due to the ETO film alone, this signal should increase sharply for each ETO unit cell added. In contrast, its experimental gradual increase, with a finite extrapolated value (indicated by the black line) clearly indicates a magnetic contribution coming also from the STO interfacial layers. Also this result is in agreement with DFT calculations, in particular with the Ti magnetic moment calculations of Fig. 2.3 (c). Finally, in panel (d) the XMCD results are compared with macroscopic magnetization measurements obtained using a SQUID magnetometer [70, 71]. The two sets of data, normalized to the saturation value for direct comparison, are in good agreement. They both show a clear, although small, hysteresis around zero magnetic field and a preferential orientation of the magnetization parallel to the interface.

2.4 Evidences of ferromagnetic coupling in the Resistance vs temperature curves

The presence of long-range ferromagnetic coupling in LAO/ETO/STO has been established via electrical transport measurements as a function of temperature, magnetic field and carrier concentration modulated via electric field effect. Fig. 2.7 shows the behavior of the sheet Resistance R_{sheet} of two LAO/ETO/STO samples as a function of the temperature for several values of the gate voltage. The red arrows in the figure indicate a change in the R_{sheet} slope appearing at high gate voltage (accumulation mode) around 7K, a temperature which corresponds to the onset of FM correlations determined by XMCD measurements (Fig. 2.6 b)). Therefore, this reduction in the resistance can be attributed to reduced scattering in the ferromagnetically ordered state. On the other hand, at low gate voltage (depletion mode) the curves show a steep upturn. In Ref. [72] this behavior was found to be related to Kondo scattering with magnetic centers having spin 1/2, associated with $3d^1$ magnetic moments, and a Kondo temperature between 15 K and 20 K.
More detailed indications of FM coupling in LAO/ETO/STO can be derived from measurements in magnetic field.
Before analyzing the magnetotransport of LAO/ETO/STO 2DEG we briefly introduce and important effect appearing in ferromagnetic metals: the Anomalous Hall

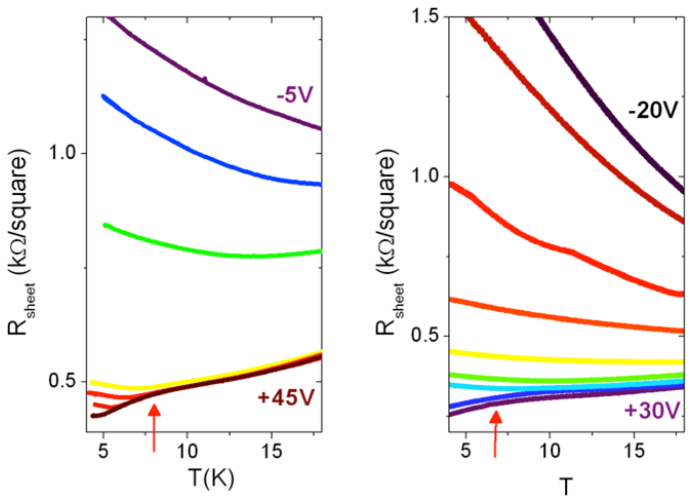

Figure 2.7: a) Temperature dependence of the sheet resistance, R_{sheet} as a function of the gate voltage for two LAO/ETO/STO samples. The red arrows indicate the position of the downturn related to reduced scattering below the FM transition.

effect.

2.5 The Anomalous Hall Effect

In general, the Hall effect describes what happens when an electrical current flows in a conductor immersed in a perpendicular magnetic field B_z. In these conditions, the motion of the charge carriers is affected by the Lorentz force proportional to magnetic field, which deviates the electrons from a straight direction and leads to their accumulation on one face of the material. This leaves equal and opposite charges exposed on the other face. An asymmetric distribution of charge density across the Hall element results.

In ferromagnetic materials, in addition to the ordinary Hall effect, there is another contribution to the Hall voltage, called Anomalous Hall Effect (AHE) that is proportional to the magnetization of material [79]. An experimental relation describing the transverse resistivity of ferromagnetic materials has been found by Pugh and Lippert [80, 81]:

$$\rho_{xy} = R_0 H_z + R_{AHE} M_z$$

where M_z is the magnetization, the ordinary Hall effect R_0 depends on the electron concentration and mobility and R_{AHE} is the anomalous component.

Three main mechanisms have been proposed for AHE: skew scattering [82, 83], side jump [84] and an 'intrinsic contribution' or 'anomalous velocity' contribution [85] (Fig. 2.8). The latter term is related to the Berry curvature: in an electric field the electrons acquire an additional amount of group velocity (the anomalous velocity). The anomalous velocity is perpendicular to the applied electric field. In general, in non-magnetic materials the sum of the anomalous velocities over all occupied band states is zero, but in systems with broken time-reversal symmetry and broken inversion symmetry, it is present [86, 87]. This feature for clean metals depends only on the band structure and is independent of scattering.
A different mechanism is proposed by Smit involving impurities in bad metals. Smit claimed that the main source of the AHE currents in this case is asymmetric 'skew' scattering from impurities caused by their spin-orbit coupling. The asymmetry can be defined through the (positive or negative) energy contribution of the spin-orbit Hamiltonian that depends on the relative orientation of the repulsive impurity potential, the electron moment and spin orientation.
Lastly, the side-jump mechanism, already proposed by Smit [82, 83] and then largely explored by Berger [84], suggests that a particle travelling in a solid in the presence of spin-orbit coupling experiences opposite electric fields when scattered by a (non magnetic) impurity. The electric fields will produce an electron velocity deflection in opposite directions. Time integration of the velocity deflection represents the side jump distance.
Recently, linear transport theories have been developed, like the semiclassical Boltzmann transport theory [89, 90] and the microscopic theories based on the

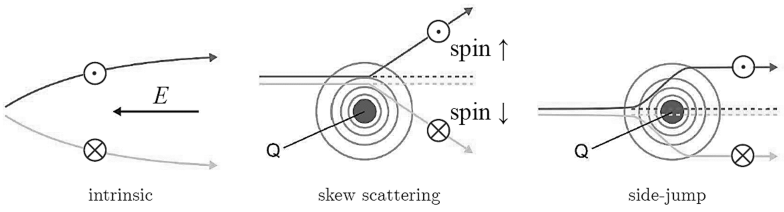

Figure 2.8: Scheme of the intrinsic and extrinsic (skew scattering and side-jump) mechanisms at the basis of the Anomalous Hall effect. Adapted from [79].

Kubo formalism and the Keldysh formalism [90, 91] [92]. These produce similar predictions [79, 82, 83]. In such theories, the classification of contributions to the AHE is based on the dependence of the conductance on the Bloch-state transport lifetime τ. The main advantages of defining the contributions through τ is the possibility to use a scaling law for the AHE analysis. Numerical calculations of Anomalous Hall conductivity σ_{xy}^{AHE} identified three distinct regimes as a function of the longitudinal conductivity σ_{xx}:

- an high conductivity regime, where $\sigma_{xy}^{AHE} \propto \sigma_{xx}$ and the observed AHE is attributed to scattering from magnetic impurities (skew scattering);
- an intermediate or intrinsic conductivity regime, where $\sigma_{xy}^{AHE} \sim cost$ and as a consequence the AHE is independent from σ_{xx} and related only to the Berry curvature of the involved bands (intrinsic AHE);
- an incoherent regime where $\sigma_{xy}^{AHE} \sim \sigma_{xx}^{1.6-1.8}$, also referred to as a bad metal regime [79].

All three regimes have been observed in several experiments, as summarized in Fig. 2.9.

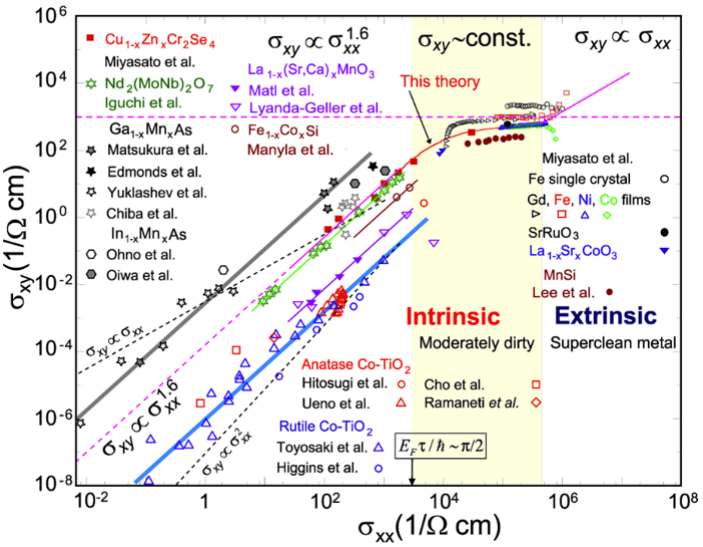

Figure 2.9: Review of main experimental results on various ferromangets, including transition-metals, perovskite oxides, spinels, and magnetic semiconductors. Adapted from [88].

2.6 The Anomalous Hall Effect at the LAO/ETO/STO interface

Figure 2.10 a) shows the transverse resistance R_{xy} of two samples of LAO/ETO/STO as a function of magnetic field for several values of the gate voltage. For a voltage tuned carrier concentration n_{2D} larger than $n_c \sim 1.9x10^{13} cm^{-2}$ (i.e. for V_g>-10V in panel a) and V_g>-20V in panel d)), the curves present a high field (> 6T) nonlinearity typical of multi-band transport, and in particular to the filling, besides the $3d_{xy}$ band, of $3d_{xz,yz}$ bands. A similar nonlinear Hall effect has been observed in LAO/STO, and interpreted as evidence of a Lifshitz transition [13]. At the same time, however, a low-field curvature is also present (see panel b)). This has a close resemblance to that reported for ferromagnetic ETO films [93] and attributed to Anomalous Hall Effect. The AHE component can be estimated by subtracting from the R_{xy} curves, the linear component above 4T (i.e. above the saturation of the magnetization found for LAO/ETO/STO). The result of such calculation is presented in panel (e) of Fig. 2.10 (see also Ref. [70, 72]). The anomalous component R_{AHE} depends on the gate voltage-tuned carrier concentration n_{2D}: for $n_{2D} < n_c$ it is zero, while for $n_{2D} > n_c$ it increases monotonically. We point out that n_c was found to be the carrier concentration at which $3d_{xz,yz}$ bands enter the transport of

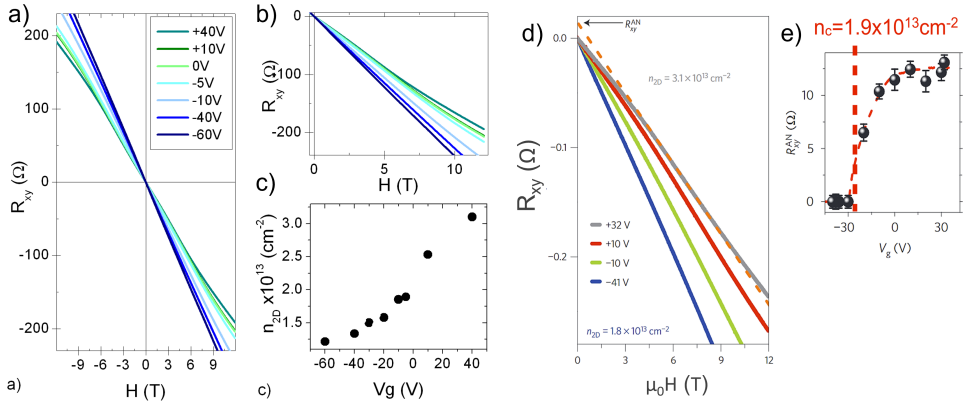

Figure 2.10: (a) and (d) Transverse resistance R_{xy} of two LAO/ETO/STO samples (A and B respectively) as a function of the magnetic field and for several values of the gate voltage V_g. b) Zoom of the positive field region for sample A. Panel c) shows the correspondence between the gate voltage values and the the carrier concentration calculated from the Hall coefficient of the same curves for sample A. e) Anomalous Hall component as a function of the carrier concentration for sample B. Panels d) and e) are adapted from Ref. [72]).

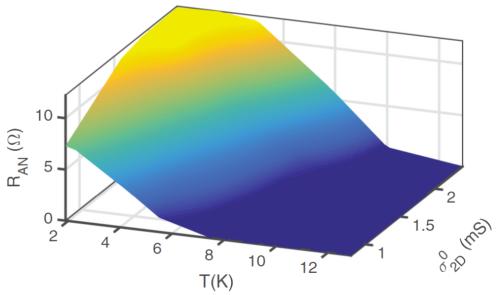

Figure 2.11: 3D plot of the temperature and sheet conductance dependence of the anomalous Hall component R_{AN} in LAO/ETO/STO

the system, activating the coupling with magnetic Eu states, as demonstrated by the DFT calculations shown in paragraph 2.2.

The temperature dependence of R_{AHE} is also in agreement with XMCD data shown in Fig. 2.6 b), as reported in Fig. 2.11 [94]. Finally, the correlation between the AHE and the magnetization of the film is clearly demonstrated by comparing the normalized transverse resistance curves with the field behavior of the Eu spin moment measured via XMCD (Fig. 2.12). The two signals, although obtained with radically different techniques, are in excellent agreement.

All these results demonstrate that the low field curvature of the R_{xy} data shown in fig. 2.10 is linked to ferromagnetism induced AHE in LAO/ETO/STO.

In the previous paragraph 2.5 the different mechanisms from which AHE originates have been presented. They can phenomenologically distinguished by analyzing the relation between σ_{xy}^{AHE} and σ_{xx}.

In the case of a 2DEG, these two terms can be written as:

$$\sigma_{AHE}^{2D} = \frac{\rho_{AHE}}{(\rho_{AHE})^2 + (\rho_{xx}^{2D}(0))^2} \tag{2.1}$$

$$\sigma_{xx}^{2D} = \frac{\rho_{xx}^{2D}}{(\rho_{AHE})^2 + (\rho_{xx}^{2D}(0))^2} \tag{2.2}$$

where $\rho_{xx}^{2D}(0)$ is the zero field 2D resistivity, and ρ_{AHE} is the saturation value of the anomalous Hall 2D resistivity, as calculated from the anomalous component of the Hall effect (Fig. 2.10).

Data collected on two LAO/ETO/STO representative samples, with carrier densities tuned by a back-gate voltage, are shown in Fig. 2.13. A correlation $\sigma_{AHE} \propto (\sigma_{xx})^{\alpha}$

with $\alpha = 1.8$ is clearly found. This result excludes a skew scattering mechanism and a purely intrinsic AHE. We conclude that in LAO/ETO/STO an intrinsic AHE suppressed by disorder is at play, analogously to what found in La-doped ETO films [93].

.

2.7 Spin-Orbit Coupling and Ferromagnetism

In Chapter 1 we have highlighted how the Rashba spin-orbit coupling (SOC) in low-dimensional systems is a fascinating way to control spin transport in the view of developing novel spintronic devices. Moreover, in the previous paragraphs, the ferromagnetic (FM) properties of LAO/ETO/STO were described. In the present paragraph we will study the interplay between these two phenomena, SOC and FM, in LAO/STO/STO by the analysis of the magnetoconductance curves.
The magnetoconductance of two-dimensional electron systems and thin disordered films shows deviations from classical theory, caused by “weak localization" (WL). Weak localization is a quantum correction to the conductance observed at low temperatures related to the interference of electron waves diffusing around impurities [95]. This effect enhances the probability of back-scattering for electron paths,

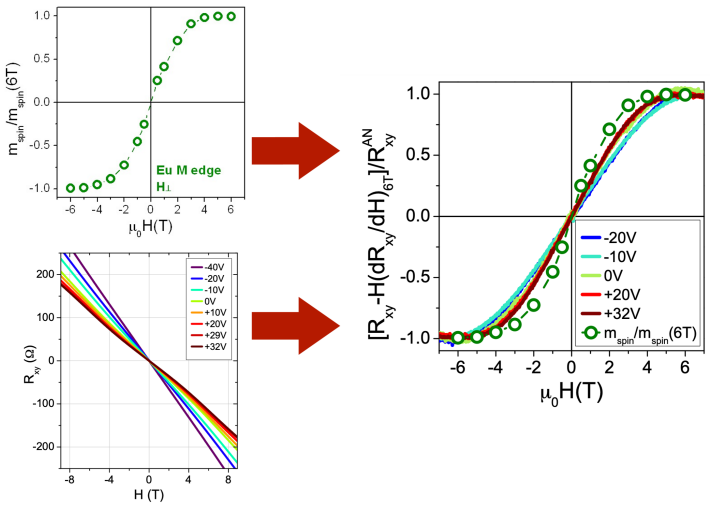

Figure 2.12: Comparison between the normalized R_{xy} and Eu spin moment measured via XMCD [72].

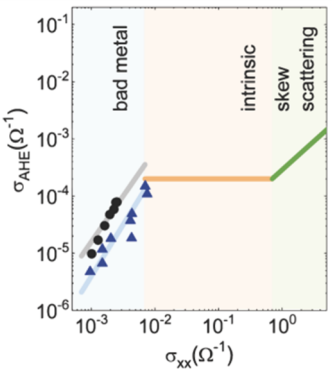

Figure 2.13: Anomalous Hall conductivity vs longitudinal 2D conductivity. Black dots and blue triangles refer to two different LAO/ETO/STO samples. Full lines refer to the exponent α in the relation $\sigma_{AHE} \propto (\sigma_{xx})^{\alpha}$: α = 1.8 (light blue, and gray, intrinsic AHE suppressed by disorder), α = 0 (orange, intrinsic AHE), α = 1 (green, skew scattering).

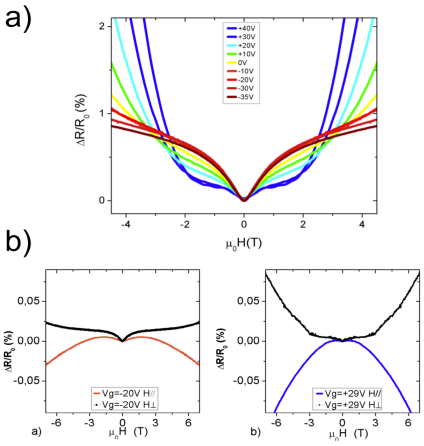

Figure 2.14: a) Differential magnetoresistance (R(H) - R(H = 0))/R(H = 0) (%) in perpendicular magnetic field for different applied gate voltages. b) Magnetoresistance curves measured at V_g = -20V (left panel) and V_g = +30V (right panel) applying the magnetic field both perpendicular and parallel to the 2DES plane. Adapted from [94].

decreasing the conductance of the film. In the presence of sufficiently strong SOC, the spin of the electrons states contributes to the amplitude of the interference reducing it with respect to the case without spin interactions. This reduction leads to the "weak antilocalization" (WAL) effect and the back-scattering is reduced below the statistical one. This corresponds to an echo in the forward direction and an increase of the conductance.

Applying an external magnetic field reduces the carriers' phase coherence length

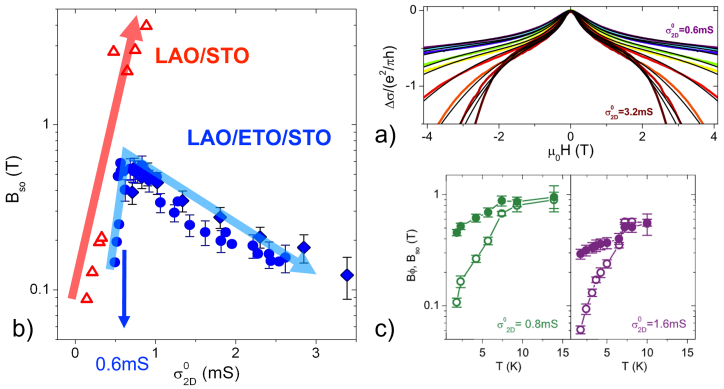

Figure 2.15: a)Differential magnetoconductance data $\Delta\sigma_{2D} = \sigma_{2D}(H) - \sigma^0_{2D}(H)$ plot in units of $\sigma_0 = e^2/\pi h$measured at T = 1.9 K on LAO/ETO/STO. The full black lines are the fit using ILP theory. (b) Spin-orbit field B_{so} and inelastic field B_ϕ obtained from the fit. c) Temperature dependence of B_{so} (filled symbols) and B_ϕ (open symbols) for two conductance values. Adapted from Ref. [94].

and washes out quantum interference, suppressing both WL and WAL. Therefore these quantum effects manifest in a negative magnetoconductance (or positive magnetoresistance), in the case of WAL due to Rashba SOC, and positive magnetoconductance (negative magnetoresistance) for WL .

The differential magnetoresistance (MR) curves acquired applying the external magnetic field perpendicular to the LAO/ETO/STO interface at T = 1.9K, and for several values of the gate voltage, are shown in Fig. 2.14 a). The curves show a dip around zero field. This dip persists also in parallel magnetic field, as shown in panel 2.14 b), therefore it can not be attributed to the anisotropic magnetoresistance effect appearing in ferromagnetic metals, but rather it can be considered as a signature of WAL [94], similarly to the case of LAO/STO [17].

In order to obtain information on the SOC parameters, the curves can be fit with localization model of Iordanskii, Lyanda-Geller and Pikus (ILP) [96], allowing to extract the spin-orbit field B_{so} and inelastic field B_ϕ.

In figure Fig. 2.15 a) we show the same data of Fig. 2.14 a) plot in terms of magnetoconductance. The black lines are the fit obtained with the ILP formalism. In panel Fig. 2.15 b) the B_{so} values obtained from the fit are plotted as a function of the field-effect modulated sheet conductance σ^0_{2D}, which is directly related to the carrier concentration of 2DEG. In the same plot the data of LAO/STO interface have been added for comparison. At low conductance (corresponding to low carrier

concentration), the SOC field of LAO/ETO/STO follows that of the LAO/STO 2DEG, demonstrating the same increasing behavior with the carrier concentration. However, at a σ^0_{2D} = 0.6mS, corresponding to $n_c \sim 1.9x10^{13} cm^{-2}$, B_{so} starts to decrease. The most interesting aspect is that the change in slope of B_{so} versus σ^0_{2D} takes place at the same value found for the onset of ferromagnetic effects [72], as shown in paragraph 2.5. Therefore, this non monotonous trend of the SOC field is related to the emergence of FM, which reduces the WAL corrections to the magnetoconductance and attests the interaction between spin orbit and ferromagnetism.
The temperature behavior of the B_{so} and B_{ϕ} fields are reported in fig. 2.15 c). The parameter B_{so} displays a further interesting response: instead of being independent from the temperature [97] as expected, it increases with increasing temperature. These results are related to the reduction of the magnetization of 2DEG in LAO/ETO/STO. At low carrier concentration (low V_g), where ferromagnetism disappears around 6 K, the increase of B_{so} is sharper, compared to what happens in high carrier concentration, where ferromagnetism persists until 10 K (see also Fig. 2.11 c)).
To conclude, ferromagnetism masks (without destroying completely) the WAL corrections to the magnetoconductances of LAO/ETO/STO heterostructures. These WAL corrections become significant when the temperature is low and the carrier density is high, where the ferromagnetic correlations reache the maximum values.

2.8 Conclusions

To conclude the overview of LAO/ETO/STO properties, we summarize the main characteristics of this system:

- By inserting a thin layer of ETO between LAO and STO, a 2DEG can be realized with general transport properties similar to those of LAO/STO (carrier concentration, tunable superconductivity, presence of SOC)
- DFT calculations show that the formation of the 2DEG is due to the polar catastrophe mechanisms and that a coupling between the magnetic Eu-4f states and Ti-3d states is present, suggesting the activation of FM in the 2DEG

- XMCD e SQUID magnetometry measurements indeed reveal a magnetic signal deriving from the Ti states
- transport measurements confirm the activaiton of long-range FM coupling. This appears simultaneously with the filling of $3d_{xz,yz}$ orbitals, as predicted by DFT calculations, confirming their crucial role in establishing FM correlations in the 2DEG. Moreover, the analysis of AHE allow to confirm its intrinsic nature
- the interplay between FM and SOC can be revealed analyzing the magnetoconductance curves as a function of carrier concentration and temperature

Finally, we briefly discuss the coexistence of ferromagnetism and superconductivity. In Fig. 2.2 b) the phase diagram of LAO/ETO/STO was anticipated. Now it is possible to see that in large part of the phase diagram, superconductivity arises from a FM state. This co-existence of normally mutually exclusive phenomena supports the hypothesis of an unconventional superconductivity, similarly to what reported in Ref. [26]. While some works explain this coexistence of superconductivity and ferromagnetism as due to a phase separation of two regions [38], others define microscopic theory according to which the two phases come from different orbital states involved [98]. In order to settle this fascinating topic, more experiments will be needed. In particular, analysis of nanoscale devices, as for instance Josephson junctions, would be extremely interesting. In the next Chapter we will present the a novel nanofabrication technique set up for the realization of such devices with LAO/ETO/STO 2DEG.

CHAPTER 3

REALIZATION AND PROPERTIES OF LAO/ETO/STO BASED NANODEVICES

The discovery of a high-mobility 2DEG at the interface between oxide insulators has undoubtedly expanded the possibility for oxide application in electronics. Indeed, in the latest years, the activities aimed at realizing oxide based nanodevices multiplied. These devices could give the unique opportunity of investigating the physics of a 2D system in detail and studying the interaction among several, in some cases antagonistic, electronic phases. In this Chapter we will present an overview of the main fabrication techniques developed for oxide 2DEG and introduce a novel one created for the LAO/ETO/STO 2DEG. [1]

[1] Parts of this chapter have been published in M. D'Antuono et al., *Nanopatterning of oxide 2-dimensional electron systems using low-temperature ion milling*, Nanotechnology, 33 085301 (2021)

3.1 Introduction to electric field effect devices based on STO

In the previous chapter, we showed the possibility to tune the STO-based interface properties (such as carrier density, superconductivity, spin-orbit coupling) with electric field effect [99]. In general, a semiconducting field-effect transistors (FETs) is composed by source and drain electrodes, a conducting channel between them and a gate terminal. The channel and gate electrode are separated by an insulating dielectric, forming a parallel plate capacitor.
For the 2D STO-based oxides systems, we may distinguish three main geometrical field effect configurations as sketched in Fig 3.1: back-gate [6] (panel (a)), side-gate [100] (panel (b)), and top-gate [101] (panels (c) and (d)). Among the possible options,

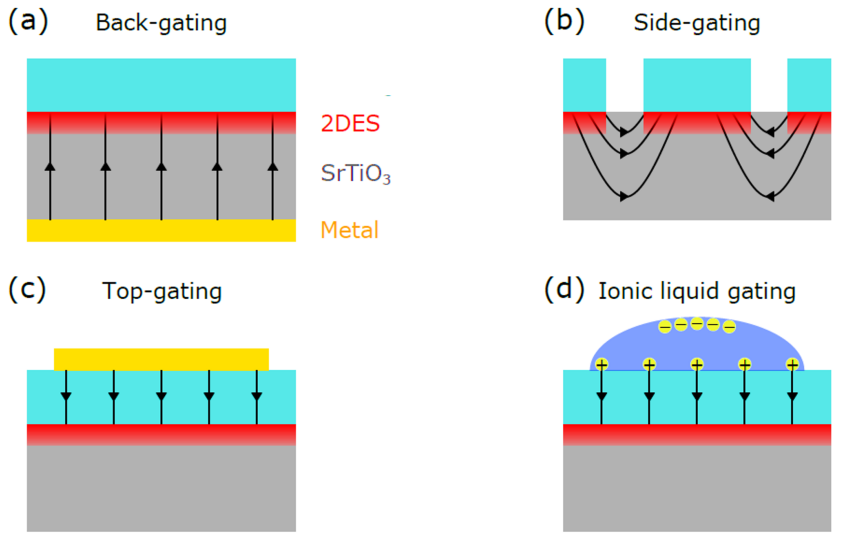

Figure 3.1: Possible geometrical configurations for $SrTiO_3$-based field-effect devices. (a) Back-gate configuration; (b) Side-gate configuration; (c) Top-gate configuration. (d) Ionic liquid gate configuration. The black lines represent electric field lines induced by the external gate voltage.

the back-gate geometry is the most widely used. Here, the STO substrate serves as a gate dielectric. The field lines cross the STO to close in the 2DEG, similarly to a plate capacitor.
This geometry has the advantage of a straightforward realization and of the possibility to exploit the large dielectric constant at low temperature of STO [102]. However, it presents also some important disadvantages. Firstly, it is a "global"

technique: the carrier density of all the devices present on the chip is modulated when a gate voltage is applied to the back electrode. Moreover, the thickness of commercially available STO-substrates is of 0.5 mm. This translates into a very thick dielectric layer which, in turn, limits greatly the voltage efficiency of the devices.
In the side-gate geometry (Fig. 3.1 (b)), the field effect allowS to perform a local modulation of the carrier concentration at the interface with optimal efficiency [100, 103]. As it can be seen in the sketch, the electric field lines (drawn in black) depart from the side electrodes and penetrate into the high dielectric constant STO, before bending and closing in correspondence with the 2DEG. In this sense the side-gate devices behave as standard back-gate configuration, but with increased efficiency thanks to a smaller thickness of the gate dielectric involved. Using this technique, a superconductor to insulator transition by applying only 0.2 V was obtained in LAO/STO nanodevices [53].
The method of the top-gate geometry works in a similar way as the back-gate counterpart, but using the LAO layer as insulating dielectric. Compared to back-gate configuration, it requires lower voltages to achieve a huge gating effects [104–106]. However, the device fabrication process in the top gate configuration is made more complex by an additional lithography step needed to define the top electrode and by the risk of leakage in the gate current due to top film imperfections and impurities. Another example of top-gate configuration is the ionic liquid gating (Fig. 3.1 (d)). In this case the channel is covered by a drop of ionic liquid which exerts a substantial electric field on the STO-based heterointerface below [107].
All the devices layout described above require some level of patterning to define the conduction channel, the gate electrodes etc. In the next section we will briefly describe the most used patterning techniques for oxide-based 2DEG, before introducing that developed during this work for the patterning of LAO/ETO/STO heterostructures.

3.2 Nanopatterning techniques for oxide 2DEGs

The patterning of STO-based heterointerfaces represents a challenge because the formation and the stability of the interface conductivity are extremely sensitive

to sample processing conditions. Conventional patterning techniques moreover cannot be applied due to the necessity of preserving the insulating topmost layer (which creates the conducting interface). For these reasons, during the latest years, several techniques were developed specifically for the LAO/STO 2DEG system (Fig. 3.2).

Amorphous technique

This approach, the first one to be used for realizing LAO/STO devices [108], relies on the realization of a pre-patterned substrate. Photo- or electron- beam lithography is used to define a resist mask, reproducing the desired devices layout, directly on the STO substrate. Then, an amorphous layer (a-LAO, a-STO or AlO_x) is deposited at room temperature. A subsequent lift-off process removes the amorphous material sitting on the resist, leaving an amorphous hard mask on the STO reproducing, in negative, the devices layout. Finally, the LAO thin film is grown on the structured substrate. The grow will take place in an epitaxial fashion on the exposed areas of the substrate, while will lead to an amorphous/polycristalline material in those covered by the hard mask. The 2DEG will be formed only below the epitaxial areas [52] (Fig. 3.2 (a) and (b)). By using this technique, devices with a resolution down to 60 nm have been realized [109]. Also the possibility to obtain more complex structures involving several field effect devices and their use as ring oscillator has been demonstrated [110].

Low energy Ar+ irradiation

Another technique involves the irradiation with low-energy Argon ions [111, 112]. In this procedure, the LAO/STO sample is firstly covered with a resist mask, then low intensity Ar+ irradiation eliminates the electrical conductivity at the interface in the exposed areas, without physical removal of the LAO film. The loss of conductivity in irradiated areas is, in this case, attributed to Ar implantation (Fig. 3.2 (c) and (d)). The spatial resolution achieved with this patterning technique is $\sim$ 50 nm [111].

AFM Writing

Scanning a voltage-biased metallic tip of an atomic force microscope (AFM) over the surface of a "sub-threshold" 3 unit cell thick LAO film enables to locally "write" conducting channels at the interface, with a lateral resolution down to 2 nm (Fig. 3.2 (e) and (f)). The nanowires created with this technique have been used to

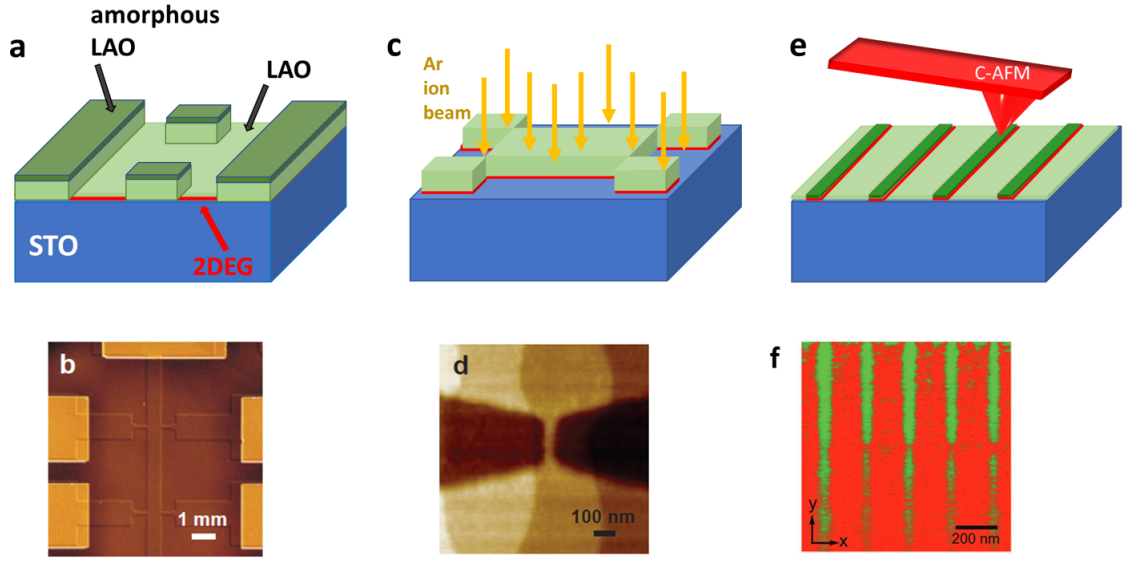

Figure 3.2: Nanopatterning techniques on 2D oxides interface and resulting devices. (a) (b) Amorphous technique [108], (c) (d) Ar+ irradiation [111], (e) (f) conducting AFM [114].

reveal fascinating quantum phenomena in the LAO/STO 2DEG, among which single-electron transistor behavior [113], ballistic transport in electron waveguides [47], and selective difference frequency generation with over 100 THz bandwidth [68]. Although all the techniques briefly described above allowed tremendous advancements in the understanding of oxide interface physics, they present some drawbacks. Firstly, they all result in devices where the 2DEG patterned channels are encapsulated in a crystalline or amorphous matrix, making it impossible to realize a lateral coupling of the oxide 2DEG with other materials, which could be very useful for applications. Moreover, some of them require complex equipment and a challenging set up (such as the conducting AFM writing) and/or involve manipulation of the substrates, with the risk of introducing impurities and contaminants.

In the next paragraph we will show a novel fabrication technique which overcomes such obstacles.

3.3 Nanopatterning of oxide 2D oxides interfaces using low-temperature ion milling

In this paragraph we will show a "top-down" technique to pattern oxide 2DEG down to nanoscale via Ar+ ion milling process. Although developed for LAO/ETO/STO, it can be applied to all types of oxide heterostructures.

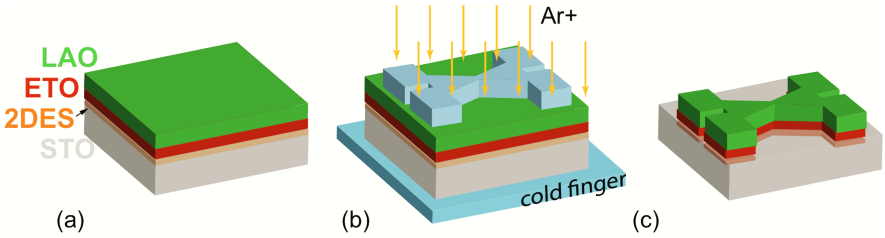

Figure 3.3: Sketch of fabrication process of the LAO/ETO/STO nanodevices: after deposition of the LAO/ETO bilayer (a), a resist mask is realized via photo or electron beam lithography (b). Low temperature ion milling is used to remove the exposed areas of the LAO/ETO bilayer (c) and resist is washed away in an acetone bath.

The process is sketched in Fig. 3.3 [115]. Firstly, a resist mask with the desired layout is realized on a LAO/ETO/STO sample, either by photolithography or electron beam lithography. In the former case, we used a Microposit S1813 resist, with a thickness in the range 600-800 nm. In the latter case, we used a negative tone resist (ma-N2401 from Micro Resist Technology GmbH, Berlin, Germany) with a thickness of 200 nm. We point out that this e-beam resist layer is thicker than what commonly used, in order to avoid damaging of the resist-protected areas during the following steps. The areas not protected by resist are indeed removed via Argon ion milling (Fig. 3.3b)) performed using a 3 cm beam aperture, a beam current of 8 mA and a beam voltage 400 V. These parameters are higher than those used in the Ar+ irradiation process described in the previous paragraph [112]; indeed, in our case, the Ar ions hit the sample surface with high energy, removing physically the sample material. The etching rate obtained is of 2 nm/min for the oxide layers and we are able to remove completely the not protected LAO/ETO areas in 3 minutes of milling. The same milling parameters result in an etching rate for the resist of 20 nm/min. Therefore, the use of an e-beam resist layer of 200 nm ensures that the areas covered are well protected throughout the brief ion milling process.
After ion milling, the protective resist mask is finally washed away in an acetone

bath (Fig. 3.3 c)).
In general, ion milling is not used for the patterning of oxides interfaces, because the impact of the energetic Ar ions with the oxide layers could create defects and, most importantly, oxygen vacancies. The latter, when created in the STO substrate, could form conducting paths in parallel with the 2DEG channels [116]. In order to avoid this, during the Ar+ ion milling process, we kept the samples at low temperature (-140 ° C), gluing them on a cold finger cooled with liquid nitrogen. This caution has been used in the past to realize nanoscale biepitaxial HTS grain boundary junctions [117] and we will demonstrate, that for oxides interfaces, represents an essential aspect to safeguard the structure and insulating properties of the STO substrate.

We have fabricated devices with different geometries, as reported in the AFM images of Fig. 3.4; in particular, nanoconstrictions (Dayem bridges) (panel a), nanochannels with one or two pairs of side gate devices (1S shown in panel b) and 2S shown in panel c)) and multi-terminal devices (panel d). The width of the devices varies in the range 0.15-0.45 μm e length spans one order of magnitude, from 0.15 to 12 μm. Well defined patterns with sharp edges are clearly visible in these images, as well as the terraces on the LAO/ETO bilayer replicating those on the underlying substrate.

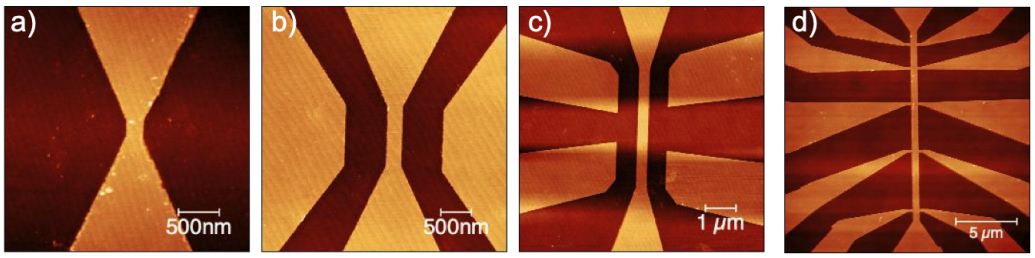

Figure 3.4: AFM topography images of some of the LAO/ETO/STO devices realized: a) a Dayem bridge, b) a side gate device with one pair of lateral electrodes (1S), c) a side gate device with two pairs of lateral electrodes (2S) and d) a multi-terminal device. In the images the lighter areas are the LAO/ETO bilayers, under which the 2DEG develops, while the darker areas are the exposed STO substrate.

3.4 Structural characterizations

In Fig. 3.5 we show contact mode AFM (panels (a) and (d)) and lateral force microscopy images (panels (b) and (e)) acquired in smaller regions of one of the Dayem bridge devices. The line profile across the device (panel (c)) shows that the etched step height is ~6nm, confirming that the LAO/ETO bilayer (10u.c. of LAO + 2u.c. of ETO = 4.7nm) was completely removed by ion milling and that a few nm of the STO substrate surface were also etched away. From panel (a) it is possible to see that, remarkably, the etched area of the substrate still shows its terraced structure. This is also confirmed by the presence of steps in the line profile of panel (c). Panel (d) shows some of these steps on the substrate and from the line profile of panel (f) it is possible to confirm that the step height of each terrace is 3.9 Å, corresponding to the height of one STO unit cell.

In panels (b) and (e) we show the lateral force signal images corresponding to the topography images of panels (a) and (d) respectively (technical details are included in the Appendix A). It is possible to see that the lateral force signal exhibits a similar response on each consecutive terrace, suggesting single atomic termination of the etched substrate terraces. The defects visible in panel (e) have dimensions of few nm on a single terrace (about 2-5 nm wide and less than one unit cell high) and can be associated to pre-existing defects present on the STO single crystal surface (such as imperfect TiO_2 termination) [118] or in the LAO surface, common also to

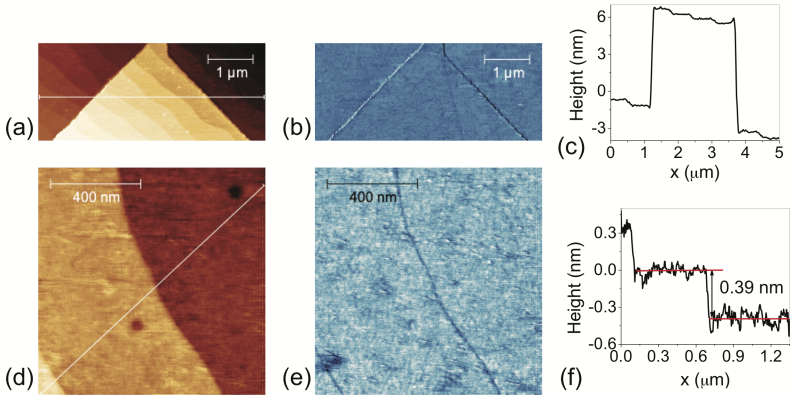

Figure 3.5: AFM topography (a) and lateral force (b) for an etched Dayem bridge device. The images were acquired in contact mode. Panel (c) shows the profile along the white line pictured in the topography image (a). AFM topography (d) and lateral force (e) images on a small area of the etched STO substrate. Panel (f) shows the profile across these terraces (white line in panel d)).

LAO/STO samples [119].
In summary, the data shown in Fig. 3.4 and 3.5 demonstrate that the ion milling process causes minimal structural damage to the etched surfaces.
Now it is important to assess that, besides the crystalline quality, also the insulating properties of STO are preserved after the ion milling and that no conducting paths were created. In order to so, we will present several characterizations, including SQUID microscopy (SSM) measurements and electrical transport measurements as a function of the magnetic field and of the gate voltage.

3.4.1 SSM on LAO/ETO/STO nanodevices

Scanning SQUID microscopy (SSM) is a powerful technique to map the spatial distribution of magnetic fields above a sample surface. As a current-carrying paths will generate a magnetic field (following the the Biot-Savart law) [120], this technique is used to check for the absence of oxygen vacancies-related extra current carrying lines in the STO etched areas.
Fig. 3.6 a) shows the geometry of the sample tested and the scanning SQUID pickup loop capturing field lines near its surface. The conducting LAO/ETO areas are shown in yellow, while in STO substrate is shown in white. Panel b) of the same figure shows the simulation of the magnetic flux pattern in the case of homogeneous conductor with the same geometry. The calculated map shows positive (red) and negative (blue) field lines at the edges of the pattern, and a smooth flux profile inside the current carrying areas. The scanning SQUID data acquired over the patterned LAO/ETO/STO at 4K are reported in panel c). The etched STO areas appear uniform and no distortion of the signal is revealed.
Localized defects are present in almost all oxide interface samples, patterned and un-patterned, as reported by several studies (see for instance ref. [121]). These defects thus are present in the film before the ion-milling process.

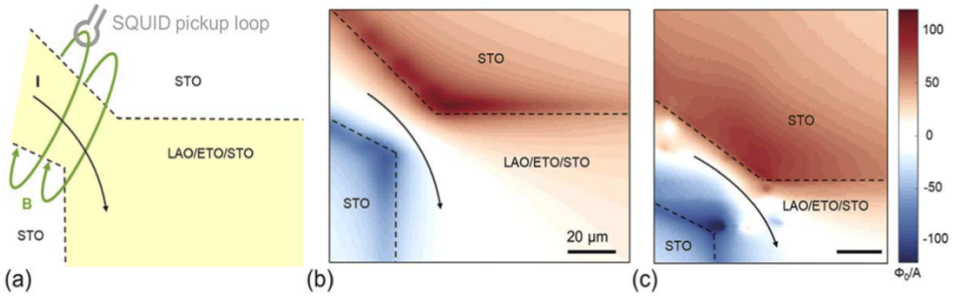

Figure 3.6: (a) Sketch of scanning SQUID pickup loop technique able to capture the field lines near the surface of a current carrying device. In this picture, the device area is shown in yellow color, while the substrate areas are shown in white. Dashed line marks the physical edge of the device. (b) Simulation of the magnetic flux pattern in a homogeneous conductor with the same geometry as the measured LAO/ETO/STO device. (c) Scanning SQUID data over a patterned LAO/ETO/STO device taken at 4 K. Dipole-shaped distortions to the image indicate regions with reduced conductivity.

3.5 Electrical transport of LAO/ETO/STO nanodevices

3.5.1 Hall effect

A further confirmation of the absence of current-carrying paths in the etched STO substrate of our devices comes from the analysis of the carrier concentration. Indeed, oxygen deficient STO-based heterostructures exhibit carrier concentrations

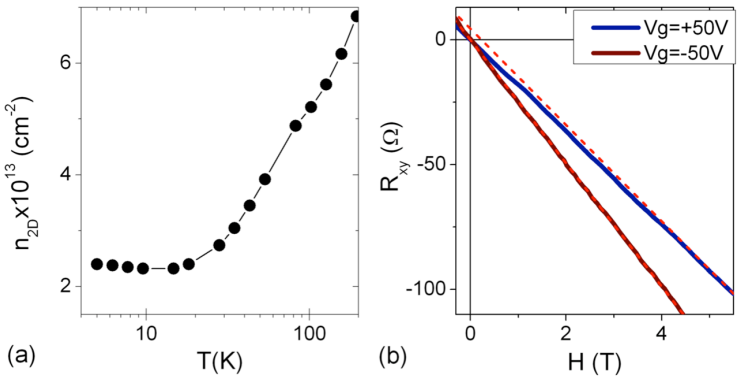

Figure 3.7: (a) Carrier concentration measured vs temperature at Vg = 0. (b) Transverse resistance Rxy at Vg = -50 V (brown line) and Vg = +50 V (blue line) at T = 5 K in perpendicular magnetic field. The red dashed lines are fit around H = 5 T, underlining the presence of a low field curvature at high gate voltage. The data in both panels were measured on large scale Hall bars realized using low temperature ion milling.

range of 10^{14} - 10^{15} cm^{-2} [122], that is one or two orders of magnitude larger than what is found in standard LAO/STO and LAO/ETO/STO samples.
We performed Hall measurements as a function of the back-gate voltage of an Hall-bar shaped LAO/ETO/STO device, realized via photolithography and low temperature ion milling (Fig. 2.10). The carrier density n_{2D} extracted from the measurements decreases with temperature as expected (Fig. 3.7 (a)). At 5 K, n_{2D} is equal to $2.3 \times 10^{13} cm^{-2}$, this is in excellent agreement with data reported in literature for pristine LAO/ETO/STO samples [4, 6, 94]. In addition, the transverse resistances R_{xy} measured at T = 5 K for high values of the gate voltages show, at low field (H~ 2 T), a decrease in the slope, as highlighted by the red dashed lines in panel (b). We have associated this phenomenon to anomalous Hall effect (AHE) as presented in paragraph 2.5 for no-patterned LAO/ETO/STO heterostructures. This result demonstrates that ferromagnetic properties are retained in patterned structures, with the similar characteristics found in pristine samples.

3.5.2 R_{sheet} vs devices size

In order to compare the performances of the different types of devices, and make them comparable also with the data in the literature, it is useful to resort to the sheet resistance R_{sheet} values. In general, this parameter is obtained by multiplying the measured resistance R by a shape factor f related to the sample specific geometry: $R_{sheet} = R * f$. To determine f we performed finite element simulations of our geometries using COMSOL MULTIPHYSICS software, as described in Ref. [53, 100] and in the Appendix C. In Fig. 3.8 we report a collection of R_{sheet} values (measured at 4.2K) as a function of the devices width. The plot in panel a) reports also data from a 500 × 500 μm Hall bar device realized via photolithography and low temperature ion milling. It is important to highlight that the sheet resistance as a function of the channel width is roughly constant. This demonstrates that the electrical transport properties of the devices are comparable to those of the as-grown samples and are not altered by the nanofabrication technique. The small scattering seen in the data can be attributed to defects in the 2DEG, probably deriving from the defects in the STO substrate and in the as-grown LAO/ETO film. Finally, if oxygen vacancies-related conducting channels in the STO substrate were

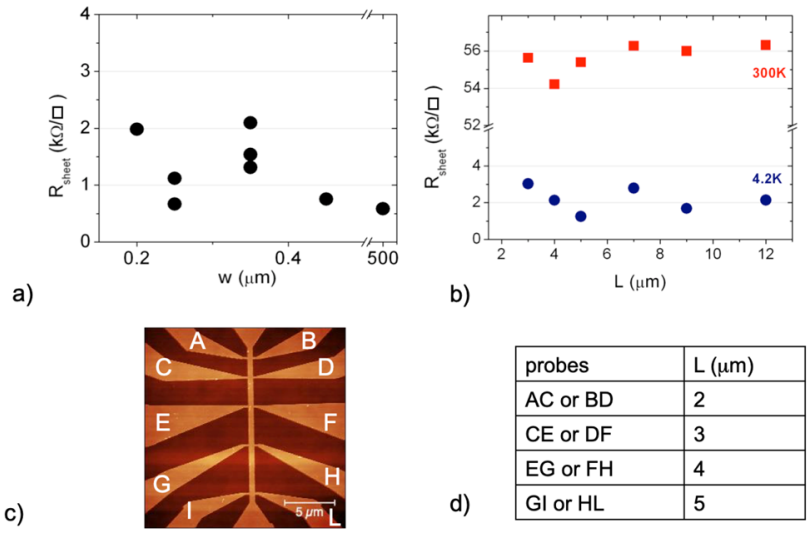

Figure 3.8: (a) R_{sheet} at 4.2 K of devices of different width, ranging from 0.2 to 0.45 μm. The length of these devices ranges from 0.16 to 4 μm. We report also data from a 500 × 500 μm Hall bar device. (b) R_{sheet} at 4.2K (blue) and 300K (red) measured for a multi-terminal device with w = 0.5 μm. Panel (c) shows the voltage probes configuration and panel (d) shows the distance between them.

present, they would add in parallel to the conducting 2DEG. As oxygen deficient STO is known to have a larger number of charge carriers, as mentioned in the beginning of this paragraph, these would effectively shunt the 2DEG channels, resulting in lower resistance, independent from the devices dimensions and, in turn, in a trend in the R_{sheet} vs. width data (as for example reported in Ref. [123]). Finally, panel b) reports the data for a multi-terminal device (Fig. 3.5 d)). This device is composed by a central channel of width w=0.5 μm and a series of voltage probes placed at different distances (see Fig. 3.8 c) and d)). Therefore, by using different pairs of voltage probes at a time, it is possible to measure different sections of the nanochannel. The sheet resistance data in Fig. 3.8 b) indicate a remarkably uniform channel and, again, do not exhibit any dependence on the channel section length.

3.5.3 R_{sheet} vs gate voltage

We now turn to a detailed transport characterization as a function of the gate voltage of the nanodevices. Figure 3.9 (a) shows representative R_{sheet} vs. Temperature

curves of three types of devices. All the devices show a metallic behavior. Panel 3.9 b) reports the tuning of the a Dayem bridge resistance (with w = 200 nm and L = 160 nm) applying a gate voltage in the back-gate configuration. A change of more than two orders of magnitude is observed for a change in the gate voltage of about 40 V, similarly to what obtained for LAO/STO Dayem bridges realized with the amorphous technique [33].

A more efficient tuning can be obtained in side gate devices [53]. The measurement configuration of devices with a pair of side electrodes (1S) is reported in Fig. 3.10 a). This device has w = 0.35μm and L = 1μm. A bias current (I_{bias}) is injected through the conducting nanochannel, while the tuning is performed applying a voltage V_{sg} to the two side gates. In all measurements shown in Fig. 3.10 the gate leakage current is stable and smaller than 2nA. [2] Panel b) of Fig. 3.10 shows that the behavior of the 2DEG can be tuned from metal to insulator with a side gate voltage amplitude ΔV_{sg} of 1.8V. Panel c) shows the modulation of R_{sheet} (at 4.2K) obtained applying the gate voltage V_{sg} to both side electrodes (cyan data) or to one side electrode (left or right) at a time (blue and red data). It is interesting to note that the blue and red data points are in excellent agreement. This means that the nanochannel is remarkably uniform along its width. These results are in

[2] When applying large voltages across a dielectric, it can have some 'losses' due to the emergence of a 'leakage current'. As a result, the voltage drop over the dielectric is not defined: the gate current also flows through the resistive channel defining a small voltage there. This is dangerous for the nanodevices and for applications, it is mainly notorious as one of the major problems in the challenge of scaling up electronics.

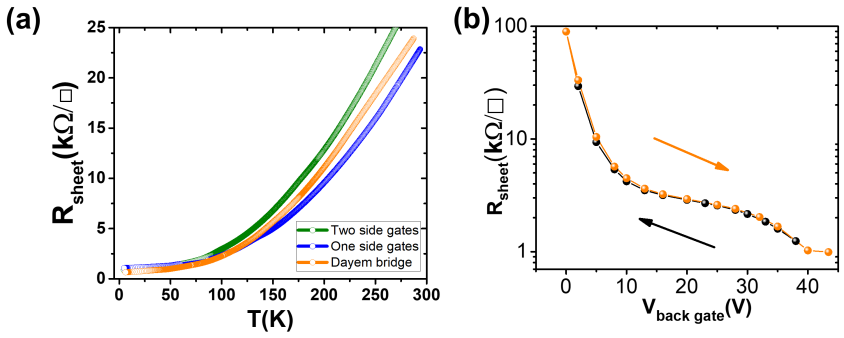

Figure 3.9: (a) R_{sheet} versus T data for different types of LAO/ETO/STO nanodevices. (b) Dayem Bridge R_{sheet} versus Vg data obtained at 4.2 K.

overall agreement with the data of side gate devices realized with the amorphous technique [53, 100]. Finally, the transport properties of two side gate (2S) devices are presented in Fig. 3.11. In this case, the channel has dimensions w = 0.45μm and L = 4μm and can be tuned using two pairs of side electrodes. In particular, by changing the values of V_{sg1} (V_{sg2}), the upper (lower) section of the channel can be tuned (Fig.3.11 a)). Firstly, we show the R_{sheet} vs. Temperature curves obtained applying a voltage to both pairs of side electrodes (i.e. using a gate voltage V_{sg}=V_{sg1}=V_{sg2}) in Fig. 3.11 b). Also in the case, as already reported for device 1S, a metal to insulator transition can be obtained using very small values of the gate voltage (ΔV_{sg} = 0.4V). Fig. 3.11 c) reports the modulation of R_{sheet} at 4.2K in the complete gate range (green data). In the same plot, also the modulation obtained applying the gate voltage to only one pair of side gate electrodes (V_{sg1}, blue data or V_{sg2}, green data) at a time is shown. In this case, the pair of side gate electrode not used in the measurement was grounded. The contour map in panel (d), instead, was obtained changing independently V_{sg1} and V_{sg2}. The symmetry of this last graph is a further proof of the uniformity and homogeneity of the channel. This last

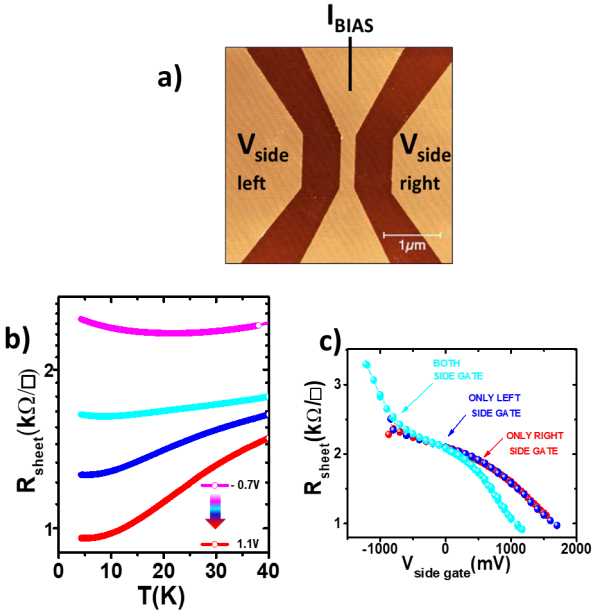

Figure 3.10: a) Sketch of the one side gate geometry (1S) showing the electrical connections for transport measurements. b) R_{sheet} versus Temperature data at several values of the side gate voltage (V_{sg}) c) R_{sheet} data obtained at 4.2 K, applying the V_{sg} to both side electrodes (cyan data) or to one electrode at a time (blue and red data) while the other was kept grounded.

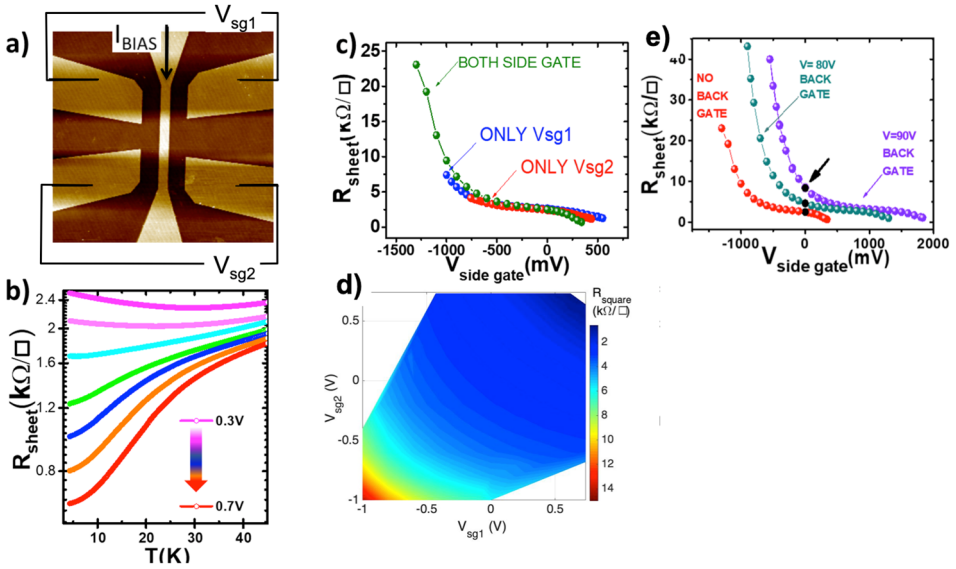

Figure 3.11: a)Sketch of the two sides gate geometry showing the electrical connections for transport measurements. The device has the following dimensions: width=450 nm, length=4μm, lateral electrode width=1.2μm, distance of the electrodes from the center of the channel=0.75μm, distance between the electrodes=1μm b)The R_{sheet} versus T data at several side gate voltages; c) R_{sheet} versus gate voltage applied to both pairs of electrodes (green data) and to one pair of electrodes at a time (blue and red data) (see also sketch in panel a); d) R_{sheet} modulation as a function of the side gate voltage; e) R_{sheet} modulation as a function of the side gate voltage and under the application of a back gate voltage. Data in panels c), d) and e) were obtained at 4.2 K.

result demonstrates the possibility to manipulate independently several sections of the 2DEG channel, promoting the simultaneous emergence of different phases in the same device. Finally, the action of the back gate can be added. The data presented in Fig. 3.11 e) were indeed acquired by firstly setting the back gate, and then changing the value of V_{sg}=V_{sg1}=V_{sg2}. This procedure allows us to change the "zero point" of the 2S device, further expanding the carrier concentration range explored.

3.6 Helium Focused ion Beam on oxide 2DEGs

In this last paragraph we show preliminary results obtained combining the low-temperature ion milling technique with Helium Focused ion beam (He-FIB)).
The focused ion beam technique involves the use of an accelerated beam of ions,

often gallium, which can remove (sputter) material from the sample surface with high spatial resolution (10-15 nm). Recently, FIB systems using Helium ions have

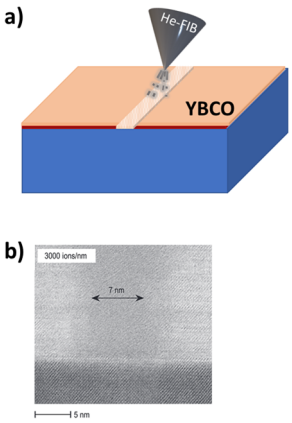

Figure 3.12: (a) Sketch of the FIB technique; (b)Amorphization of YBCO film obtained using He-FIB. Adapted from [124].

been developed, in order to decrease the risk of heavy ion implantation. The effectiveness of He-FIB on oxides has been proven in Ref. [124], where a 30 keV He-FIB was used to irradiate $YBa_2Cu_3O_7$ (YBCO) thin films in order to define Josephson junctions (JJs). The effect of He irradiation was found to be an amorphization of YBCO, which becomes insulator, acting as a Josephson barrier (Fig. 3.12 a) and b)). During this thesis work, we explored the possibility to use He-FIB on oxide interfaces, in collaboration with University of Tübingen where a Zeiss Orion NanoFab He ion microscope in installed. Our experiment is based on the idea that the He-FIB effect on LAO and LAO/ETO should be similar to what reported for YBCO, leading to the amorphization of the LAO overlayer and the consequential elimination of the 2DEG underneath. In order to verify this hypotesis, we realized LAO/STO channels using photolithography and cold ion milling and then irradiated them with He-FIB using several ion doses. The He ion beams were scanned along the width of the channels in order to create micron-size constrictions or tunnel like devices (panels a) and d) in Fig. 3.13 respectively). In the first case, the beam was blanked along the scan, in the second the scanning was continuous. In Fig. 3.13 we show our preliminary results. Panel b) shows resistance vs. temperature curves for constrictions realized using several doses. The width of the constrictions is 5 or 10

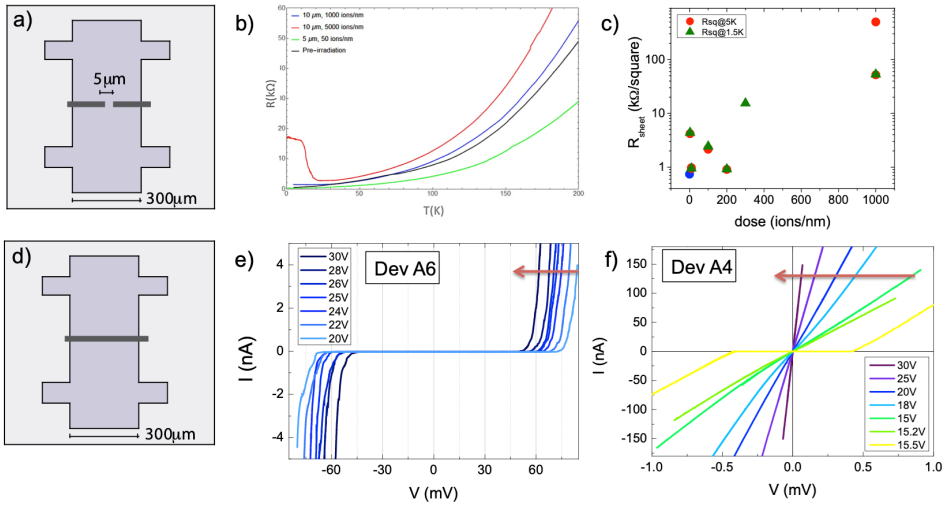

Figure 3.13: (a) constriction geometry; (b) Resistance vs. Temperature behavior for 3 He-FIB irradiated LAO/STO costrictions compared with the same sample before irradiation. The width of the constriction is 5 and 10 μm; (c) Sheet resistance as a function of the ion dose of the constrictions; (d) tunnel-like geometry; (e) I-V characteristic of device A6 realized with a dose of 1000 ions/nm measured for several values of the gate voltage; (f) I-V vs. Vg characteristics of device A4 realized with a dose of 150 ions/nm. Both devices were measured at T= 0.3K.

μm. We observe that the metallic behavior of the interface is preserved for doses below 300 ions/nm, as confirmed by the analysis of the sheet resistance R_{sheet} vs. dose of panel c). Panels e) and f) show the results obtained on the second type of device, where the irradiation was performed along a continuous line in order to create tunnel-like barriers (see sketch in panel d)). In particular, panel e) shows the current vs. voltage (I-V) characteristics of device A6 where a dose of 1000 ions/nm was used to create a barrier. The behavior is typical of a tunnel junction, with zero conduction below a critical voltage value and a sharp increase in the current when such threshold is reached. The voltage threshold can be modulated using back gate. The data in panel (f), instead, show the same measurements on a device realized using a lower dose (device A4, 150 ions/nm). Also in this case the gate voltage can modulate the I-V characteristics but, this time, in a more dramatic way. At low gate voltage, the same tunnel-like behavior seen for device A6 is reproduced whereas, increasing the gate voltage, a transition to a metallic-like I-V is achieved. Therefore a complete tunability of the tunnel barrier is demonstrated.
We have also measured the A4 device down to dilution temperatures (using low noise electronics as presented in Appendix B). The current-voltage (I-V) charac-

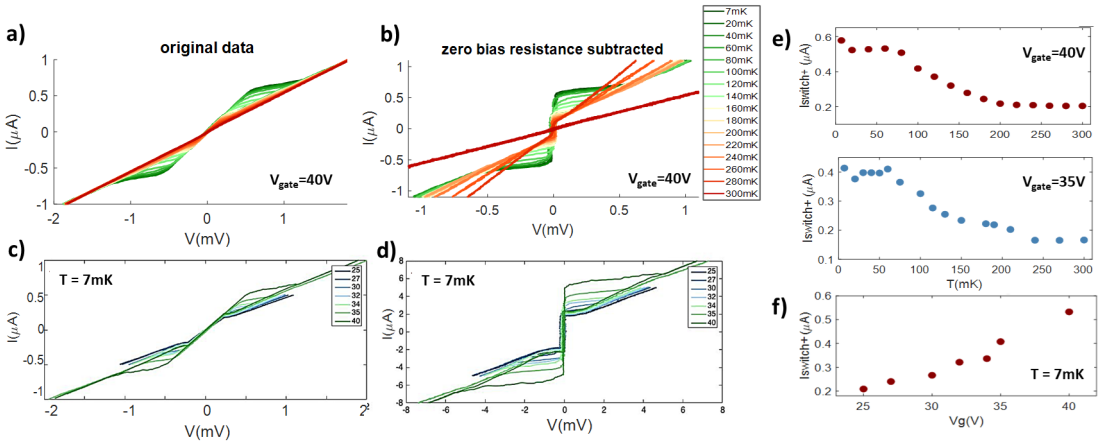

Figure 3.14: (a) I-V characteristics from 300 mK to 7 mK and with back gate voltage of 35V of device A4. At zero bias, a series resistance is present, and by subtracting it (b) typical I-V characteristics of a Josephson junction is obtained. c), d) I-V characteristics at 7mK with several back-gate applied. (e) Temperature behavior of the switching current with back gate of 40V and 35V; (f) Gate behavior of the switching current at 7mK.

teristics of the A4 device at several temperatures and at back gate voltage of 35V is reported in Fig. 3.14. At low voltage, the I-V characteristics as a function of temperature show a finite resistance, instead of the supercurrent branch (panel a)). This is likely due to high resistive contacts of the device. Indeed, if the low voltage resistance is subtracted from the data, non-linear I-V characteristics, reminiscent of those typical of Josephson junctions, are obtained (Fig.3.14 b)). In panels c) and d) the I-V characteristics at 7 mK are reported as a function of the back-gate voltage. Also in this case, a zero bias resistance was subtracted from the data (panel d)). Finally, in panel e) we report the switching current extracted after subtraction of the zero bias slope for two values of the gate voltage and in panel f) we plot the temperature behavior of the switching current. These characteristics are very similar to those obtained for LAO/STO JJs devices realized with the amorphous technique [33]. In particular, we notice that the I_{switch}(T) data are very similar to the two-gap fit model of LAO/STO JJs. These preliminary results are very encouraging for the application of He-FIB for fabrication of 2D oxide based devices and for study of unconventional superconductivity in LAO/STO JJs.

3.7 Conclusions

In summary, in this Chapter we presented a "top-down" fabrication technique, based on low temperature ion milling, for the realization of nanoscale LAO/ETO/STO devices. By keeping the samples at low temperature during the Ar+ ion milling process, the formation of oxygen vacancies in the STO substrate is avoided. On the other hand, the samples realized with ion milling at room temperature show a conductive STO substrate as shown in the appendix A.
The absence of oxygen-related current carrying paths in the STO has been assessed using several techniques:

- Hall effect measurements show that the carrier concentration in the patterned samples realized is comparable to that typically found in pristine LAO/ETO/STO interfaces
- Using scanning SQUID measurements, we have confirmed the absence of current flow outside the patterned LAO/ETO/STO areas
- The realized nanochannels are tunable using side gate electrodes. This can be possible only in the case that no conducting paths are present on the surface of the etched STO areas separating the channel from the gate electrodes.

The technique presented shows many advantages, compared to those used up to now for patterning of oxide 2DES described in section 3.2. Being a "top down" approach, it does not involve manipulation of the substrate and for this reason it is attractive for the patterning of every kind of interfacial systems, including those where termination and cleanliness of the substrate is a fundamental aspect. Furthermore, this technique can be applied also to pre-tested heterostructures, increasing the yield of the nanofabrication procedure. However, the major advantage it brings is that it is the only technique which allows to expose the lateral sides of the devices and to access the oxide 2DEG from the side. This opens the way to the realization of hybrid devices, where the oxide 2DEG is coupled to other materials of interest for advanced electronic applications, such as superconducting materials and semiconducting nanostructures.
Finally, we showed preliminary results of further structuring of devices using He-

FIB. A complete characterization of these last devices will require several future expriments; however, the complete modulation of the nanoscale barrier achieved is extremely promising.

CHAPTER 4

TUNING MAGNETIC INTERACTIONS IN LAO/ETO/STO 2DEG USING LIGHT

Electric field effect is a well established tool to tune the transport regime of STO-based 2DEG. Recently, however, another possible tool has emerged for these systems: visible light. Here we investigate the combined effect of light and field effect to tune the properties of LAO/ETO/STO interfaces, with particular attention to the ferromagnetic correlations. We will also explore the response of oxide 2DEG to infrared radiation, which is of great relevance for electronic applications.

4.1 Photo-response of LAO/STO

Electric field effect is of paramount importance both for the study of STO-based 2DEG properties and for the design of oxide-based electronic devices. However, it is not the unique way to manipulate oxide 2DEG system. As a powerful external perturbation, light also can modify the transport properties of these systems [99]. Recently, photoconductivity of oxide 2DES has drawn a lot of attention due to the demand for optoelectronic devices such as optical switches, photo-detectors, holographic memory, etc [126, 129–132].

Photoconductivity (i.e. changing in the conductivity of a material under the absorption of light at suitable wavelength) can depend on two mechanisms: the intrinsic photoelectric effect, if light favors the promotion of electrons in the conduction band, leaving behind holes in the valence band; and the extrinsic (i.e. doped) photoelectric effect, where the excitation of shallow impurity levels is involved.

In STO-based interface systems, photoconductivity has been reported when using light in a wide wavelength range going the infrared to the near ultra-violet [99].

Fig. 4.1 reports some results on LAO/STO published in the recent years. Panel

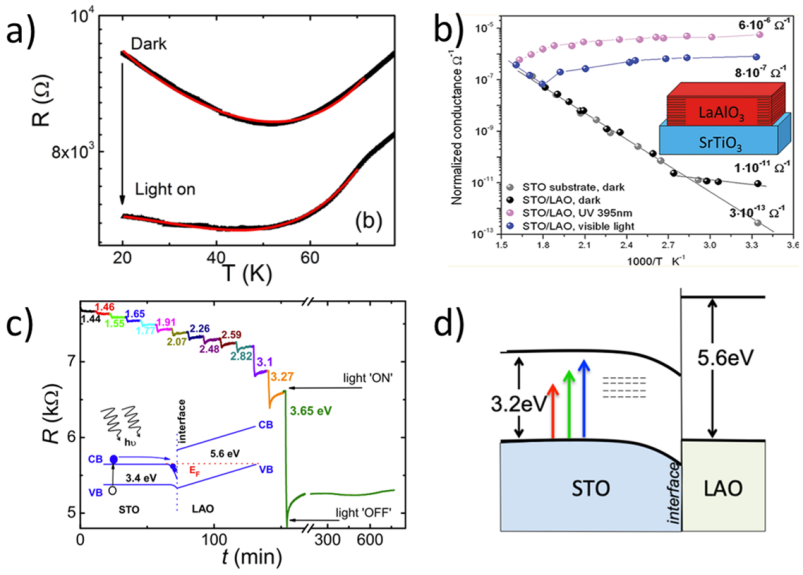

Figure 4.1: a) Resistance versus temperature curves of the heterointerface with and without the UV light irradiation [125], b) Normalized photo-induced conductance at STO or and LAO/STO kept in dark or illuminated with a 395 nm UV lamp (pink dots) or visible light (blue dots) [126], c) Resistance as a function of time during the illumination with the photons energy from 1.44 eV to 3.65 eV at 4.2 K. Each change in the photon energy results in a step in the resistance [127]. d) Sketch of the band diagram of LAO/STO.

a) shows an example of the resistance versus temperature curve of a LAO/STO sample before and after exposure to UV light with the wavelength of 365 nm [125]. Panel b) shows that the modulation of the resistance under UV and visible light takes place also at room temperature [126]. Panel c) shows the temporal evolution of the resistance during the illumination with different photon energies. In all experiments, the modulation of the resistance was found to persist after the illumination is interrupted (persistent photoconductivity). The simplified band diagram shown in panel d) can be used to understand the origin of photoconductivity in LAO/STO. STO posses a band gap of 3.2 eV. Therefore, promotion of electrons from the valence band (VB) to the conduction band (CB) should take place only when the system is irradiated with light having energy of the UV radiation or larger. However, surprisingly, a sizable photoconductivity effect is measured also for irradiation with visible light (panels 4.1 b) and c)), although the efficiency in this case is reduced. The reason for such behavior could be found defects-related in-gap states which reside 1.3 eV below the CB of STO (represented with dashed lines in the sketch of panel d) of Fig. 4.1) [133, 134]. These states can be excited by energies lower than the gap, promoting photoconductivity under light in the visible spectrum. This explanation is confirmed by the observation that the change is resistance observed under illumination with visible light (Fig. 4.1 b) and c)) is in general reduced compared to what happens under UV light. When the light is

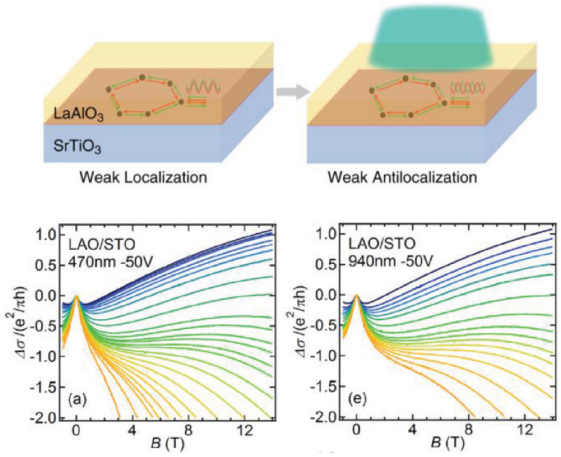

Figure 4.2: Magnetoconductace curves of LAO/STO after repeated illumination steps with different wavelength (470 and 940 nm). The darkest blue are the initial curves (pristine state) and the darkest red are the curves after around 25 times illumination. Adapted from Ref. [128]

turned off, the photo-generated electrons that are moved to the quantum well at the interface do not come back immediately to the original state. The recapture rate of these defect-related carriers is quite low [116]; characteristic relaxation times have been estimated in the order of 10^4 seconds. The case of LAO/STO may be compared with GaAs/AlGaAs heterostructures, where the persistent photoconductivity is ascribed to the spatial separation of the electron-hole pair under the effect of the local confining electric field [135].
Photo-gating has been used also to tune the SOC at LAO/STO interfaces, as shown in Fig. 4.2 [128]. Increasing the carrier concentration with light, by means of repeated illumination steps, a transition from a transport regime characterized by weak-localization (WL) to one characterized by SOC-induced weak anti-localization (WAL) takes place. This transition is similar to that obtained using electric field effect [17, 100].
The observation of photoconductivity and SOC modulation in oxide 2DEG can open opportunities for these systems in the field of optoelectronics. Even more exciting are the possibility offered by photoresponse combined with ferromagnetism for novel magneto-optical devices. In the following paragraphs we will investigate the behavior of the spin-polarized LAO/ETO/STO 2DEG under the combined effect of visible light and field effect.

4.2 Photo response of LAO/ETO/STO

We investigated the photoresponse of LAO/ETO/STO 2DES due to visible light irradiation. The samples were patterned using photolithography and low-temperature ion milling as described in paragraph 3.3, in order to realize well defined channels with width of 500μm. The irradiation was performed using commercially available light emitting diodes (LEDs) mounted inside the cryostats and in proximity to the samples surface. The LED lights peak wavelength λ are listed in Table 4.2. We point out that the emission spectrum of the LED sources, as declared by the manufacturers, includes some dispersion around the dominant wavelength. In the Table we report this information as spectral line half width ($1/2\Delta\lambda$). Therefore the range of wavelengths includes photons from the near-IR to the near-UV range. The use of commercial LED sources, which are less selective in the illumination

wavelength compared to laser sources, has the advantage of ease of use for future applications. In particular, the illumination with LED lights do not require optical access for the measurement cryostat.
Table :

LED LIGHT COLOR	λ(nm)	Energy (eV)	(1/2)$\Delta\lambda$ (nm)
Red	655	1.89	20
Blue	525	2.36	15
Green	470	2.63	10
White	from 450 to 650	from 2.75 to 1.9	

4.2.1 Modulation of the resistance under visible light

In Fig. 4.3 we show the typical evolution of the normalized sheet resistance $\Delta R_{sheet} = (R_{sheet} - R^{OFF}_{sheet})/R^{OFF}_{sheet}$ (with R^{OFF}_{sheet} the sheet resistance before illumination) of a LAO/ETO/STO sample as a function of illumination time at 5K. A qualitatively similar behavior was observed for all the light wavelengths listed in Table 4.2 and for all the gate voltages used. The horizontal axis was set to 0 at the switch on of the LED sources. The normalized sheet resistance ΔR_{sheet} shows an exponential-like decrease, with most part of variation taking place in the first first 3 minutes of illumination. When the LED source is switched off, ΔR_{sheet} shows

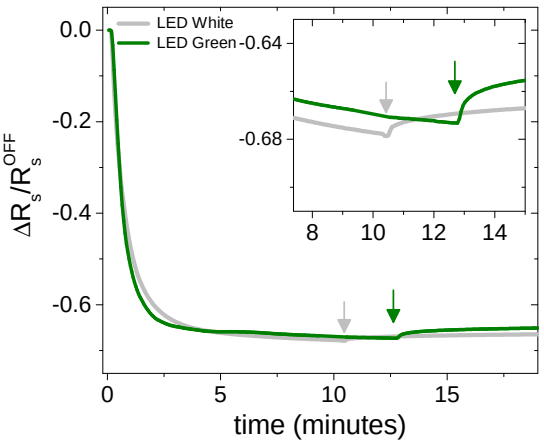

Figure 4.3: Examples of sheet resistance R_s versus time of a LAO/ETO/STO Hall bar device under visible light illumination at 5K. The inset shows the small recover of the Rs upon switch off the LED source.

a small recover, as reported in the inset of the Fig. 4.3. Similar trends have been reported for several oxide 2DEG systems based on STO under UV and visible light illumination [125, 136, 137] .

In Section 2.4, we showed that indications of ferromagnetic coupling are visible in the Resistance vs. Temperature curves of LAO/ETO/STO as an increased slope below 10K. We now analyze this feature of the R vs T curves when the samples are illuminated with visible light. All the measurements reported in this section were performed following the same illumination protocol and repeated for all the light wavelengths of Table 4.2, similar to that reported in Ref. [128]:

1) Cool the samples to base temperature;

2) Apply a positive back gate voltage;

3) Illuminate the sample with the LED light for 5 minutes;

4) Switch off the LED light and wait for 10 minutes;

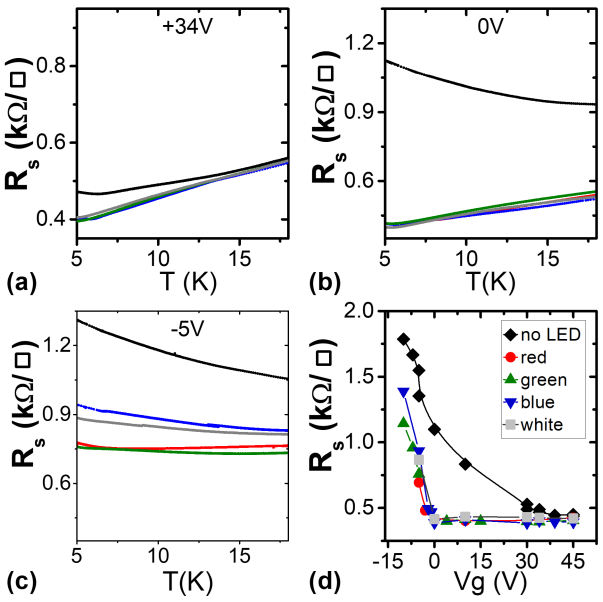

Figure 4.4: Panels (a) to (c): Resistance versus Temperature for LAO/ETO/STO Hall bar measured at $V_g = +34V$, $V_g = 0V$ and $V_g = -5V$ respectively. Black data are acquired in the absence of LED illumination, whereas red, blue and green data are acquired after illumination with LED of the corresponding color (see also legend in panel (d)). Gray data refer to illumination with white LED. Panel (d) shows R_{sheet} at 5K as a function of the gate voltage after photodoping.

5) Start the measurement ramping up the temperature at the rate of 1K per minute.

In order to provide consistent analysis, the feeding power to the LED source was set at the same value for all LED types and kept constant throughout all the illumination time. At this power the change in the sample temperature, measured by a sensor in close contact, is smaller than 0.5K. Panels (a) to (c) of Fig. 4.4 show the R_{sheet} vs T for a LAO/ETO/STO channel obtained applying positive, zero and negative gate voltages respectively. The back gate configuration was used in this case. In each panel, the data in the pristine (state before illumination) are shown in black, whereas those measured after illumination are shown in red, green, blue and gray following the color of the LED light used (grey data refer to illumination with white light).

We notice that for $V_g \geq 0$, R_{sheet} drops, upon illumination, to the value of 400 Ohm regardless of the gate voltage values and of the light color. On the other hand, for $V_g < 0$ the resistance value reached upon illumination is substantially larger and changes with the light color. These observations are condensed in panel (d) of the same Figure, showing R_{sheet} as a function of the gate voltage at 5K for the several light colors used.

A closer inspection to the data shown in panels (a)-(c) reveals that, upon illu-

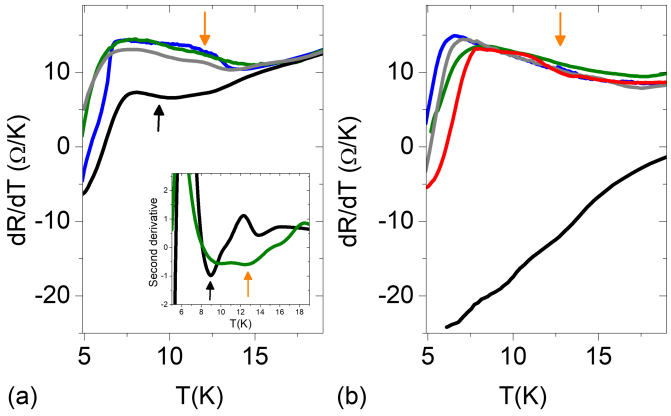

Figure 4.5: Derivative of the Resistance versus Temperature for LAO/ETO/STO measured at $V_g = 34V$ (a) and $V_g = 0V$(b). Black data are acquired in the absence of LED illumination whereas red, blue and green data are acquired after illumination with LED of the corresponding color. Gray data refer to illumination with white LED. In the inset, the second derivative is plotted for LAO/ETO/STO measured at $V_g = 34V$ in absence of LED (black curve) and under green LED (green curve).

mination with the visible light, a change of slope also appears in the R_{sheet} vs. T data below 10K. In order to better evaluate such change, Fig. 4.5 shows the derivative of the data of panels (a) and (b) of Fig. 4.4. The black arrow in panel (a) indicates the upturn in the dR/dT curve, corresponding to an increased slope of the R_{sheet} vs T curve, of the data acquired at V_g = 34V. After light illumination, this upturn becomes more evident and shifts to higher temperature, indicating increasing ferromagnetic coupling (orange arrow). This behavior is confirmed by second derivative (insert of Fig. 4.5 a)). A similar increase in the ferromagnetic temperature was obtained using electric field effect in Ref. [94]. The pristine R_{sheet} vs T curves measured at V_g = 10V (black data in Fig. 4.4 (b)), on the other hand, show no indications of ferromagnetic effect, as seen in the monotonous derivative of Fig. 4.5 (b). However, when the LEDs are switched on, a clear change in the slope appears (orange arrows in Fig. 4.5).

4.2.2 Magnetotransport under visible light

In this section, we will show a more quantitative evaluation of the tuning of ferromagnetic transition in LAO/ETO/STO with visible light.
In paragraph 2.5, we described how, for ferromagnetic conductors having spin-orbit coupling, the transverse resistance shows an additional term, called anomalous Hall component, which depends directly on the magnetization of the material. Fig.

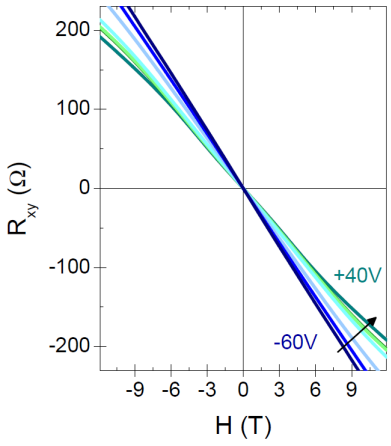

Figure 4.6: Hall effect measured for different values of the gate voltage, from -60V (dark blue data) to +40V (dark green data).

4.6 shows transverse resistance R_{xy} curves measured on a LAO/ETO/STO sample at several values of the gate voltages. It is clearly visible that, at low values of the gate voltages, the R_{xy} vs H curve is linear, whereas increasing the gate voltage, we see an upward curvature at high field (H > 6 T) related to the activation of multiband transport [13, 138] and a downward curvature at low field (H < 4 T) due to the anomalous Hall component [70, 72].
We will now demonstrate that this anomalous component can be modulated using visible light. Also in this case we have defined a measurement procedure:

1) Cool the samples to base temperature;

2) Apply a positive back gate voltage;

3) Illuminate the sample with the LED light for 2 minutes;

4) Switch off the LED light and wait for 10 minutes;

5) Start the measurement ramping the magnetic field

6) at the end of the field sweep, switch on again the LED for 2 minutes and repeat the steps 3) to 5).

This protocol gives the access to several values of the carrier concentration at fixed values of the gate voltage.
In Fig. 4.7 we show Hall effect measurements with negative (V_g = -20V) and positive (V_g = 60V) gate voltage (panels (a) and (d) respectively). The three curves measured for each V_g are obtained after subsequent illumination steps (see the above protocol) using blue and red light respectively. The arrows in the picture indicate the direction of increasing illumination time. In order to highlight the presence of an Anomalous Hall component, we subtract from the curves the linear component calculated around H ~ 4 - 5T; the resulting curves are shown in panels (b) and (e). The Anomalous Hall component values (R_{AHE}) can be estimated from the plateau in these curves and are reported in panels (c) and (f) as a function of the carrier concentration (calculated from the slope of the corresponding R_{xy} curves at high field (H > 6T)).
As expected, the data show that R_{AHE} increases with increasing the illumination

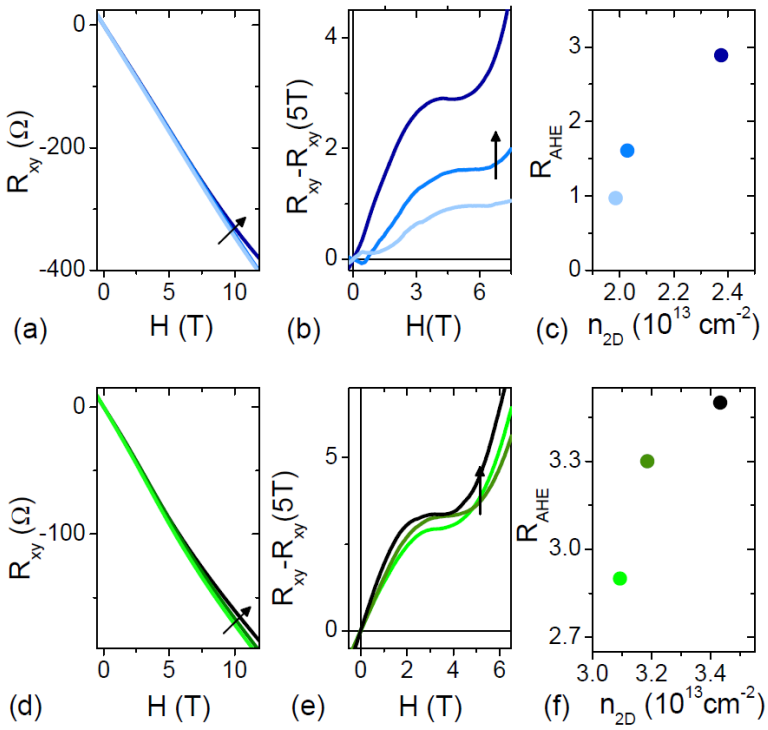

Figure 4.7: Hall effect measured for different values of the gate voltage, from -60V (dark blue data) to +40V (dark green data).

time, together with carrier concentration. In particular, we notice, from the data in panel (c), that when visible light induces an increase of the carrier concentration above the critical value $n_c = 2\times10^{13}cm^{-2}$, ferromagnetic coupling is activated in the heterostructure. We have demonstrated indeed that above this carrier concentration value, $d_{xz,yz}$ carriers are promoted into the conduction band and, thanks to their dispersion along the z axis perpendicular to the interface, can couple with Eu spins of the uppermost ETO layer, leading to spin polarization (see paragraphs 2.2 and 2.6) [70].

This result confirms that the ferromagnetic transition can be activated in the heterostructure using both electric field effect and visible light.

Finally, we have measured the magnetoresistance under LED light. In paragraph 2.7, we have shown that ferromagnetism, tuned by gate voltage in LAO/ETO/STO, masks the SOC-induced weak-antilocalization (WAL) corrections to the magnetoconductance. However, by using gate voltage, a complete suppression of such corrections was not reached. We will now add visible light to boost ferromagnetic

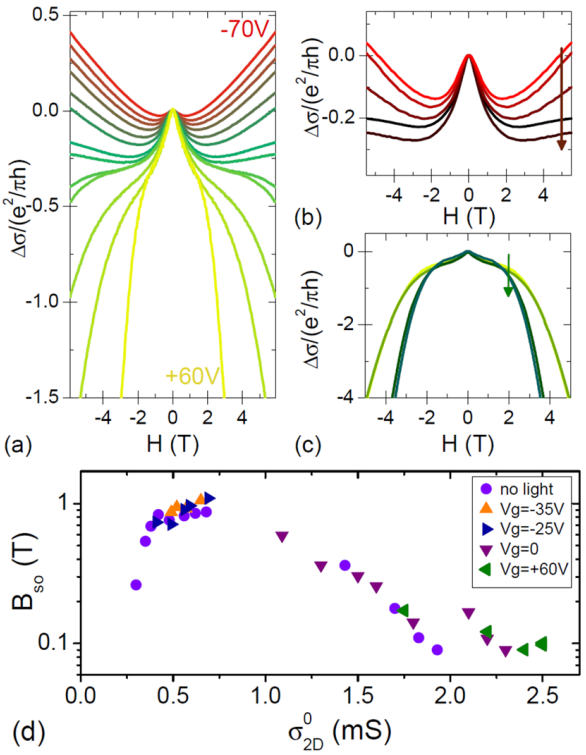

Figure 4.8: Panel (a): Differential magnetoconductance $\Delta\sigma$ of LAO/ETO/STO heterostructure as a function of the gate voltage. Panel (b): $\Delta\sigma$ obtained at fixed gate voltage V_g=-35V after subsequent illumination steps. The arrow indicates the direction of increasing illumination time. The green curves in panel (c) show the same as (b) for V_g=+60V. The blue curves in the upper part of the panel show the magnetoconductance data after subtraction of the classical component. Panel (d) shows the spin-orbit field B_{so} extracted from magnetoconductance curves as a function of sheet conductance.

coupling and expand the transport range to investigate the FM-SOC interplay. Panel (a) of Fig. 4.8 displays normalized differential magnetoconductance curves at T = 2K for different values of the gate voltages between -70V and +60V measured in perpendicular magnetic field. The passage from largely positive magnetoconductance at low gate voltage (weak localization - WL) to completely negative magnetoconductance at high gate voltage (weak anti localization - WAL) is visible (paragraph 2.7). We fit the magnetoconductance curves shown in Fig. 4.8 (a) using the Maekawa-Fukuyama (MF) model, following the [94, 100] (Appendix C). The analysis reveal that spin-orbit field B_{so} parameters obtained from the fitting follow the behavior already shown in paragraph 2.7: initially it increases with increasing sheet conductance σ_0^{2D}, similarly to what happens in LAO/STO; then at σ_0^{2D}= 0.7mS, B_{so} reaches its maximum value and starts to decrease. Indeed, σ_0^{2D}= 0.7mS

corresponds to n_{2D}=n_c and to the activation of ferromagnetic effects, which mask WAL corrections.

We turn now to the evolution of the magnetoconductance curves under visible light. Panels (b) and (c) of Fig. 4.8 show curves at fixed values of the gate voltage (V_g = -35V and +60V respectively) after subsequent illumination steps, following the same protocol used for Hall effect measurements. As indicated by the arrows in the panels, the increasing illumination time shifts the conductance curves, similarly to gate voltage effect. Therefore, in panel (d), for each value of the gate voltage, several B_{so} values are reported after fitting of the magnetoconductance curves. We see that the the B_{so} values obtained under illumination follow the trend already reported for the pristine state. However, for the data at high conductance the B_{so} values seem to saturate to very low values, which probably correspond to the sensitivity of our fitting procedure. In order to get a better insight in this high conducting

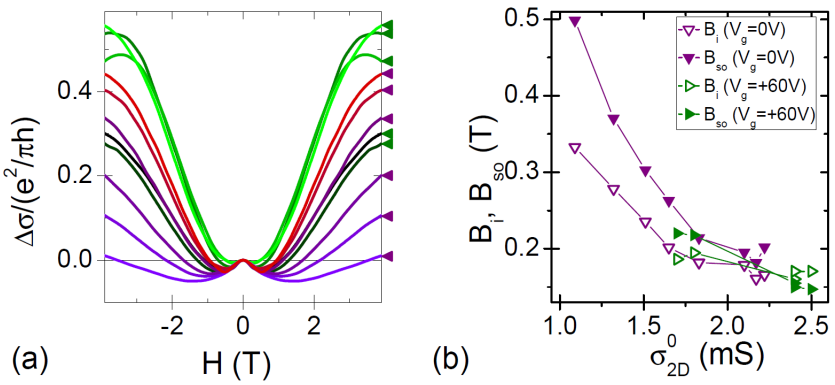

Figure 4.9: Magnetoconductance curves achieved at V_g = 60V (green arrows) and V_g=0V (purple arrows) for subsequent illumination steps, after subtraction of a parabolic component. Panel (b) shows the comparison between the inelastic field B_i (open symbols) and spin orbit field B_{so} (full symbols) obtained by fitting the curves using the MF formalism. Purple data refer to V_g=0V and green data refer to V_g=+60V.

regime, in Fig. 4.9 (a) we report the magnetoconductance curves obtained during subsequent illumintion steps keeping the gate voltage fixed at V_g= +60V (green arrows) and at V_g = 0V (purple arrows) after subtraction of a parabolic background from the data, related to the classical component to the magnetoconductance (as reported in [94]). Repeated illumination steps lead to a progressive reduction of the negative part of the differential magnetoconductance, around zero field. Fig. 4.9 panel (b) shows the spin-orbit field B_{so} (full symbols) and inelastic field B_i (open symbols) parameters extracted from fits as a function of sheet conductance

σ_0^{2D}. Increasing σ_0^{2D} (which correspond to increasing carrier concentration) the values of B_{so} and B_i tend to approach and eventually crossover. We point out that this crossover cannot be obtained using only the gate voltage to tune the carrier concentration [94].

4.2.3 Discussion

In summary, by means of systematic transport measurements, we have demonstrated that it is possible to modulate magnetic coupling in LAO/ETO/STO 2DEG by using visible light illumination. The energies of the visible radiations used in the present experiment (see Table 4.2) reside well below the STO band gap (3.2eV, see sketch in Figure 4.1), so a direct promotion from the valence band (VB) to the conduction band (CB) should be excluded. In the case of LAO/STO interface, as discussed in paragraph 4.1, sub-gap photo-promotion has been explained taking into account the presence of in-gap states 1.3 eV below the CB, originating from oxygen vacancies [128]. These states are clearly visible in the angle integrated angle-resolved photoemission spectroscopy (ARPES) data shown in Fig. 4.10 (lower panels) [70]. In the upper panel of the same Figure, we report also data from LAO/ETO/STO. In this case, a large Eu $4f$ peak is visible around 2eV. These

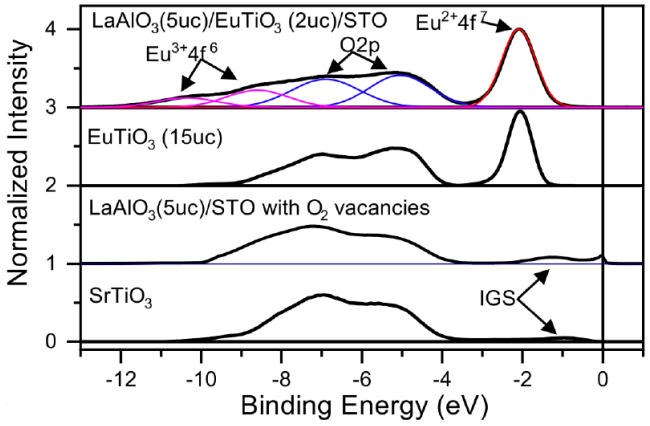

Figure 4.10: Angle integrated ARPES VB data of STO, and ETO 2DEG surface state, compared to angle and photon-energy integrated RESPES VB of (001) LAO(5uc)/STO (containing oxygen vacancies) and LAO(5uc)/ETO(2uc)/STO heterostructures. Multiple gaussian fit of the LAO/ETO/STO VB profile is used to determine the Eu3+/Eu2+ ratio. The in-gap states is observed only in STO and LAO/STO 2DES due to the presence of oxygen vacancies. Adapted from [70].

states could therefore contribute to the response of LAO/ETO/STO under visible light. This point is of great importance because, as reported in section 2.2, Eu $4f$ states couple with Ti-$3d$ states, promoting spin-polarization in the 2DEG. This means that light illumination could be a very efficient tool to boost ferromagnetic correlations in this 2DEG. However, more detailed experiments are needed to discriminate the nature of the carriers promoted and to fully explain promotion mechanisms.
The presented tunable photo-response properties at oxide interfaces open the possibility to the creation of an oxide based photoelectric platform.

4.3 Tuning of LAO/STO using infrared light

In the last section of this Chapter we will present initial results on the response of oxide 2DES under infrared light. The infrared radiation is interesting because optoelectronic devices that operate in the near- and mid-infrared range are currently used for sensing, telecommunication and are attractive for the intra/inter chip optical interconnections. Moreover, the 1550 nm spectral region is a widely used wavelength in optical communication systems, thanks to the low absorption characteristics of the glass material used in fibers at this wavelength. The propagation losses (fiber attenuation) expressed in decibels per kilometer (dB/km) are particularly important for long-distance links. For single-mode fibers operated in the 1550 nm spectral region, they are often of the order of only 0.2 dB/km. Multi-mode fibers typically show higher values in the 1550 nm region, and largely higher attenuation is obtained for operation at short wavelengths. Therefore an exciting challenge is to develop methods for measuring actuation, especially at the nanoscale order, for the optoelectronics development.
In this paragraph, we present our preliminary experimental results concerning the photoresponse of LAO/STO nano-constriction (Dayem Bridge) exposed to optical fiber laser at 850 nm and 1550 nm wavelength, operated at temperatures of T = 4.5 K. For these experiments, a cryogenic system with optical access was used. These results pave the way for the exploration of the response of LAO/ETO/STO in the infrared regime.
We have fabricated LAO/STO Dayem Bridge width 200 nm and length 160 nm

using the patterning procedure presented in paragraph 3.3. The geometry of the devices is identical to that presented in Fig. 3.5 a). In Fig. 4.11, we plot the resistance as a function of time during subsequent illuminations with 850 nm light (power ~ 200 nW). We observe that, when the laser is switched on, the resistance quickly drops to to 55% of its initial (pristine) value. This large drop is partially recovered when the laser is off, leading to a final variation in the resistance value of ~30%. This persistent photoconductivity is similar to what already observed for illumination with visible light. When the laser is switched on again, the change in the resistance amounts to ~20%. These results are extremely encouraging, also considering the low power of the light source used.
In Fig. 4.12 we show the results obtained using a laser source with wavelength 1550 nm. The several panels correspond to the response of our samples when decreasing the power of the incident radiation with the help of fiber optical attenuators inserted in the optical system (see Appendix B). In all case studied, the resistance quickly decreases to a minimum value when the light is turned on and then shows a small recovery at the switch off of the irradiation. It is important to note that the memory of the first irradiation is retained even after several light on-off cycles. We point out that a sizable change in the resistance (around 10%) can be obtained also with powers in the microWatt range, as condensed in panel e) of Fig. 4.12. The obtained results open the prospect of realizing photon detectors based oxides interfaces. However, they offer also the possibility to infer interesting

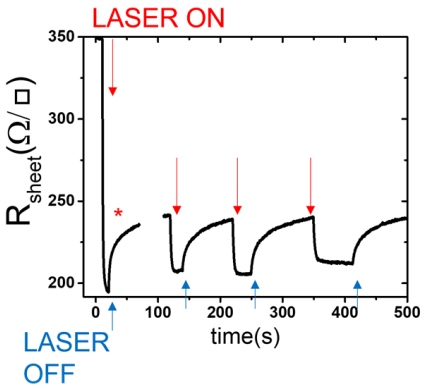

Figure 4.11: Time dependence of the sheet resistance under illumination of 850 nm at 4.5K. *Under the first irradiation shows the persistent photo-induced effect and then a balanced state.

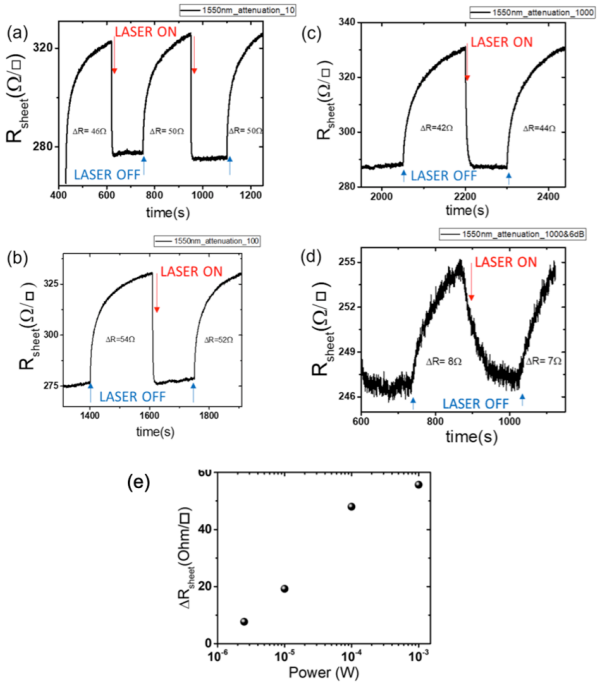

Figure 4.12: Time dependence of the sheet resistance under several 1550 nm laser power, a) 10^{-3}W b)10^{-4}W c)10^{-5}W d)3 X 10^{-6}W at temperature of 4.5K. Panel (e) summarizes the change in the resistance as a function of the laser power.

information on the oxide 2DEG band structure. Using IR light, we moved to lower photon energies. The 1550 nm radiation, for instance, correspond to 0.8 eV photon energy. Looking at the bottom panels of Fig. 4.10, we can conclude that the change in the resistance under this type of light can only be ascribed to the effect of in gap-oxygen states. In the case of LAO/ETO/STO, on the other hand, no states are visible for such low energies, therefore the IR light should have no effect on this 2DEG. We plan to perform such experiments in the near future.

CHAPTER 5

CONCLUSIONS AND PERSPECTIVES

This thesis is dedicated to the realization, investigation and exploration of nanodevices based on oxide interfaces for new quantum applications. Among the possible interfaces, we focus our attention on the LAO/ETO/STO interface, where a fully electric-field-tunable spin-polarized and 2D electron gas (2DEG) is artificially created.

Firstly, we have reviewed the oxide interfaces main properties and part of the very large literature concerning, in particular, the 2DEG at LAO/STO interface. The latter can be indeed considered as the "parent compound" of LAO/ETO/STO. Among the many possible applications of oxide 2DEG, we focused on recent results on 2DEG based nanodevices exhibiting interesting quantum effects and the proposals for devices exploiting the Rashba spin-orbit coupling in these systems, an attractive ingredient for future quantum applications.

In the second chapter we presented the LAO/ETO/STO properties, where the ETO film behaves like a δ-doping layer introducing another degree of freedom: tunable magnetic correlations (which are absent in LAO/STO). As a matter of fact, the LAO/ETO/STO samples, below a temperature of T_{FM} = 6 - 8K, become ferromagnetic, in addition to be conductive and superconductive, defining a complex

"phase diagram" [72]. We presented recent theoretical results based on density functional theory calculations which provide a detailed insight on the nature of the spin-polarized 2DEG. From these calculations, it is possible to conclude that the magnetic coupling is induced thanks to a ferromagnetic interaction between Eu and Ti states. This exchange is promoted when the Fermi level of the system is tuned to include Ti $3d_{xz,yz}$ orbitals into the transport. The theoretical observations are confirmed and strengthened by experimental results obtained using several techniques. X-ray magnetic circular dichoism analysis, in agreement with SQUID measurements, confirm the ferromagnetic coupling at the interface, extending also into the first layers of STO. Long range coupling is demonstrated by the appearance of a curvature in the Resistance vs. temperature data and by the presence of an Anomalous component in the Hall effect. Numerical calculations demonstrate that the AHE exhibited by LAO/ETO/STO 2DEG is of the intrisic type, therefore it is not due to magnetic impurities. Finally, we show a study of the interaction between Rashba spin orbit coupling and ferromagnetism, testified by the reduction of weak anti-localization effects in magnetoconductance measurements.

In the third chapter we presented a novel fabrication technique which allows to realize nanodevices where all the mentioned properties can be exploited for the realization of new functionalities. The "top down" procedure we set up during this work involves a (photo or electron beam) lithography step followed by a low temperature ion milling process. The advantages of our nanofabrication procedure lie in its applicability to every kind of oxide interfaces and also to pre-tested heterostructure, improving the yield of the procedure. Moreover, it allows to expose the lateral side of 2DEG therefore paving the way to the realization of hybrid devices. Lastly, we illustrated our preliminary results for structuring the oxide devices using He-FIB.

Finally, in chapter 4, we collected our most recent results on the tuning of the LAO/ETO/STO ferromagnetic transition by visible light. The Hall data and the spin orbit coupling analysis show that the light can manipulate the FM phase, the weak localization /antilocalization (WL/WAL) transition and enhance the ferromagnetic effects. In an effort to investigate the oxide interfaces as opto-electronic devices for

sensing and telecommunication application, we presented also preliminary results of infrared resistance response of LAO/STO interface. The presented observations provide strong motivation to further investigate this new perspective.

We conclude this work with some final comments on future applications of LAO/ETO/STO 2DEG devices.

5.1 2D-oxide devices for spin current control

In Chapter 1 (paragraph 1.4) we introduced some experiments where the spin-orbit coupling at oxide interfaces was exploited for demonstrating the possibility to obtain spin transport and manipulation in these systems. Now we will analyze the potential the LAO/ETO/STO 2DEG has in this field.
In order to efficiently inject a spin-polarized current into a conductor, an appropriate choice of materials and architectures must be made. Three possible approaches can be considered: one relies on the use of a ferromagnetic injector; another consists of inserting a ferromagnetic tunnel barrier between the injector and the channel; a third is based on spin-filtering tunnel barriers where the injecting electrode is a non-magnetic metal [139, 140]. Although all these three approaches have been demonstrated to be possible with oxides, such as in magnetic tunnel junctions [141], spin pumping (as ferromagnetic magnetic resonance (FMR))[142, 143], and spin-torque FMR [144] experiments, they pose considerable difficulties from the material science point of view and a general increased complexity in the fabrication procedure of the devices. For instance, the tunnel barrier could have high resistance, preventing an efficient spin injection into the electron gas at the interface and generating spurious spin transport signals, due to the spin-dependent hopping through defects at the contacts [145]. A fourth possible method has therefore been explored: the use of the spin Hall effect to generate pure spin currents without the need of additional ferromagnetic layer [61, 145]. Once the spin-current is generated, four-contact measurement for non-local spin detection in lateral spin valves must follow. To detect a finite spin signal, the dwell time of the spin-polarized electrons between the injection and detection contacts must be shorter than the spin lifetime, i.e. the distance between these two contacts must be shorter than the spin diffusion

length, so that the spin carriers maintain their polarization up to the next vertical line. At the same time the detection contacts must not be destructive, to enable the extraction of the spin-polarized electrons. This imposes strict conditions on both the channel material and the interface between the channel and the detection contact.

The possible existence of a local magnetic field within the 2DEG, as in the case of LAO/ETO/STO, could represent an intriguing solution. Similarly to a spin injection device, where the polarized electrons are injected from a ferromagnetic electrode into a channel by passing a current from the FM into the channel through a tunnel contact, we could use gate tunable spin-polarized 2DEG at LAO/ETO/STO interface to induce an imbalance of spin population at the channel side (spin accumulation) and create a finite additional voltage. In this thesis work, we demonstrated the possibility to fabricate nanodevices in a multiple H-bar design. These kind of devices will be used to study the dependence of the spin diffusion as a function of the channel length.

The presence of anomalous Hall effect (AHE) could be another advantage in our LAO/ETO/STO nanodevices. The anomalous Hall effect in ferromagnetic materials has attracted attention as an alternative mechanism for generating spin current. In this case, when a charge current flows in the longitudinal direction, spin-up and spin-down electrons are deflected to opposite transverse directions. Due to the asymmetry in density of states at the Fermi level and charge transport in FM, both transverse charge and spin accumulations will occur at boundaries of the sample at steady state [146].

This observed behavior of the enhanced directional response in a channel for non-reciprocal charge transport promises outstanding performances for oxide 2DEG devices which can be view as a promising platform to explore coupled charge and spin transport phenomena and to discover new effects in the field of spin-transport and spin-orbitronics.

5.2 Final considerations on the use of 2D-oxide devices for quantum spin control

The realization of a "fault tolerant" quantum computation is another of the fundamental challenges in quantum technology. The main obstacles on its path are the extreme fragility of quantum effects with respect to noise and decoherence. Quantum control, quantum initialization, read-out and enhanced coherence remain the main challenges which need to be addressed in a scalable multi-qubit platform. In the last few years, the spin-degrees of freedom, which can be manipulated with electric fields through the SOC effect, emerged as one of the possible solutions.
Oxide 2DEG systems show a sizable and fully controllable SOC; they allow a top-down approach for realization of complex nanodevices, which can be easily scaled to include a large number of qubits. The realization of quantum dots in oxide 2DEGs, for the control of individual electron spins, has been demonstrated [54]. Moreover, all the ingredients necessary for manipulating and controlling the exchange interactions and qubits operations can be realized using the same material and incorporated in the device layout in a seamless way. Therefore, oxide 2DEGs appear as optimal candiates to implement quantum spin control.
However, the feasibility of this proposal is linked to a favorable estimation of the decoherence times. In general, for a quantum variable there are three time scales to consider:
- The decay time T_1 of the quantum state from the $|1\rangle$ (excited state) to $|0\rangle$ (ground state);
- The homogeneous dephasing time T_2 that quantifies the decay of quantum mechanical superpositions;
- The inhomogeneous dephasing time T_2^*, for instance due to inhomogeneity of the magnetic field.

In the case of oxide 2DEGs, the decay time of the quantum state, T_1 is governed by electric field fluctuations and phonon induced relaxation. It can be estimated from the Zeeman and the orbital level splitting (50 meV in LAO/STO[11]) and goes from tens up to hundreds of milliseconds at 2 Tesla. The decoherence time T_2, which quantifies the decay of quantum mechanical superpositions, and the dephasing time T_2^*, are mainly governed by the SOC and hyperfine interaction HFI

(interaction of a single electron spin with many nuclear spins). In order to reduce the decay effect due to SOC, quantum dots with sizes comparable to the spin orbit length (of the order of 10 nm) could be realized. Thus, the most important source of decoherence remains the statistically fluctuating nuclear magnetic field due to the HFI, known as the Overhauser field. This latter is composed by the ensemble of nuclear spins acting as an additional magnetic field to the the external one. Root mean square of Overhauser field B_N value for an electron spin interacting with N nuclear spins is

$$B_{N,rms} = \frac{B_{N,max}}{\sqrt{N}} * \sqrt{1-x} \tag{5.1}$$

where N is total number of atoms, $B_{N,max}$ is the magnitude of magnetic field, maximal when all nuclear spins are fully polarized, and x is the fraction of nuclei with zero nuclear spin. In state of art GaAs and InAs spin-orbit qubits, $B_{N,rms}$ defines a dephasing time T_2^* typically of the order of 1-10 ns. It is important to notice that all isotopes of Ga, As and In have a finite nuclear spin ($x = 0$), while for the STO case, x is of the order of ~ 0.9. This results in a $B_{N,rms}$ in STO-based interface that is more than 2-3 times lower than in GaAs and InAs. Finally, considering that oxide 2DEG electron wavefunction retains the 3d-orbital character of the Ti-3d states, characterized by nodes at the nuclei position, we expect even further enhancement of the decoherence time, facilitating future large-scaled on-chip realizations. Thus, we argue that STO and other 2D oxides provide a promising, unexplored platform for long-lived quantum coherence of qubits.

APPENDIX A

In this section we collect the details of the experimental techniques used to realize the LAO/ETO/STO nanodevices described in this thesis work.

A.1 Realization of LAO/ETO/STO 2DEG samples

The samples described in this thesis work were realized in the MODA system (Modular Facility for Oxide Deposition and Analysis) located in the CNR-SPIN laboratories in Naples. This system includes a pulsed laser deposition chamber and several in-situ analysis techniques.

Pulsed Laser Deposition Pulsed laser deposition (PLD) is an epitaxial growing technique, widely used for the fabrication of thin films from multi-component materials and of multi-layer heterostructures. A laser irradiates a target of the desired material with fast consecutive pulses, generating a strong electric field on the target surface to extract a plasma (plume). The plume expands in a direction perpendicular to the target surface and deposits on a suitable substrate. The substrate is placed on a heater, in order to increases the mobility of the impinging atoms allowing them to diffuse over the whole substrate and giving rise to a layer by layer crystalline growth. For the growth of the LAO/ETO/STO samples described

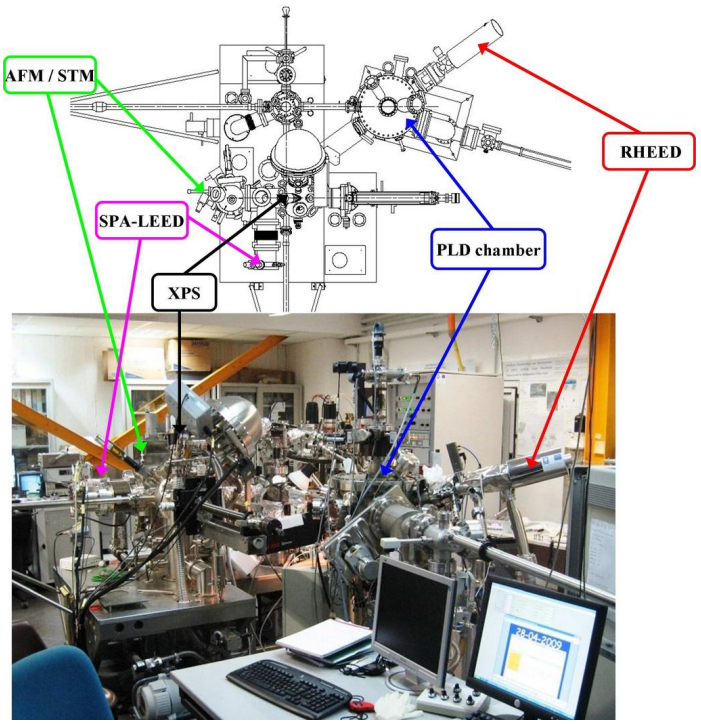

Figure A.1: The deposition system used for the growth of LAO/ETO/STO interfaces

in this thesis, we used a high-energy excimer laser (KrF) with a wavelength of 248 nm, a laser fluency of 1.3 J/cm^{-2} and a repetition rate of 1Hz. Firstly, the laser is focused on a sintered $Eu_2Ti_2O_7$ target for the growth of the $EuTiO_3$ layer, then on a crystalline $LaAlO_3$ target for the growth of the LAO layer. The TiO_2-terminated STO substrates are kept at 680 °C during both the deposition steps. During the films growth, the PLD chamber is filled with an oxygen partial pressure of $1x10^{-4}$mbar. No annealing procedures were carried out after the deposition, to avoid recrystallization of ETO in the $Eu_2Ti_2O_7$ competing phase at higher oxygen pressures. The samples were, instead, slowly cooled down to room temperature, at a rate of 3 ° C/min, in the same oxygen atmosphere used during the deposition.

Reflection High Energy Electron Difraction The growth of the thin films is monitored in situ and in real time using Reflection High Energy Electron Diffraction (RHEED). Fig. A.2 shows typical RHEED data obtained during the growth. On the left, we report the images of the RHEED pattern measured on the STO surface before deposition (top), after the deposition of the ETO layer (middle) and

after the deposition of the LAO layer (bottom). On the right, the intensity of some diffraction peaks are plot. The periodic oscillations in this plot are related to the relative surface coverage: each intensity peak represents the completion of an atomic layer. Therefore, the number of intensity peaks indicate the thickness of the thin film deposited. The first set of oscillations are related to the growth of 2 u.c. of ETO, whereas the second set of oscillations are related to the growth of LAO. As reported in chapter 2, at least 4 u.c. of LAO are required to form the 2DEG at the STO-based interface; however, in order to avoid non-homogeneity in the 2DEG due to local variations in the film thickness along the sample area, a standard thickness of 10u.c. of LAO was used in our samples.

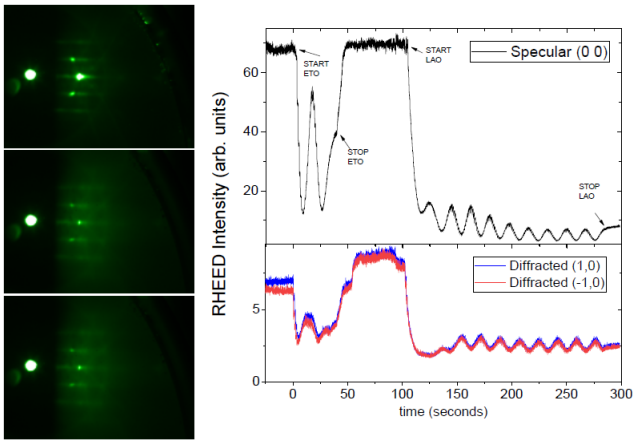

Figure A.2: Typical RHEED data obtained during the growth of a LAO/ETO/STO sample. On the left, we report the images of the RHEED pattern on the STO (top), ETO (middle) and LAO (bottom) surfaces. On the right, we plot the intensity of the diffraction peaks.

A.2 Patterning techniques

Realization of a resist mask The first step to pattern the 2DEG at the oxides interface is to create a resist mask to cover areas we want to be protected during the subsequent ion milling. Firstly, the resist is deposited by spin coating on the sample. Then, it is shaped using photo or e-beam lithography.
During this thesis work, photolithography was performed in the Photolitography laboratories of the Department of Physics, at the University of Naples Federico II, using a Karl-Suss MJB3 mask aligner and Shipley S1813 photoresist (800 nm

thick). By using a 350 nm lamp for irradiation, this machine allows a resolution of 2 μm.
For devices with higher resolution, we resorted instead to electron beam lithography (EBL). In this case, a beam of electrons, instead of UV light, is used to transfer the desired pattern on the resist. During this work EBL was performed thanks to a collaboration with the Chalmers University of Technology using a JEOL JBX-9300FS. The EBL procedure set up for our samples is non-standard for several aspects.
First of all, EBL is performed on LAO/ETO/STO samples which, as deposited, have a resistance at room temperature between 5 and 10 kOhm, orders of magnitude higher than a metallic film. Moreover, the conducting layer is buried under several nanometers of insulating material (LAO and ETO). Therefore, in order to reduce charge buildup during electron beam scanning of the sample and deflection of the electron beam, very low exposure currents have been used. Lower exposure current translates into higher exposure times. In order to expose both the nanoscale parts and the larger areas of the devices (ex. contact pads) during the same EBL run, the latter was divided into two parts: during the first, the nanochannels were exposed using a current in the hundreds of nA range. Then, the current was increased to the μA and the exposure of the larger areas was carried out. In this double exposure procedure, great care has to be taken to link the two areas, in order to avoid stitching problems for the masks due to the deflection of the electron beam mentioned above.
A second issue regards the use of EBL resist as hard mask. EBL resist is indeed a "soft" material used for lift-off processes or covered with an hard mask when ion milling is required. Due to the characteristics of our oxide materials, we could not use either of the options above, therefore we have to resort to a simple increase of the resist layer thickness to make it more robust. We performed several tests changing the resist type and thickness to assess the robustness in our ion milling conditions. The best results were obtained using a ma-N2403 electron beam resist from Micro Resist Technology GmbH, with a thickness of 200 nm.

Low-temperature ion milling Once the resist mask is created thanks to optical or e-beam lithography, we use low temperature Ar+ irradiation to define the

structures in the 2DEG at the oxide interfaces by removing the LAO/ETO areas not protected by the resist.
We use a beam current of 8 mA and a beam voltage 400 V for a 3 cm beam aperture. These parameters result in a stable etching rate of 2 nm/min for the oxide layers. The LAO/ETO/STO samples used in this work are composed of 2 u.c. of ETO and 10u.c. of LAO, resulting in total thickness of 4.7 nm. In order to ensure the complete removal of the LAO/ETO bilayer, however, we decided to perform a slight over-etch of the STO substrate. The total ion milling duration for our sample is therefore of 3 minutes, which leads to the removal of the complete LAO/ETO bilayer plus a few nanometers (1 or 2) of the STO substrate. In the same beam conditions, the etching rate of the resist is around 20 nm/min, therefore ensuring optimal protection of the pattern also for in the softer e-beam resist case (200 nm thick).
The impact with energetic Ar+ ions during ion milling causes a temperature increase of the processed samples, which in our case could turn in enhanced loss of oxygen. During this work, the heating of the samples under ion milling has been limited by gluing them on a copper cold finger where nitrogen gas, cooled down using liquid nitrogen, circulates. The temperature of the cold finger is constantly monitored using a thermo-couple. The efficiency of this system is such that the sample stage reaches temperatures down to -150 ° C. Furthermore, the ion milling process was carried out alternating milling runs with pauses to allow the cooling of the samples.
Cooling down of the samples during ion milling turned out to be of fundamental importance to ensure that the STO substrate keeps its insulating properties. Ion milling is a widely used technique not only for the realization of small scale devices, but also in the field of imaging, for the preparation of transmission electron microscopy (TEM) samples. In the latter case, great attention and study has been dedicated to potential damages induced by ion bombardment in the specimen structure, as they can severely alter the results of TEM analysis. One of the sources of ion damage is heating, which, among other effects, can promote thermal activated mechanisms and oxygen desorption [147]. Cooling the sample stage with liquid nitrogen has therefore been introduced since many years in the TEM scientific community (indeed, ion milling systems equipped with a liquid nitrogen cooling stage are now commercially available).

In Fig. A.3 we show the AFM image of a LAO/ETO/STO nanodevice realized using the same ion milling parameters described above but without liquid nitrogen cooling of the sample stage. On the STO etched surface, terraces can easily be distinguished (see black dashed lines as guide to the eyes). However, by wire bonding directly on the exposed STO area, we found that the STO areas are conducting with a resistance in the range of hundreds of kOhm, resulting in electrical contact among the devices. Electrical conduction of the STO etched areas disappear if the sample is cooled during the ion milling.

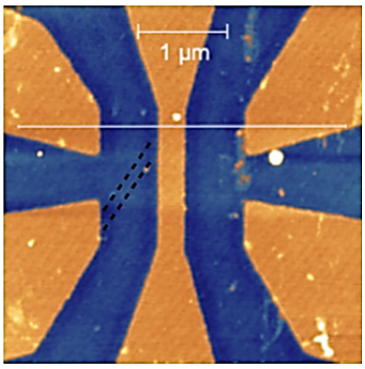

Figure A.3: AFM image of a LAO/ETO/STO nanodevice realized with e-beam lithography and room temperature ion milling. Although the nanostructures are well defined and terraces in the STO substrate are well visible, the latter is found to be conducting, as the result of oxygen desorption.

APPENDIX B

APPENDIX B

B.1 Structural characterization techniques

Atomic force microscopy The Atomic Force Microscopy (AFM) is a scanning probe microscopy mode which uses a physical probe to scan and investigate the surface of a sample at high resolution. Local material properties such as friction, height and magnetism can be also measured with such technique, depending on the probe.
In this work, we used a Park AFM 100 instrument in contact mode (force 15 nN, tip nanosensor NC36 model). The samples were tested multiple times during the nanodevices fabrication process. Firstly, the surface of the as-received STO substrates is inspected to assess their quality. Defects in the STO crystal are indeed the first cause of disomogeneity in oxide 2DEG devices. During the patterning process, the samples were also inspected before and after the ion milling. We point out that, as the ion milling can be done in several steps, in some cases the devices were inspected also in between one ion milling run and the other.

Lateral Force Microscopy The lateral force microscopy technique can provide useful information about the different terminations on the same material as

demonstrated in the case of oxides and specifically in the case of STO [148]. As common for most setups, in our AFM, the tip is scanned with constant force load (L), which results in a lateral friction force acting on the tip and hence a torsion (T) force acting on the cantilever. The torsion force applies a torsion moment to the cantilever, creating an angular deflection (or twist) of the cantilever. We use an optical lever method to detect the deflection of the cantilever, whereby a laser is reflected off the back of the cantilever onto a position sensitive photodetector (PSD) with four quadrants. The twist of the cantilever results in a lateral movement of the laser spot on the PSD which is measured as a change in the lateral voltage output from the PSD, which is the quantity we show in Fig. 3.5 (Chapter 3). The friction coefficient (μ), which can be in principle determined from the torsion using the following formula: T = μ(L+A) (where A is the adhesion force) is sensitive to the surface termination. In Fig. 3.5 (b) and (e) the lateral force signal is extremely uniform along the etched substrate terraces and between the terraces, suggesting single atomic termination and no ion milling induced defects.

Scanning SQUID Microscopy The Scanning SQUID microscopy images shown in Chapter 3 were realized on LAO/ETO/STO patterned samples at the Bar-Ilan University by the group of prof. Beena Kalisky [115]. Measurements were performed using a SQUID with loop of 3 μm at T = 4K.
A Superconducting Quantum Interference Device (SQUID) is a sensitive magnetometer that uses quantum phenomena to detect magnetic flux. Utilizing scanning SQUID magnetometer, it is therefore possible to investigate local deviation of electronic properties and simultaneously map electronic and magnetic properties of oxide interfaces [121]. The SQUID pickup loop captures the magnetic field lines generated by the current driven through the sample, as a function of location. The data obtained are the convolution of the magnetic field of sample with the spread function depending of the position of the SQUID pickup loop. The deconvolution analysis separates out the contribution of the field from that of the pickup loop, leaving behind only the measured magnetic field of the sample.
The scanning SQUID microscope (SSM) was used in this thesis with two main goals: 1. detect the presence of current carrying paths in the etched areas of STO and 2. check for the presence of ion milling induced defects. As regards the first

point, if a current carrying line is present, it would clearly show as magnetic field lines captured by the SQUID pickup loop. As regards, the presence of defects, regions with reduced or enhanced conductivity distort the flow of current and therefore the distribution of magnetic field lines [120]. These show up in SSM images as localized regions, sometimes resolution limited, or elongated features. Some defects can be seen in the LAO/ETO/STO areas of image 3.6 c).

B.2 Electrical transport characterization

After patterning, the transport properties of devices have been analyzed by connecting the 2DEG devices with ultrasound wire bonding (performed with a K&S 4523 Manual Wire Wedge Bonder machine) to a sample holder.
As explained in chapters 3 and 4, the transport properties of the nanodevices have been studied with varying temperature, electrostatic and light doping and as a function of the magnetic field. Several cryogenic set-ups were therefore used.

Transport measurement down to 4K The transport measurements as a function of the temperature, of the gate voltage and of the visible light down to 4K were carried out using a variable temperature cryostat at the University of Naples. The bias current was provided by Keithley 6220 picoammeter and the sample response was measured using a Keithley 2182 nanovoltmeter. The gate voltage was supplied using a Keithley 2400 sourcemeter.
The measurements in magnetic field were performed in part at the University of Naples, using a Oxford Instruments-MagLab magnetometer, and in part at the Laboratoire Charles Coulomb, at the University of Montpellier, France, using a superconducting magnet able to generate a field up to 12 T.

Transport measurements down to 0.3K Measurements down to 0.3K were performed in the Heliox ^{3}He cryostat (Oxford Instruments). In this type of cryostat, the cryogenic insert is immersed in a helium bath and liquid helium is introduced into a 1K pot thanks to a capillary. A rotary pump allows to lower the 1K pot temperature down to $\sim$ 1.8K, starting the condensation of a ^{3}He and ^{4}He mixture. From this mixture, the more energetic atoms are pumped away thanks to a sorbp-

tion pump, and a final temperature of 0.3K can be reached. The system at the University of Naples is equipped with two different filtering stages at different temperatures: low pass RC-circuits, known as π-filters, with a cut-off of about 1MHz installed at the 1K-Pot stage; and two copper powder filtering stages with typical cut-off frequencies of about 1 GHz mounted at the 1K-pot stage and at the 0.3K stage in order to attenuate thermal and electronic noise.

Transport measurements down to 7mK The cryostat used for these measurements is a Triton XL model (Oxford Instruments) installed at the University of Naples. In this type of cryostat (called Cryogen-free) the liquid helium bath is replaced by a dry system. This is able to reach the base temperature of < 10 mK. Also this system is filtered against electrical noise. The filters are different for the different temperature stages; they are divided into EMI filters, that reduce the high frequencies at room temperature; low-pass RC filters that remove the frequencies above ~ 100 kHz at about 1K; copper powder filters connected to the cryostat coldest plate that delete the frequency of ~ GHz.

Transport measurements under IR irradiation The laser irradiation experiments shown in paragraph 4.3 were performed using a cryogenic laser system at CNR-SPIN laboratories of Pozzuoli (Naples). The system is entirely mounted on an anti-vibration optical bench and is composed of a continuous flow helium cryostat where the device is kept at a controlled temperature. On optical window allows for illumination of the samples area using various laser sources (850 nm - 1550 nm) with a beam focused in 0.01 mm diameter spots. It is possible to control the intensity, polarization and position of the laser beam on an area of 10x10mm^2 with an accuracy of 10μm. The presence of a video camera coaxial with the laser beam allows to view the irradiated surface with high resolution and check their alignment. During the measurements, the devices are current biased using a battery operated voltage source connected to a variable resistor (0 - 100 kOhm).

APPENDIX C

APPENDIX C

C.1 Simulation techniques

In this section we briefly describe the computational techniques used in this thesis work.

Finite elements simulations of the electrical transport During this thesis work, we extensively used finite elements simulation of the nanodevices response to both design efficient field effect geometries and verify the quality of the devices. The software employed is COMSOL Multiphysics software. It is a cross-platform finite element analysis, solver and multiphysics simulation software. It allows conventional physics-based user interfaces and coupled systems of partial differential equations. We used this tool to, firstly, design the geometry of our devices. In particular, in the case of multiple side gate field effect devices the software was essential to determine the size of the side electrodes and their dimension in order to obtain an uniform doping of the central nanochannels. Fig. C.1 shows simulations of 2S devices with varying distance between the lateral electrodes. The simulations were performed assuming, for the low-temperature STO dielectric

constant ϵ, the electric field E dependence:

$$\epsilon(E) = 1 + \frac{B}{[1 + (E/E_0)^2]^{1/3}} \tag{C.1}$$

with B=25462 and E_0=82213 V/m. The effect of changes in the distance between the side gates can be immediately appreciated in the distribution of the electric field inside the nanochannel. These considerations lead, for example, to a design of the tilted side gate electrodes which can be seen in Fig. 3.4 b) and c).
Another important use of the simulation software was for the determination of the shape factor of our geometries. In order to compare the properties of devices with different size and geometry, the sheet resistance value can be used as it is indeed directly related to the carrier concentration. In a regular three-dimensional conductor the resistance is related to the resistivity ρ , the cross-sectional area A, the length L, the width W and the thickness t:

$$R = \rho \frac{L}{A} = \rho \frac{L}{Wt} = R_{sheet} \frac{L}{W} \tag{C.2}$$

The sheet resistance R_{sheet} can be considered as the resistivity per unit thickness, defined through a purely geometric factor from the measured resistance R. Since the ratio L/W is dimensionless, the sheet resistance is conventionally expressed in Ω per square or $\Omega/\square$, to avoid confusion with normal resistance.
We can rewrite the general relation written above as:

$$R_{sheet} = R * f \tag{C.3}$$

where f is a form factor depending only on the planar geometry of the examined sample, while R_{sheet} depends only on the sample's resistivity and thickness along the z axis. For simple geometries (square, rectangle) f is easily obtained using the width and the length of the sample. Our devices, however, have irregular geometries, including hundreds of micron large areas (ex. contact pards) and sub-micron central channels. Therefore we perform finite element simulations using COMSOL Multiphysics to obtain an accurate estimation of f. Firstly, we impose a standard value for R^*_{sheet} = 500 $\Omega/\square$, that represents typical value for good quality LAO/ETO/STO samples. Then we run the simulation of the electrical transport in our devices (using the same bias current of the actual experiment) and from that

we extract the resistance R_{sim} a standard sample (with R_{sheet} = 500 Ω/□) should exhibit. The following relation will hold:

$$f = \frac{R^*_{sheet}}{R_{sim}} \tag{C.4}$$

which allows us to obtain the form factor to calculate the R_{sheet} of the measured samples.

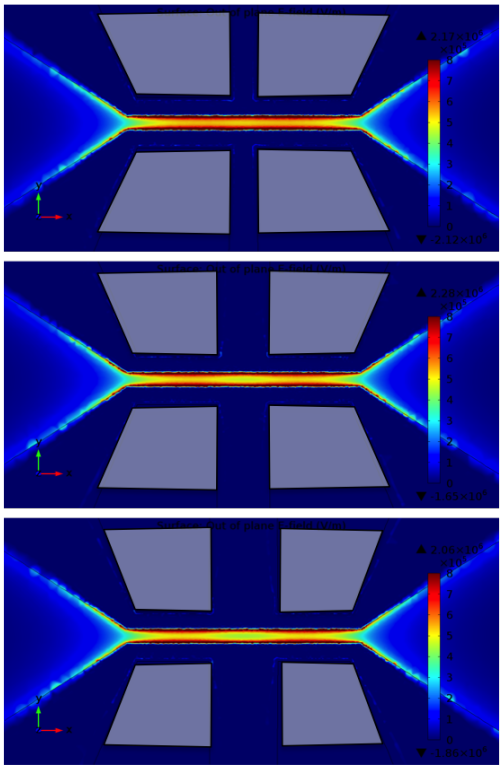

Figure C.1: Finite elements simulations run with COMSOL multiphysics depicting the electric field effect in a 2S device (w=0.35μm, L=4μm) for increasing distance between the side gate electrodes: 0.5μm (top), 1μm(middle) and 1.2μm (bottom). The color scale indicates the out-of-plane electric field E_z generated in the channel applying 0.2V to both pairs of side gate electrodes. A clear disuniformity in E_z develops increasing the separation between the gate electrodes.

Fit of the magnetoconductance data The theoretical models most widely used to fit the magnetoconductance data of system showing spin-orbit coupling (SOC) were developed by Hikami, Larkin, and Nagaoka (HLN) and by Iordanskii, Lyanda-Geller, and Pikus (ILP). The former is based on the Elliott-Yafet spin-flip scattering mechanism and incorporates only the k-cubic SO coupling term, whereas

the latter is based on the Dyakonov-Perel spin precession mechanism and takes into account both the k-linear and k-cubic SO coupling (where k is the wave vector of the carrier) (see also paragraphs 1.2.2 and 2.7) . For oxide 2DEGs, it has been demonstrated that the k-linear term is predominant, therefore, the Maekawa and Fukuyama (MF) formula, a development of the HLN theory, has been often used with good results. This success is due to the mathematical identity of the models when only the k-cubic term is taken into account.
We have used the MF theory to fit the experimental data of magnetoconductance (MC) curves as a function of gate voltage for LAO/ETO/STO samples under visible lights. The MF formula describes the evolution of the conductance of a 2D system as a function of the magnetic field in the presence of weak (anti-) localization WL (WAL) and including a spin-orbit term.
The MF quantum correction of the magnetocondutivity under a perpendicular magnetic field B can be expressed as:

$$\frac{\Delta\sigma}{\sigma_0} = \Psi\left(\frac{B}{B_i + B_{so}}\right) + \frac{1}{2\sqrt{1-\gamma^2}}\left(\frac{B}{B_i + B_{so}(1+\sqrt{1-\gamma^2})}\right) + \\ -\frac{1}{2\sqrt{1-\gamma^2}}\left(\frac{B}{B_i + B_{so}(1-\sqrt{1-\gamma^2})}\right)$$

where the function Ψ is $\Psi(x) = ln(x) + \Psi(1/2 + 1/x)$ and Ψ is the digamma function. This equation contains three fitting parameters B_i, B_{so}, and γ from which we can obtain the inelastic scattering time τ_i, the spin relaxation time τ_{so} and the g factor of electrons using the following relations:

$$B_i = \frac{\hbar}{4eD\tau_i}$$
$$B_{so} = \frac{\hbar}{4eD\tau_{so}}$$
$$\gamma = \frac{g\mu_B B}{4eDB_{so}}$$

where μ_B is the Bohr magneton and D is the diffusion coefficient.

APPENDIX D

D.1 Attached papers

M. D'Antuono, A. Kalaboukhov, R. Caruso, S. Wissberg, S. Weitz Sobelman, B. Kalisky, G. Ausanio, M. Salluzzo and D. Stornaiuolo
Nanopatterning of oxide 2-dimensional electron systems using low-temperature ion milling
Nanotechnology 33 (2022) 085301 (7pp)

R. Di Capua, M. Verma, M. Radovic, V.N. Strocov, C. Piamonteze, E. B. Guedes, N.Plumb, Yu Chen, M. D'Antuono, G.M. De Luca, E. Di Gennaro, D. Stornaiuolo, D. Preziosi, B. Jouault, F. Miletto Granozio, A. Sambri, R. Pentcheva, G.Ghiringhelli and M. Salluzzo
Orbital selective switching of ferromagnetism in an oxide quasi two-dimensional electron gas
arXiv:2109.06138v1
Submitted to npj Quantum Materials

Nanopatterning of oxide 2-dimensional electron systems using low-temperature ion milling

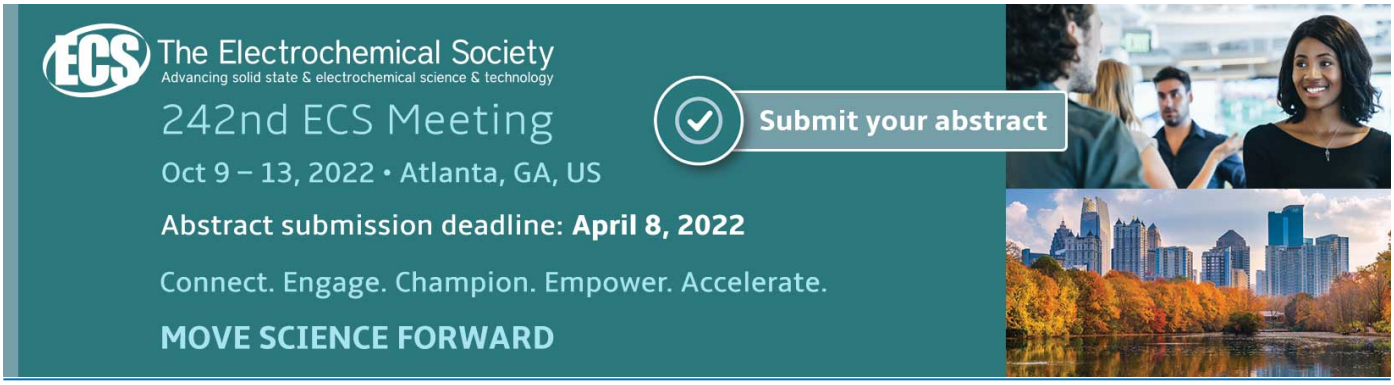

OPEN ACCESS
IOP Publishing
Nanotechnology

Nanotechnology **33** (2022) 085301 (7pp)
https://doi.org/10.1088/1361-6528/ac385e

Nanopatterning of oxide 2-dimensional electron systems using low-temperature ion milling

M D'Antuono[1,2], A Kalaboukhov[3], R Caruso[1,2,4], S Wissberg[5], S Weitz Sobelman[5], B Kalisky[5], G Ausanio[1,2], M Salluzzo[2] and D Stornaiuolo[1,2]

[1] University of Naples Federico II, Italy
[2] CNR-SPIN, Naples, Italy
[3] Department of Microtechnology and Nanoscience MC2, Chalmers University of Technology, Gothenburg, Sweden
[4] Brookhaven National Laboratory, Condensed Matter Physics and Materials Science Department, Bldg. 480, PO Box 5000 Upton, NY 11973-5000, United States of America
[5] Department of Physics and Institute of Nanotechnology and Advanced Materials, Bar-Ilan University Ramat-Gan, Israel

E-mail: maria.dantuono@unina.it

Received 28 May 2021, revised 4 November 2021
Accepted for publication 9 November 2021
Published 30 November 2021

Abstract

We present a 'top-down' patterning technique based on ion milling performed at low-temperature, for the realization of oxide two-dimensional electron system devices with dimensions down to 160 nm. Using electrical transport and scanning Superconducting QUantum Interference Device measurements we demonstrate that the low-temperature ion milling process does not damage the 2DES properties nor creates oxygen vacancies-related conducting paths in the STO substrate. As opposed to other procedures used to realize oxide 2DES devices, the one we propose gives lateral access to the 2DES along the in-plane directions, finally opening the way to coupling with other materials, including superconductors.

Keywords: oxide 2DES, nanodevices, oxide field effect devices

(Some figures may appear in colour only in the online journal)

1. Introduction

The wealth of properties shown by transition metal oxide materials has stimulated in the latest years an intense research into oxide heterostructures, where such properties can be modulated via structural, chemical or electronic coupling [1]. Interfaces between different complex oxides, in particular, give rise to extraordinary and unexpected phenomena. At the $LaAlO_3/SrTiO_3$ (LAO/STO) interface, for example, a superconducting, highly tunable two-dimensional electron system (2DES) develops [2]. This system can also be engineered to obtain even more intriguing multi-functional heterostructures. Introducing a magnetic $EuTiO_3$ layer between LAO and STO, for instance, a spin-polarized, superconducting oxide 2DES can be realized [3, 4]. Using Ca-doped STO substrates ferroelectricity can be added to the rich phase diagram of LAO/STO [5, 6]. The relevance of oxide 2DES for possible electronic applications is also emerging [7–9]. Experiments show that oxide 2DES can be used to perform spin-to-charge conversion with high efficiency [10], are suitable for transistor [11, 12], photonic and high frequency applications [13, 14]. These are some of the reasons for the recent interest in the realization of oxide based nanodevices, which could give the unique opportunity of investigating the physics of a 2D system in detail and

studying the interaction among several, in some cases antithetical, electronic phases.

In the latest years, several techniques have been used to realize nanodevices based on novel materials for advanced electronic applications, from ultra-high resolution electron beam lithography to direct writing using electron beams [15]. Specific device fabrication techniques were also developed soon after the discovery of the LAO/STO system. Scanning a voltage-biased metallic tip of an atomic force microscope (AFM) over the surface of a 3 unit cell (u.c.) thick LAO film enables to locally 'write' conducting channels at the interface, with a lateral resolution down to 2 nm [16–18]. A second approach is based on the realization of a pre-patterned substrate. Photo- or electron-beam lithography is used to define a resist mask reproducing the desired devices layout, which is then transferred to the STO substrate via deposition of an amorphous oxide layer and lift-off. Subsequently, the LAO film is deposited creating a conducting interface on the areas not covered by the amorphous template [19, 20]. A third patterning method is based on low-energy Ar ion beam irradiation of the LAO/STO interface [21]. The LAO/STO sample is firstly covered with a resist mask, then Ar irradiation eliminates the electrical conductivity at the interface in the exposed areas, without physical removal of the LAO film.

Thanks to the techniques described above, great progress has been made in the understanding of oxide interface physics. However, many issues are still open. The nature of the superconducting ground state in the LAO/STO system, for example, is still not completely understood. Several theoretical [22–25] and experimental [18, 26, 27] works indicate an unconventional superconducting ground state for this 2DES, but a final proof of the superconducting order parameter symmetry is still lacking. A direct way to probe the order parameter symmetry would be to couple the 2DES with a conventional superconductor, as for example has been done to study the order parameter symmetry of high temperature superconductors (HTS) [28]. In the case of oxide interfaces having intrinsic 2D nature, this coupling should take place in the in-plane directions. The nanofabrication techniques currently available, on the other hand, result in devices where the 2DES patterned channels are encapsulated in a crystalline or amorphous matrix, making it very difficult to perform such lateral electrical transport experiments.

In this work we present oxide 2DES nanodevices realized with a technique based on low-temperature ion milling, which allows to expose the sides of the nanostructures. Ion milling is commonly used for patterning of complex devices but, when applied to oxide materials, it can promote thermally activated oxygen desorption. In our case, this could lead to the formation of conducting areas in the STO substrate and electrical shorts between the devices [29]. We demonstrate that the careful tuning of the milling parameters and the cooling of the sample during the milling process (as sometimes done for the preparation of samples for transmission electron microscopy [30]) greatly limits the substrate damage. Our process results in nanodevices down to 160 nm in width. The absence of conducting paths in the substrate is clearly demonstrated by the transport properties of the devices and using scanning Superconducting QUantum Interference Device (SQUID) measurements. Moreover, the STO areas exposed after the ion-milling show very ordered terrace structures, therefore they could host the growth of complex materials laterally coupled to the oxide 2DES.

2. Methods

In this work we present the properties of devices based on $LaAlO_3/EuTiO_3/SrTiO_3$ (LAO/ETO/STO) heterostructures [4]. However, the fabrication procedure we describe is suitable also for LAO/STO and whatever type of oxide thin film and interface. The process is illustrated in panels (a)–(c) of figure 1. Initially, LAO(10 u.c)/ETO(2 u.c.) heterostructures (panel (a)) are realized by pulsed laser deposition on TiO_2-terminated (001) STO substrates. A KrF excimer laser (wavelength 248 nm, pulse rate 1 Hz) is focused on a sintered $Eu_2Ti_2O_7$ or on a crystalline LAO target at a fluency of 1.3 J cm^{-2}. During the deposition the substrate is kept at 680°C in oxygen partial pressure p_{O_2} of 1×10^{-4} mbar. The layer by layer thin films growth is monitored using reflection high-energy electron diffraction (RHEED). Following deposition, the sample is slowly cooled down to room temperature in $p_{O_2} = 1 \times 10^{-4}$ mbar [3].

After deposition of the heterostructures, a resist mask is realized using photolitography or electron beam lithography (figure 1(b)). In the latter case, we use a layer of negative tone ma-N2403 electron beam resist from Micro Resist Technology GmbH, with a thickess of 200 nm [31].

After resist development, the LAO/ETO areas not protected by the mask are etched with a low-intensity Ar ion milling process. We use a beam current of 8 mA and a beam voltage 400 V for a 3 cm beam aperture. These parameters result in a stable etching rate of 2 nm min^{-1} for the oxide layers, and the LAO/ETO areas not protected by resist are removed in 3 min of milling. The thickness of the resist mask ensures that the areas covered by the resist are well protected throughout this brief ion milling process. During the process the sample is glued on a cold finger kept at low temperature (−150 °C). This approach has been used in the past to realize nanoscale biepitaxial HTS grain boundary junctions and devices [32–34]. It was found that cooling the sample during the ion milling is crucial to ensure minimal loss of oxygen from the oxide HTS film, especially in the grain boundary areas.

After transferring the resist geometry to the oxide layers, the mask is finally washed away in an acetone bath (figure 1(c)). After fabrication, all the devices are inspected by atomic and lateral force microscopy using an AFM PARK 100 instrument in contact mode (force 15 nN, tip nanosensor NC36 model).

The transport properties of the devices were tested down to 5 K using a variable temperature cryostat. In order to compare the electrical transport properties of devices with different dimension and geometry, the sheet resistance value $R_{sheet} = R * f$ (with f a shape factor related to the device

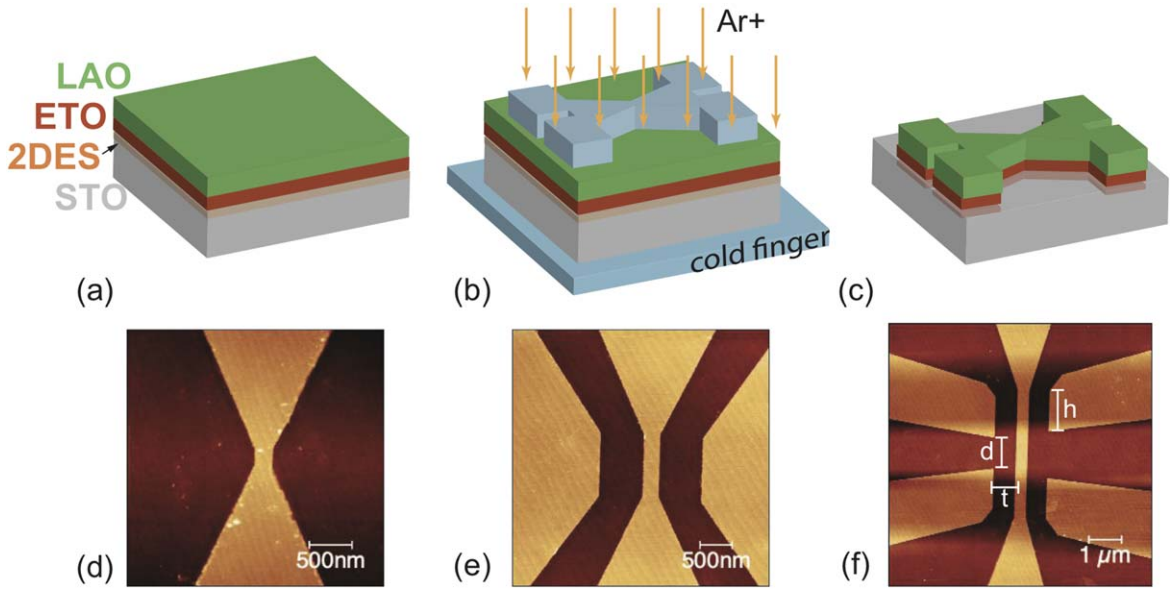

Figure 1. Sketch of devices fabrication process and contact mode AFM topography images of some of the LAO/ETO/STO devices realized. After the ETO/LAO bilayer is deposited (a), a resist mask is realized via photo or electron beam lithography and low temperature ion milling is used to remove the exposed areas of the ETO/LAO bilayer (b). Finally, the resist is washed away in an acetone bath (c). In the lower part of the figure we show the AFM images of a Dayem bridge (d), a side gate device with one pair of lateral electrodes (geometry 1S) (e) and a side gate device with two pairs of lateral electrodes (geometry 2S) (f).

geometry) can be used as a reference. In order to calculate the factor f for complex geometries, we perform finite element simulations using COMSOL MULTIPHYSICS software, as described in [12, 35]. Hall effect was tested applying a perpendicular magnetic field in a Physical Properties Measurement System (PPMS Quantum Design) and an Oxford Instruments-MagLab magnetometer. Finally, the spatial distribution of the current flow was mapped using a scanning SQUID microscope.

3. Results

Figures 1(d)–(f) show representative AFM images of devices realized using e-beam lithography: a constriction (Dayem bridge) with width $w = 200$ nm and length $L = 160$ nm (d), a side gate device with one pair of lateral electrodes (geometry 1S) with a central channel 250×1000 nm (e) and a side gate device with two pairs of lateral electrodes (geometry 2S) and a central channel 350×4000 nm (f). Well defined patterns with sharp edges are clearly visible, as well as the terraces on the LAO/ETO bilayer replicating those on the underlying substrate. In order to characterize the surface of etched devices we show in figure 2 contact mode AFM and lateral force microscopy images acquired in smaller regions of one of the Dayem bridge devices. Panel (a) shows that, remarkably, the terraces structure is preserved in the ion-milled areas of the substrate, as it can be seen also from the steps in the line profile of panels (c) and (f). The step height of each terrace is 3.9 Å (panel (f)). Panels (b) and (e) show that the lateral force signal is the same on each consecutive terrace, suggesting single atomic termination. Small inhomogeneities in the topographic and lateral force microscopy (2–5 nm wide, less than one unit cell high) on a single terrace are related to native defects present on the STO single crystal surface before the deposition (imperfect TiO_2 termination) [36] or in the LAO surface, common also to LAO/STO samples [37]. The data shown in figures 1 and 2 demonstrate that the ion milling process causes minimal structural damage to the exposed STO surfaces.

All the devices show a metallic behavior, as for example reported for a Dayem bridge in figure 3(a). In the inset we show the R_{sheet} as a function of devices dimensions. We include data from a large sample (500×500 μm) realized resorting to photolithography followed by low-temperature ion milling. Its properties are comparable to those of pristine (no patterned) heterostructures.

In [38] LAO/STO nanochannels were realized using a BCl_3-based reactive ion-etching process. The authors find that the R_{sheet} increases with decreasing width and infer a sidewall depletion of 20 ± 3 nm on each side of the structures. From the inset of figure 3(a) it can be seen that, in our case, R_{sheet} is approximately constant with the device width, and similar to that of a larger scale device (data point at $w = 500$ μm). This demonstrates that a depletion layer, if present, is very small and does not influence substantially the properties of the 2DES.

The devices realized in this work are tunable using electric field effect. Red diamonds in figure 3(a) show the R_{sheet} versus gate voltage V_g behavior for a Dayem bridge. The gate voltage V_g was applied to an electrode placed on the back of the STO substrate (back gate configuration). After a first sweep of the gate voltage to positive values (the so called 'forming' process —not shown [39–41]), the R_{sheet} versus V_g curve is perfectly reproducible. A change of more than 2 orders of magnitude in the R_{sheet} can be obtained with a change of V_g of 40 V, similar

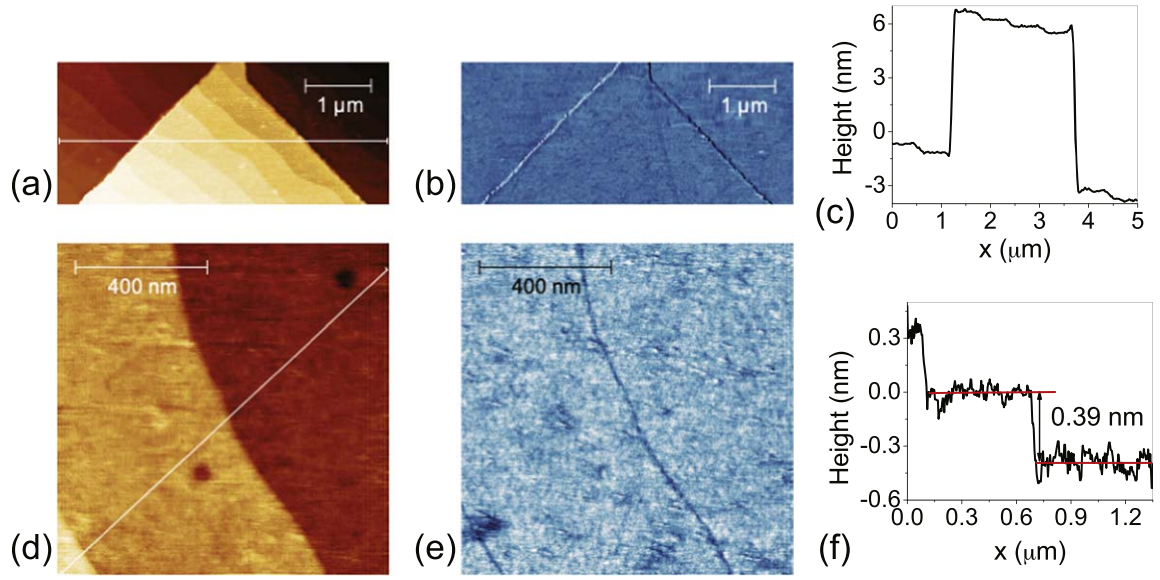

Figure 2. Upper panels: topography (a) and lateral force (b) across an etched Dayem bridge device. The images were acquired in contact mode. Panel (c) shows the profile along the white line depicted in the topography image (a). Bottom panels: topography (d) and lateral force (e) images on a small area of the ion-milled STO substrate showing two terraces with step height of one unit cell, as reported in panel (f). Lateral force shows that consecutive terraces have the same surface termination, as no contrast in the image is observed. Small changes in the lateral force signal are due to localized defects on the surface.

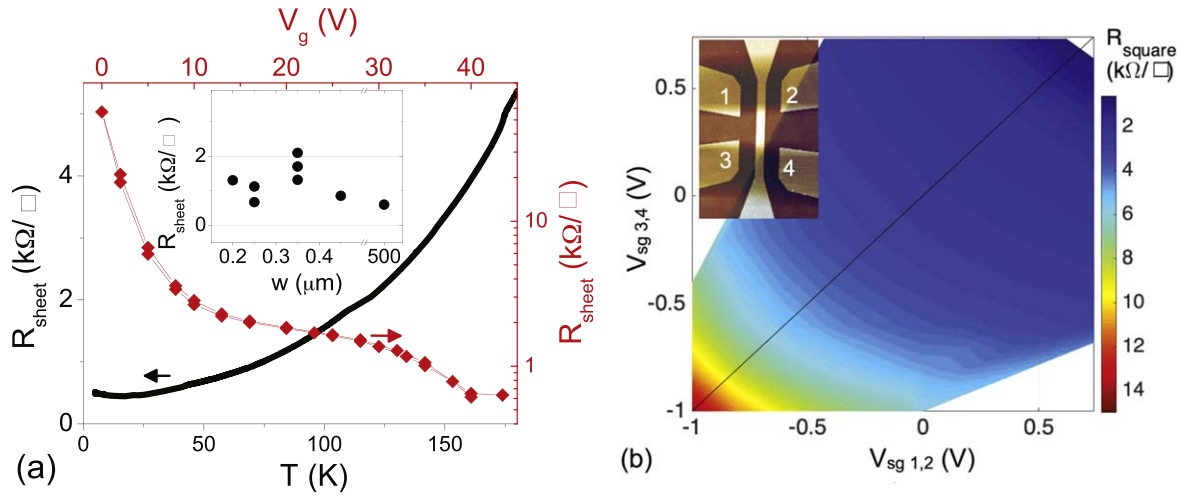

Figure 3. (a) Temperature (black data) and back gate voltage V_g (red data) dependence of R_{sheet} for a Dayem bridge with $w = 200$ nm and $L = 160$ nm. The R_{sheet} versus V_g data were obtained at 4.2 K. In the inset, we show the R_{sheet} at 4.2 K of devices of different width, ranging from 0.2 to 0.45 μm. The length of these devices ranges from 0.16 to 4 μm. We report also data from a 500 × 500 μm Hall bar device realized via photolithography and low temperature ion milling. (b) R_{sheet} of a side gate device 2S as a function of gate voltages applied independently to the two pairs of gate electrodes (see sketch in the inset) measured at 4.2 K. In black we show the $V_{g1,2} = V_{g3,4}$ line as a guide to the eye.

to that obtained for LAO/STO Dayem bridges realized with the amorphous template technique [26]. In the case of side gate devices the gate voltage can be applied also using the lateral electrodes. In figure 3(b) we show a contour map of the R_{sheet} of a device with geometry 2S (width $w = 450$ nm and length $L = 4$ μm). The width of the side gate electrodes (distance h in figure 1(e)) is 1.2 μm, their distance from the center of the channel (t) is 0.75 μm and the distance between the two side gates in the point closer to the channel (d) is 1 μm. To realize this plot, different values of gate voltages were applied independently to the two pairs of electrodes 1–2 and 3–4 (see inset in the same panel) in order to tune half of the channel length at a time. From the symmetry of the plot we can conclude that the two sections of the channel can be tuned independently and that the channel is remarkably uniform and homogeneous along its 4 μm length. During these measurements, the leakage current was stable below 2 nA, ensuring that the side electrodes are properly insulated from the central channel and that the STO substrate kept its insulating nature after the ion-milling process.

In figure 4(a) we show the carrier concentration measured on a Hall bar device (500 × 500 μm^2) realized with photolithography and low temperature ion milling. At $T = 5$ K we

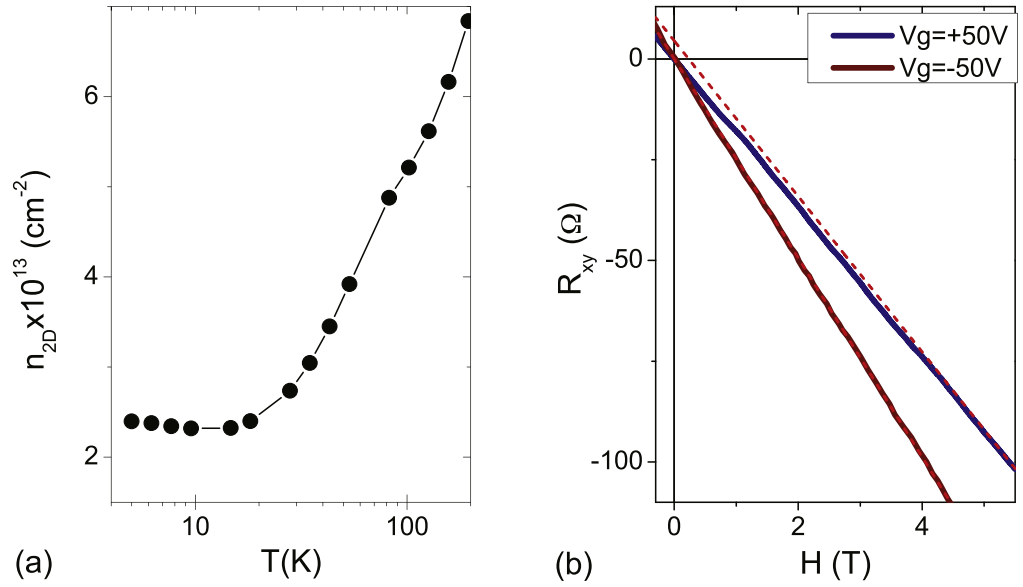

Figure 4. (a) Carrier concentration measured as a function of the temperature at $V_g = 0$. (b) Transverse resistance R_{xy} measured at $V_g = -50$ V (brown line) and $V_g = +50$ V (blue line) at $T = 5$ K in perpendicular magnetic field. The red dashed lines are fit around $H = 5$ T, highlighting the presence of a low field curvature at high gate voltage. The data in both panels were measured on large scale Hall bars realized using low temperature ion-milling.

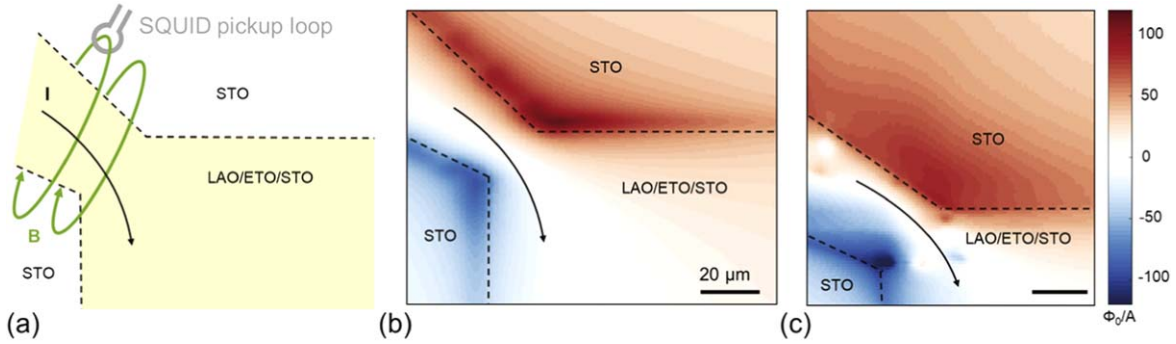

Figure 5. (a) Schematic of scanning SQUID pickup loop capturing field lines near the surface of a current carrying device. In this picture, the device area is shown in yellow color, while the substrate areas are shown in white. Dashed line marks the physical edge of the device. (b) Simulation of the magnetic flux pattern in a homogeneous conductor with the same geometry as the measured LAO/ETO/STO device. (c) Scanning SQUID data over a patterned LAO/ETO/STO device taken at 4 K. Dipole-shaped distortions to the image indicate regions with reduced conductivity.

measure $n_{2D} = 2.3 \times 10^{13}$ cm^{-2}, in excellent agreement with data reported in literature for pristine LAO/STO and LAO/ETO/STO samples [2, 42, 43]. Panel (b) shows the transverse resistance R_{xy} measured at $T = 5$ K for different values of the gate voltage. We observe that at high gate voltage, the data show a nonlinear behavior at low field ($H \sim 2$ T). It can be attributed to anomalous Hall effect taking place in ferromagnetic systems characterized by an intermediate/low carrier density and a non-negligible spin–orbit coupling, as previously reported for LAO/ETO/STO heterostructures [4, 43]. This result demonstrates that ferromagnetic properties are retained in patterned structures, with the same characteristics found in pristine samples.

Finally, we used a scanning SQUID microscopy to map the spatial distribution of current flow in patterned LAO/ETO/STO devices. The SQUID pickup loop captures the magnetic field lines generated by the current driven through the sample, as a function of location [44] (figure 5(a)). The current produces circulating magnetic fields around the sample. In a homogeneous sample the map shows positive (red) and negative (blue) field lines at the edges of the pattern, and a smooth flux profile inside the current carrying areas, as shown in the simulation of figure 5(b). Local distortions in the map of magnetic flux, for example dipoles or line features, point to the presence of defects, which could be localized regions, sometimes resolution limited, or elongated features [45]. These defects (regions with reduced or enhanced conductivity) distort the flow of current and therefore the distribution of magnetic field lines. Localized regions of reduced conductivity appear as a dipole-shaped signal in the raw data, reflecting the size of the defect, the shape of the sensor and the scan height. The data in figure 5(c) demonstrate that the patterned LAO/ETO/STO device presents homogeneous flow interrupted only by a few regions with reduced conductivity (likely related to defects in

the thin films), while the exposed STO areas show no indication of current carrying paths.

4. Conclusions

In this work we presented a fabrication technique based on low-temperature ion-milling for the realization of oxide 2DES complex nanodevices. This 'top down' approach involves a lithography step followed by an ion milling process where the sample is kept at low temperature, close to that of liquid nitrogen. The devices realized are stable over time and multiple thermal cycling between room and cryogenic temperatures. By a careful selection of the e-beam resist type and thickness, we realized nanodevices with dimensions down to 160 nm and properties comparable to that of pristine films. The strong tunability of the resistance of side gate devices demonstrates that no current paths are present in the etched STO areas between the nanochannels and the lateral electrodes, therefore the STO substrate keeps its insulating properties after the ion-milling process. The carrier concentration in the devices realized is comparable to that typically found in LAO/STO and LAO/ETO/STO 2DES. Scanning SQUID images confirm that no current flow outside the patterned areas, supporting the above conclusions.

The technique we present can be applied to all types of oxide heterostructures. In the present configuration, we estimate that an oxide thickness of maximum 10 nm can be etched before damaging the resist nanopattern. However, by resorting to a more robust e-beam resist this limit could probably be raised. Being a 'top down' approach, this technique does not involve manipulation of the substrate before thin films deposition, therefore it is particularly useful for the patterning of interfacial systems where termination and cleanliness of the substrate are of great importance. The formation of a LAO/ETO/STO 2DES is one of these cases: even a small amount of contaminants on the substrate could hamper the 2 u.c. ETO layer formation, resulting in an insulating LAO/ETO/STO interface. Furthermore, the technique we describe can be applied to a pre-tested heterostructure, increasing the yield of the nanofabrication procedure.

An important innovation our technique brings is also to expose the lateral sides of the devices, with little or no damage to the lateral areas of the system, giving the possibility to access the oxide 2DES from the side. This opens the way to the realization of hybrid normal/superconductor structures or even to superconductor/superconductor structures, where the 2DES could be proximized by another superconducting material. Adding the ferromagnetic properties of our LAO/ETO/STO heterostructures, many other exciting perspectives for a new class of hybrid devices can be envisaged.

Acknowledgments

We thank E Di Gennaro and A D Caviglia for fruitful discussions. This work was supported by the ERA-NET QUANTERA European Union's Horizon H2020 project QUANTOX under Grant Agreement No. 731 473, by the MIUR PRIN project TOP-SPIN (Grant No. PRIN 20 177SL7HC) and by the European Cooperation in Science and Technology COST Action CA16218 (NANOCOHYBRI). AK acknowledges support from the Swedish infrastructure for micro- and nanofabrication—MyFab. SWS and BK were supported by European Research Council Grant No. ERC-2019-COG-866236. SW and BK by the Israeli Science Foundation grant no. ISF-1281/17.

Data availability statement

The data that support the findings of this study are available upon reasonable request from the authors.

ORCID iDs

M D'Antuono https://orcid.org/0000-0001-7520-1243
A Kalaboukhov https://orcid.org/0000-0003-2939-6187
R Caruso https://orcid.org/0000-0002-9934-836X
B Kalisky https://orcid.org/0000-0002-1270-2670
G Ausanio https://orcid.org/0000-0003-3126-8504
M Salluzzo https://orcid.org/0000-0001-8372-6963
D Stornaiuolo https://orcid.org/0000-0003-2654-9504

References

[1] Zubko P, Gariglio S, Gabay M, Ghosez P and Triscone J M 2011 *Annu. Rev. Condens. Matter Phys.* **2** 141–65
[2] Ohtomo A and Hwang H 2004 *Nature* **427** 423–6
[3] De Luca G *et al* 2014 *Phys. Rev.* B **89** 224413
[4] Stornaiuolo D *et al* 2016 *Nat. Mater.* **15** 278–83
[5] Tuvia G, Frenkel Y, Rout P K, Silber I, Kalisky B and Dagan Y 2020 *Adv. Mater.* **32** 2000216
[6] Bréhin J *et al* 2020 *Phys. Rev. Mater.* **4** 041002
[7] Mannhart J and Schlom D G 2010 *Science* **327** 1607–11
[8] Coll M *et al* 2019 *Appl. Surf. Sci.* **482** 1–93
[9] Barthelemy A *et al* 2021 *Europhys. Lett.* **133** 17001
[10] Noël P *et al* 2020 *Nature* **580** 483–6
[11] Kornblum L 2019 *Adv. Mater. Interfaces* **6** 1900480
[12] Massarotti D, Miano A, Tafuri F and Stornaiuolo D 2020 *Supercond. Sci. Technol.* **33** 034007
[13] Chen L, Sutton E, Lee H, Lee J W, Li J, Eom C B, Irvin P and Levy J 2019 *Light: Sci. Appl.* **8** 1–7
[14] Dai W, Liang Y, Yang M, Schrecongost D, Gajurel P, Lee H, Lee J W, Chen J, Eom C B and Cen C 2019 *Nano Lett.* **19** 7149–54
[15] Zhang W, Zhang Q, Zhao M Q and Kuhn L T 2013 *Nanotechnology* **24** 275301
[16] Cen C, Thiel S, Mannhart J and Levy J 2009 *Science* **323** 1026–30
[17] Boselli M, Scheerer G, Filippone M, Luo W, Waelchli A, Kuzmenko A B, Gariglio S, Giamarchi T and Triscone J M 2021 *Phys. Rev.* B **103** 075431
[18] Briggeman M *et al* 2020 *Science* **367** 769–72
[19] Schneider C W, Thiel S, Hammerl G, Richter C and Mannhart J 2006 *Appl. Phys. Lett.* **89** 122101
[20] Stornaiuolo D, Gariglio S, Couto N, Fête A, Caviglia A, Seyfarth G, Jaccard D, Morpurgo A and Triscone J M 2012 *Appl. Phys. Lett.* **101** 222601

[21] Paolo Aurino P, Kalabukhov A, Tuzla N, Olsson E, Claeson T and Winkler D 2013 *Appl. Phys. Lett.* **102** 201610
[22] Scheurer M S and Schmalian J 2015 *Nat. Commun.* **6** 1–10
[23] Loder F, Kampf A P and Kopp T 2015 *Sci. Rep.* **5** 1–10
[24] Fukaya Y, Tamura S, Yada K, Tanaka Y, Gentile P and Cuoco M 2018 *Phys. Rev.* B **97** 174522
[25] Perroni C, Cataudella V, Salluzzo M, Cuoco M and Citro R 2019 *Phys. Rev.* B **100** 094526
[26] Stornaiuolo D, Massarotti D, Di Capua R, Lucignano P, Pepe G, Salluzzo M and Tafuri F 2017 *Phys. Rev.* B **95** 140502
[27] Kuerten L, Richter C, Mohanta N, Kopp T, Kampf A, Mannhart J and Boschker H 2017 *Phys. Rev.* B **96** 014513
[28] Wollman D, Van Harlingen D, Giapintzakis J and Ginsberg D 1995 *Phys. Rev. Lett.* **74** 797
[29] Kan D *et al* 2005 *Nat. Mater.* **4** 816–9
[30] McCaffrey J, Phaneuf M and Madsen L 2001 *Ultramicroscopy* **87** 97–104
[31] Singh G, Lesne E, Winkler D, Claeson T, Bauch T, Lombardi F, Caviglia A D and Kalaboukhov A 2021 *Nanomaterials* **11** 398
[32] Stornaiuolo D, Rotoli G, Massarotti D, Carillo F, Longobardi L, Beltram F and Tafuri F 2013 *Phys. Rev.* B **87** 134517
[33] Stornaiuolo D, Rotoli G, Cedergren K, Born D, Bauch T, Lombardi F and Tafuri F 2010 *J. Appl. Phys.* **107** 113901
[34] Papari G, Glatz A, Carillo F, Stornaiuolo D, Massarotti D, Rouco V, Longobardi L, Beltram F, Vinokur V and Tafuri F 2016 *Sci. Rep.* **6** 1–8
[35] Stornaiuolo D, Gariglio S, Fête A, Gabay M, Li D, Massarotti D and Triscone J M 2014 *Phys. Rev.* B **90** 235426
[36] Fragneto A, De Luca G, Di Capua R, Scotti di Uccio U, Salluzzo M, Torrelles X, Lee T L and Zegenhagen J 2007 *Appl. Phys. Lett.* **91** 101910
[37] Salluzzo M, Gariglio S, Torrelles X, Ristic Z, Di Capua R, Drnec J, Sala M M, Ghiringhelli G, Felici R and Brookes N 2013 *Adv. Mater.* **25** 2333–8
[38] Minhas M, Blaschek H, Heyroth F and Schmidt G 2016 *AIP Adv.* **6** 035002
[39] Liu W, Gariglio S, Fête A, Li D, Boselli M, Stornaiuolo D and Triscone J M 2015 *APL Mater.* **3** 062805
[40] Yin C, Smink A E, Leermakers I, Tang L M, Lebedev N, Zeitler U, Van Der Wiel W G, Hilgenkamp H and Aarts J 2020 *Phys. Rev. Lett.* **124** 017702
[41] Pallecchi I, Lorenzini N, Safeen M A, Can M M, Di Gennaro E, Granozio F M and Marré D 2021 *Adv. Electron. Mater.* **7** 2001120
[42] Thiel S, Hammerl G, Schmehl A, Schneider C W and Mannhart J 2006 *Science* **313** 1942–5
[43] Stornaiuolo D *et al* 2018 *Phys. Rev.* B **98** 075409
[44] Persky E and Kalisky B 2018 *Adv. Mater.* **30** 1706653
[45] Kalisky B *et al* 2013 *Nat. Mater.* **12** 1091–5

Orbital selective switching of ferromagnetism in an oxide quasi two-dimensional electron gas

R. Di Capua[1,2], M. Verma[3], M. Radovic[4], V.N. Strocov[4], C. Piamonteze[4], E. B. Guedes[4], N. Plumb[4], Yu Chen[2], M. D'Antuono[1,2], G.M. De Luca[1,2], E. Di Gennaro[1,2], D. Stornaiuolo[1,2], D. Preziosi[5], B. Jouault[6], F. Miletto Granozio[2], A. Sambri[2], R. Pentcheva[3], G. Ghiringhelli[7,8] and M. Salluzzo[2]*

[1]*Dipartimento di Fisica "E. Pancini", Università di Napoli "Federico II", Complesso Monte Sant'Angelo via Cinthia, I-80126 Napoli, Italy.*
[2]*CNR-SPIN, Complesso Monte Sant'Angelo via Cinthia, I-80126 Napoli, Italy.*
[3]*Department of Physics and Center for Nanointegration, University Duisburg-Essen Lotharstr. 1, D-47057 Duisburg, Germany.*
[4] *Photon Science Division, Paul Scherrer Institut, CH-5232 Villigen PSI, Switzerland.*
[5] *Université de Strasbourg, CNRS, IPCMS UMR 7504, 67034 Strasbourg, France.*
[6] *Laboratoire Charles Coulomb, UMR 5221, CNRS, Université de Montpellier, F-34095 Montpellier, France*
[7] *Dipartimento di Fisica Politecnico di Milano, Piazza Leonardo da Vinci 32, I-20133 Milano, Italy.*
[8]*CNR-SPIN, Politecnico di Milano, Piazza Leonardo da Vinci 32, I-20133 Milano, Italy.*

* marco.salluzzo@spin.cnr.it

ABSTRACT

Multi-orbital physics in quasi-two-dimensional electron gases (q2DEGs) triggers unique phenomena not observed in bulk materials, such as unconventional superconductivity and magnetism. Here, we investigate the mechanism of orbital selective switching of the spin-polarization in the oxide q2DEG formed at the (001) interface between the $LaAlO_3$, $EuTiO_3$ and $SrTiO_3$ band insulators. By using density functional theory calculations, transport, magnetic and x-ray spectroscopy measurements, we find that the filling of titanium-bands with $3d_{xz,yz}$ orbital character in the $EuTiO_3$ layer and at the interface with $SrTiO_3$ induces an antiferromagnetic to ferromagnetic switching of the exchange interaction between Eu-$4f^7$ magnetic moments. The results explain the observation of the carrier density dependent ferromagnetic correlations and anomalous Hall effect in this q2DEG, and demonstrate how combined theoretical and experimental approaches can lead to a deeper understanding of novel electronic phases and serve as a guide for the materials design for advanced electronic applications.

Introduction

Since the discovery of a quasi-two-dimensional electron gas (q2DEG) at the interface between the $LaAlO_3$ (LAO) and $SrTiO_3$ (STO) band insulators [1], studies on oxide surfaces and interfaces uncovered an intriguing and rich physics, boosting the expectations for all-oxide electronics. The LAO/STO q2DEG shows remarkable properties, including electric field effect induced insulator-to-metal transition at room temperature [2], gate-tunable Rashba-like spin-orbit coupling [3, 4], superconductivity [5-7], and magnetism [8]. From these studies, a fundamental role of the multi-orbital nature of the carriers in the electronic properties of the oxide q2DEGs clearly emerged.

The possibility to induce ferromagnetic (FM) correlations at the interface between non-magnetic oxides, combined with the large spin to charge conversion efficiency of oxide q2DEGs [9], paves the way to applications in spintronics. However, the reported magnetism at the bare LAO/STO interface is believed to be related to defects and oxygen vacancies [10] more than intrinsic coupling of electronic states.

Recently, it has been shown that a feasible method to induce a spin-polarization in oxide q2DEG is the introduction of a thin magnetic layer between LAO and STO, like $EuTiO_3$ (ETO) (Fig. 1a) [11, 12] and $LaMnO_3$ [13]. FM correlations were reported also in heterostructures where LAO is replaced by a ferro(ferri)-magnetic insulator, as in $GdTiO_3$/STO (13, 14), EuO/STO [16] and $LaAl_{1-x}Mn_xO_3$/STO [17].

In LAO/ETO/STO, FM correlations are believed to be induced by the ordering of localized Eu^{2+} $4f^7$ magnetic moments and their coupling with Ti-*3d* states forming the conduction band of the q2DEG. However, the microscopic mechanism leading to these phenomena is not straightforward, as rare earth magnetic ions have usually a small hybridization with transition metal *3d* orbitals. Unlike the LAO/STO q2DEG [1-9], there is no detailed study of the electronic band structure of LAO/ETO/STO heterostructures, and it remains unclear whether a spin-polarized q2DEG is present in both ETO and interfacial STO layers, which is relevant for the intriguing phase diagram showing a transition from a FM to a superconducting state [12]. Additionally, FM correlations were observed only above the Lifshitz transition, where carriers with $3d_{xz,yz}$ orbital character start to contribute to the transport [12].

In this work all these questions are settled by combining extensive experimental and theoretical investigations. Firstly, we show that low temperature electrical transport, x-ray magnetic circular dichroism (XMCD) and superconducting quantum interference device (SQUID) experiments give evidence of tunable ferromagnetism originating from the correlation between Ti- and Eu- magnetic moments. Secondly, we provide a direct picture

of the q2DEG band structure by using resonant soft-x-ray photoemission spectroscopy (RESPES). These experimental observations are finally compared and blended with Density Functional Theory calculations with on-site Hubbard terms (DFT+*U*). The latter show that the q2DEG forms at the ideal LAO/ETO interface and extends few unit cells into the STO. FM correlations are induced by the delicate balance between different antiferromagnetic (AFM) and FM contributions to the exchange interaction between Eu-$4f^7$ magnetic moments and Ti-*3d* electrons at the ETO/STO interface, which involves also the first STO unit cells (uc), in agreement with the experiments. Moreover, theoretical calculations show that the ferromagnetism in the q2DEG and the filling of $3d_{xz,yz}$ bands take place simultaneously, explaining the electric field induced anomalous Hall effect above the Lifshitz point [12], and the orbital selective switching of the ferromagnetism in an oxide q2DEG.

Results

I. Experimental evidence of intrinsic ferromagnetic correlations

Bulk ETO is an AFM insulator with a Neel temperature of 5.5 K. However, doping or lattice strain favor a FM order in epitaxial films [18-22]. ETO has a quasi-perfect structural matching with STO and a similar conduction band formed by the overlap of t_{2g} Ti-*3d* orbitals. By embedding few unit cells of ETO between LAO and STO using epitaxial growth by pulsed laser deposition, we realized a q2DEG characterized by electrical transport properties similar to the LAO/STO q2DEG. However, at low temperatures and at a carrier density $>2.10^{13}$ cm^{-2} tuned by electric field effect (Fig.1a), the sheet resistance exhibits a downturn below T=6-8 K (Fig.1b), which correlates to the FM transition of doped ETO [12]. The heterostructures itself is characterized by a FM transition (T_c=6-8 K) and a FM ground state, as shown in Fig.1c, where we compare the maximum intensity of the Eu-XMCD signal (at M_5-edge, scatter data), acquired at 2 K at the X-Treme beamline of the Swiss Light Source (SLS) [23], to macroscopic SQUID magnetometry data (full lines) as a function of the magnetic field in parallel (red line) and perpendicular (black line) directions. The two sets of data, normalized to the saturation value for direct comparison, show a small, although clear, hysteresis around zero magnetic field and a preferential orientation of the magnetization parallel to the interface, confirming a finite low magnetic field magnetization and FM correlations. The magnetization saturates above 2-3 Tesla (depending on the sample and on the magnetic field direction), indicating that all the Eu^{2+}-spin moments order ferromagnetically above these values.

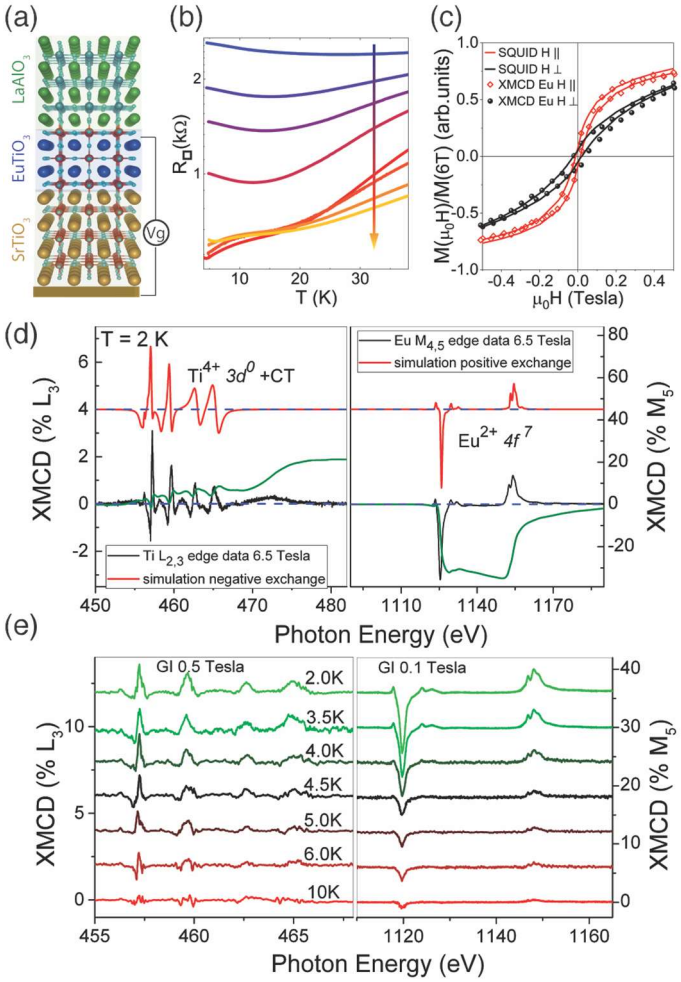

Fig. 1. Structure and general transport and magnetic properties of LAO/ETO/STO heterostructures. (a) Sketch of the LAO/ETO/STO heterostructure. In this work, the carrier concentration was tuned using electric field effect in back-gate configuration, as sketched in the figure. (b) Sheet resistance vs. temperature as a function of the gate voltage Vg. The arrow indicates increasing values of Vg from -30 to 30 V. (c) Eu-XMCD (scatter data) and SQUID magnetization (continuous lines) as function of the magnetic field parallel (red) and perpendicular (black) to the interface. The data are normalized to the saturation value. The Eu-XMCD in parallel direction is obtained by combing data acquired in grazing (60 degrees from the surface normal) and normal incidence conditions. (d) XMCD data at the Ti-L (right) and Eu-M (left) edges at 6.5 Tesla. Red-lines are atomic multiplet simulations, green lines are integrals of the XMCD spectra (see main text). (e) Temperature dependence of the Ti-$L_{2,3}$ (0.5 Tesla) and Eu-$M_{4,5}$ (0.1 Tesla) edges XMCD spectra in grazing incidence conditions. Data are vertically shifted for clarity.

To further elucidate the magnetic properties of the system, in Fig.1d we show XAS and XMCD spectra at the Ti-$L_{2,3}$ and Eu-$M_{4,5}$ edges at 2 K and 6.5 Tesla and in Fig.1e the XMCD temperature dependence in grazing incidence conditions (60 degrees from the surface normal). The data show that Eu- and Ti- XMCD spectra follow each other, thus are correlated. In particular the Ti- (orbital and spin) and the Eu- magnetic moments have the same temperature dependence, with a T_c of the order of 6-8 K. Moreover, they have the same magnetic field dependence as shown in ref. [12].

In Figure 1d, the XMCD spectra are compared to atomic multiplet simulations (red lines) for Eu^{2+} and Ti^{4+} ions in C4 symmetry, the latter including the crystal field splitting reproducing the x-ray linear dichroism data, and a charge transfer (CT) term to account for the hybridization between Ti-*3d* and O-*2p* states in the TiO_6 cluster (see Supplementary materials from page 24, and ref. [24]). The calculations reproduce most of the features shown by the experiment. However, while a positive exchange is needed to simulate the Eu^{2+} magnetization, parallel to the magnetic field, only a negative one correctly reproduces the Ti-XMCD peaks at L_3 and L_2. On the other hand, we also find a finite and positive Ti-XMCD integral that, according to the sum rules [25], corresponds to a sizeable Ti-*3d* orbital moment, m_{orb}, of the order of -0.05 μ_B/Ti, opposite to the magnetic field. While the application of the sum rules does not accurately provide the spin-moment at the Ti-$L_{2,3}$ edge, following the Hund's rules, the sign of the orbital moment corresponds to a finite Ti-spin moment parallel to the Eu-spin moment.

However, the Ti-XMCD integral and the Ti- magnetic moment is expected to be null for a Ti-$3d^0$ state, even in the presence of a CT between Ti-*3d* and neighbor O-*2p* states. Thus, the only way to explain the results is the presence of two contributions to the Ti-XMCD spectra: (i) a $3d^0$+CT contribution (i.e. $3d^0$ and $3d^1\underline{L}$, with $\underline{L}$ the O*2p*-Ti*3d* ligand state), due to the negative exchange interaction between the ligand Ti*3d* electrons and the Eu^{2+} magnetic moments, which gives rise to a circular polarization dependence of the cross-section for the $2p^63d^0$ ($3d^1\underline{L}$) to $2p^53d^1$($3d^2\underline{L}$) transition; (ii) a second contribution coming from Ti-$3d^1$ electronic states, with their associated magnetic moments, parallel to the magnetic field and to the Eu^{2+} spin-moments. These results suggest different typologies of exchange interactions between Eu and Ti ions i.e., an AFM one between Eu^{2+} and Ti-$3d^0$+*CT* states, and a FM exchange between the Eu^{2+} and Ti-$3d^1$ spin-moments.

The FM correlations in the q2DEG, and the magnetic field dependence of the magnetization are directly related to the Hall effect data [12], which exhibit at low field (<3 Tesla) a curvature change associated to the anomalous Hall effect (AHE) (Fig.2a). Further insights on the nature of the AHE is obtained by comparing the 2D anomalous conductivity, σ_{AHE}, to the longitudinal one, σ_{xx}, estimated according to eq.(*1a,1b*):

$$\sigma_{xx} = \frac{\rho_{xx}^{2D}(0)}{(\rho_{AHE})^2 + \left(\rho_{xx}^{2D}(0)\right)^2} \qquad (1a)$$

$$\sigma_{AHE} = \frac{\rho_{AHE}}{(\rho_{AHE})^2 + \left(\rho_{xx}^{2D}(0)\right)^2} \qquad (1b)$$

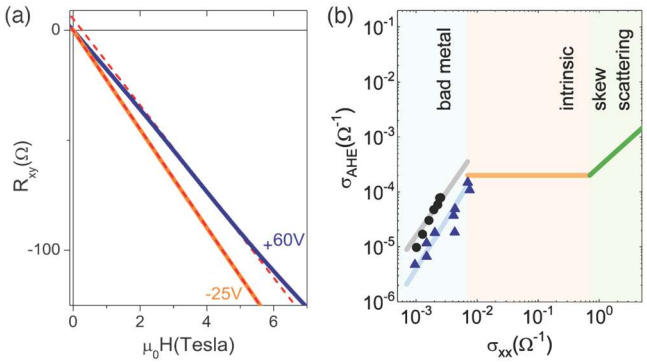

Fig. 2. Analysis of the anomalous Hall effect. (a) Transverse (Hall) resistance R_{xy} as a function of the magnetic field for two values of the gate voltage. The high gate voltage +60 V (higher carrier concentration) data show negative curvature at low field (μ_0H<2.5 T) and a positive curvature at high field (μ_0H >5T). The former is due to the anomalous Hall component, the latter to multiband transport. The red dashed lines are linear fit in the range 3-4 Tesla, and the intercept is the AHE component at saturation. (b) Anomalous Hall conductivity vs. longitudinal 2D conductivity (see main text eq.1). Black dots and blue triangles refer to two LAO/ETO/STO samples. Full lines refer to the exponent α in the relation $\sigma_{AHE} \propto (\sigma_{xx})^{\alpha}$: α=1.8 (light blue, and gray, intrinsic AHE suppressed by disorder), α=0 (orange, intrinsic AHE), α=1(green, skew scattering).

where $\rho_{xx}^{2D}(0)$ is the zero field 2D resistivity, and ρ_{AHE} is the saturation value of the anomalous Hall 2D resistivity, as calculated from the anomalous component of the Hall effect (Fig. 2a and refs. [12, 19]). The origin of the AHE can be attributed to different mechanisms, which can be phenomenologically distinguished from the relationship between σ_{AHE} and σ_{xx}. According to the literature [26], most of the materials showing an AHE can be classified in the following three regimes: (i) a high conductivity range, where $\sigma_{AHE} \propto \sigma_{xx}$ and the observed AHE is attributed to scattering from unwanted magnetic impurities (skew scattering); (ii) an intermediate conductivity range, where σ_{AHE} is independent from σ_{xx} and the AHE is related only to the Berry curvature of the involved bands (intrinsic AHE); (iii) a bad metal range where $\sigma_{AHE} \propto (\sigma_{xx})^{\alpha}$, with α in the interval 1.6-1.8, where the intrinsic AHE is suppressed by the disorder. In the latter two ranges the AHE is due to the spin-polarization of the carriers and to the spin-orbit coupling breaking both time and inversion symmetry. Data collected on two LAO/ETO/STO representative samples, with carrier densities tuned by a back-gate voltage, are shown in Fig.2b. We found a correlation $\sigma_{AHE} \propto (\sigma_{xx})^{\alpha}$, with α=1.8, which excludes a skew scattering mechanism and a purely intrinsic AHE. We conclude that in LAO/ETO/STO an intrinsic AHE suppressed by disorder is at play, analogously to what found in La-doped ETO films [20].

II. Experimental investigation of the band structure via RESPES

In order to characterize the electronic structure of the LAO/ETO/STO system, we used the RESPES technique at the soft-x-ray end station of the ADvanced RESonant Spectroscopies (ADRESS, X03MA) beamline of the Swiss Light Source (SLS) [27, 28]. The experimental data were acquired at base temperature (12 K) thus above the FM transition of the system.

In Fig. 3a we report angle and photon-energy integrated (across the Ti-$L_{2,3}$ edge) RESPES VB data on (001) LAO(5uc)/ETO(2uc)/STO and a reference PLD grown (001) LAO(5uc)/STO sample containing oxygen vacancies, i.e. cooled down from the high deposition temperature (750 °C) in a reduced oxygen pressure of the order of 10^{-5} mbar, without any high-O_2 pressure annealing process. For comparison we show also data acquired by high resolution ARPES at the SIS (Surface Interface Spectroscopy) beamline of SLS ($h\nu$ = 85 eV), on reference VB of an STO crystal and of an ETO film hosting q2DEGs [35].

Since the escape depth of the photoelectrons in the 450-470 eV range is of the order of 1-2 nm, in LAO(5)/ETO(2)/STO the data have contributions from both the ETO layers and from the interfacial STO unit cells. As a result, the VB spectra of ETO heterostructures show prominent differences respect to the STO and LAO/STO VB. The main one is the presence, in ETO and in LAO/ETO/STO, of a peak at -1.95 eV binding energy (BE), due to Eu^{2+} - $4f^7$ states. Another important difference between the STO and LAO/STO q2DEGs containing oxygen vacancies, and the ETO q2DEGs is the absence in the latter of the -1.0 eV in-gap state (IGS). The IGS is a distinctive characteristic of the STO q2DEGs and of oxygen deficient LAO/STO [28]. Finally, in LAO/ETO/STO we observe the evidence of a further broad feature at BE lower than -8 eV, which reflects the contribution of Eu in Eu^{3+} oxidation state: through a Gaussian deconvolution of the observed spectral features (reported in Fig. 3a), we estimated a fraction of Eu^{3+} of about 25%. This result is in agreement with reported atomically resolved high resolution transmission electron microscopy and electron energy loss spectroscopy [12], which show that a similar fraction of Eu^{3+} is present in the system, mostly located into the LAO layer at the interface with the ETO film.

In Fig. 3b we report angle integrated VB-RESPES data of LAO(5uc)/ETO(2uc)/STO at photon energies hν across the Ti-*2p* absorption edge resonance. The data are overlapped to TEY XAS (white line), and to Constant Initial State (CIS) spectra obtained by integrating the valence band over different binding energy ranges. CIS spectra allows the

identification of the resonance of different VB features with the XAS intensity spectra. We can see that the same XAS resonances characteristic of Ti^{4+} ions appear as higher intensity signal in the RESPES map inside the contribution from the O-*2p* band. Similar results have been reported for the LAO/STO q2DEG [28], and are a consequence of the hybridization between O-*2p* and Ti-*3d* states. On the other hand, the CIS spectrum around the Fermi level, related to the q2DEG conduction band, has a different shape, reminding the characteristic absorption from Ti^{3+} ions in an octahedral environment, similar to bulk $LaTiO_3$ [29] (see Supplementary Materials, from page 24). Surprisingly, also the peak at -2 eV resonates with the Ti-absorption spectrum, a result which would point to a hybridization of Eu with O-*2p* and Ti-*3d* states. This is rather unexpected, since *4f* rare earth orbitals have usually little overlap with neighbor ions in a crystal.

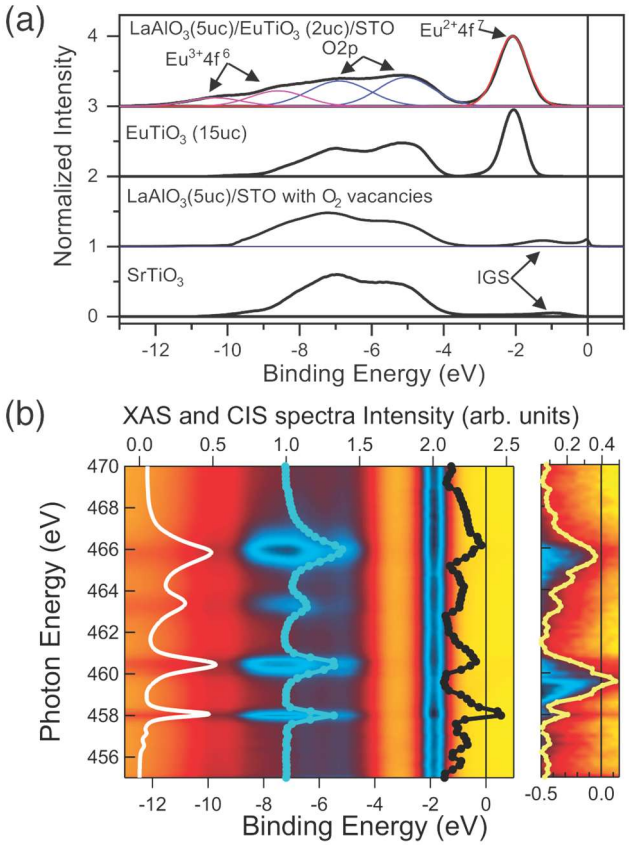

Fig. 3. RESPES and ARPES VB data. (a) Angle integrated ARPES VB data of $SrTiO_3$, and $EuTiO_3$ q2DEG surface state, compared to angle and photon-energy integrated RESPES VB of (001) LAO(5uc)/STO (containing oxygen vacancies) and LAO(5uc)/ETO(2uc)/STO heterostructures. Multiple gaussian fit of the LAO/ETO/STO VB profile is used to determine the Eu^{3+}/Eu^{2+} ratio. The IGS in gap states is observed only in STO and LAO/STO q2DEGs due to the presence of oxygen vacancies. (b) (left panel) RESPES color-map of the valence band region and constant initial state spectra obtained integrating the RESPES data around BE = -2 eV (Eu^{2+}, black scatter data) and between -7 and -4 eV (O-*2p*, cyan scatter data). The white line is the total electron yield XAS spectrum; (right panel) the same RESPES map in the Fermi level region and corresponding CIS spectrum (yellow scatter data).

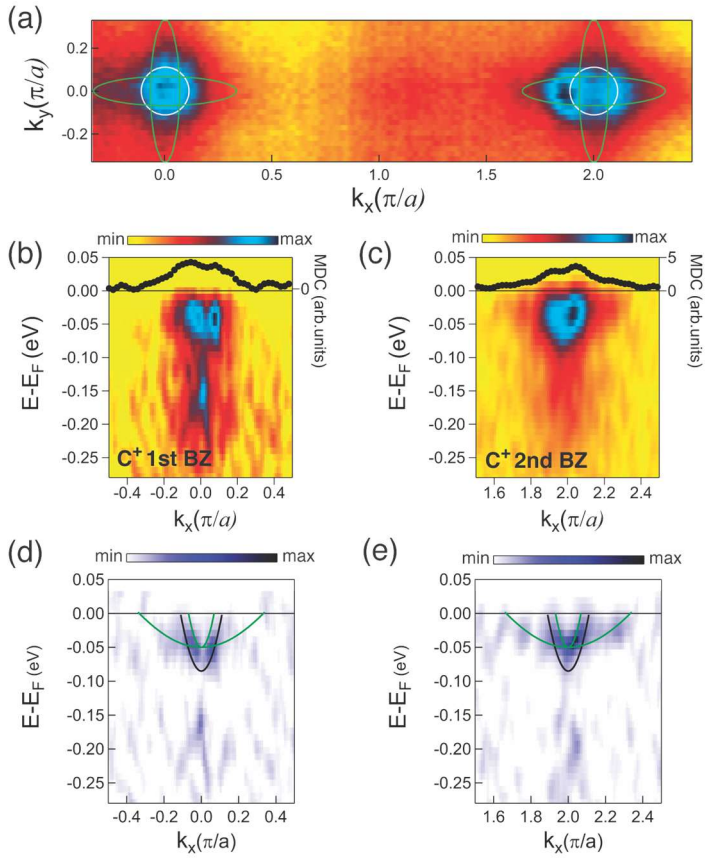

Fig. 4: Resonant angle resolved photoemission spectra. (a) Average between circular plus and circular minus Fermi surface map of the (001) LAO/ETO/STO heterostructure. Dashed lines are Fermi surface contours of light (white) and heavy (green) bands. (b) and (c) E vs. k_x band dispersions maps acquired with C+ polarization in the 1st and 2nd BZ. Black scatter data on top of each band dispersion map are the Fermi level MDCs curves (integrated around E_F in a 10 meV range). All the data are measured in resonance conditions (465.5 eV). (d) and (e) two-dimensional curvature maps of the C+ dispersions in (c) and (d), with tight-binding fitting of the bands (green lines $3d_{xz}$ and $3d_{yz}$ bands, black line $3d_{xy}$ band).

In order to characterize the band structure of the LAO/ETO/STO q2DEG, in Fig. 4a we show k_x-k_y in-plane cut of the Fermi Surface (FS), obtained by averaging circular minus (C-) and circular plus (C+) polarization spectra at an incoming photon energy of 465.5 eV, resonant with the Ti^{3+} L_2 absorption peak. Overlapped to the map we also show Fermi surface contours associated to non-interacting electronic bands originated from atomic Ti-$3d$-t_{2g} states: namely, a ring-shaped feature and two ellipsoidal structures oriented lengthwise along the k_x and k_y directions. The ring-shaped Fermi contour corresponds to light effective mass electrons having mainly $3d_{xy}$ orbital character, while the ellipsoidal ones are related to heavy effective masses electrons with mainly $3d_{xz}$-$3d_{yz}$ orbital characters. The qualitative features of the measured FS in (001) LAO/ETO/STO resemble those observed on different oxide systems characterized by the presence of a q2DEG, like

the (001) STO surface [30, 31], the (001) LAO/STO interface [32-34], and the recently investigated (001) ETO surface [35]. However, the FS, in particular at the 2nd BZ, where heavy bands contributions are better resolved due to matrix element effects, has a shape which departs from the simple tight binding model of three non-interacting t_{2g} bands.

In Figs. 4b-c we show band dispersion cuts at the 1st and 2nd BZ through the Γ-point along the k_x direction (corresponding to Γ-X in reciprocal space) with circular plus (C^+) polarization of the incoming photons (C+ pol, hν = 465.5 eV). Momentum Dispersion Cuts (MDCs) at the Fermi level are shown on the top of each panel. In Fig. 4d-e we show the corresponding 2D-curvature maps to highlight the different bands [36]. Other data acquired with different polarizations of the incoming photons are shown in the Supplementary Materials (from page 24).

The dispersive profile of the different bands were obtained by combining the 2D-curvature maps and the fit of the maxima of MDCs at several energies below the Fermi level, in analogy with previous studies on LAO/STO q2DEGs [33, 34] (see Supplementary Materials, from page 24). From simple tight-binding fitting assuming three independent bands (superimposed to the 2D curvature maps of Fig. 4d-e), we estimated the effective masses m* at the Fermi level of each band (see Table 1). We obtained m* = 0.4 m_e for the $3d_{xy}$ band, while for the heavy bands we estimated m* = 0.25 m_e and ~10 m_e in the "light" and "heavy" directions, respectively (m_e being the free electron mass). The $3d_{xy}$ band effective mass and the $3d_{xz,yz}$ bands effective masses along the "light" directions are typically smaller than the ones estimated for the LAO/STO system [33]. The splitting between the heavy- and light- band bottoms is of the order of ~ 35 meV at the Γ-point, considerably smaller than that usually reported for the STO-surface 2DEGs [30], but consistent with our earlier reports about the differences between the ETO and STO surface states [35], and in quantitative agreement with x-ray linear dichroism data on (001) LAO/ETO/STO [12].

Table 1: Fermi momentum k_F, band bottom E(0) and effective mass of the various bands.

Bands	k_F (Å^{-1})	E(0) (meV)	m*/me
$3d_{xy}$	0.09±0.01	-85±5	0.4±0.1
$3d_{yz}$	0.27±0.02	-50±5	10±2
$3d_{xz}$	0.055±0.005	-50±5	0.25±0.05

III. Results of DFT+*U* calculations

In order to understand the mechanism at the base of the formation of the q2DEG in LAO/ETO/STO and of the spin-polarization of its carriers, we performed DFT+*U* calculations [37-42] on an ideal c(2x2) LAO/ETO/STO (001) heterostructure composed by 5uc of LAO, 2uc of ETO and 4uc of STO stacked along the c-axis, and a vacuum region of 20 Å (Fig. 5a). On-site effective Hubbard parameter *U* = 4 eV, 7.5 eV and 8 eV were applied on the Ti-*3d*, Eu-*4f* and *La-4f* states, respectively. Similar to findings for the ETO (001) surface state [35], the choice of *U* for the Eu-*4f* states, and partially for the Ti-*3d* states, is dictated by the necessity to reproduce the position of the Eu^{2+} peak in the valence band at about -2 eV. We tested models with the Eu-ions in AFM (G-type) and FM configurations. We found that the FM solution is the lowest in energy for the system (about -20 meV per simulation cell). This result is in full agreement with the experimental evidence of a FM ordering of Eu^{2+} magnetic moments shown in Figs.1-2 and in ref.[12].

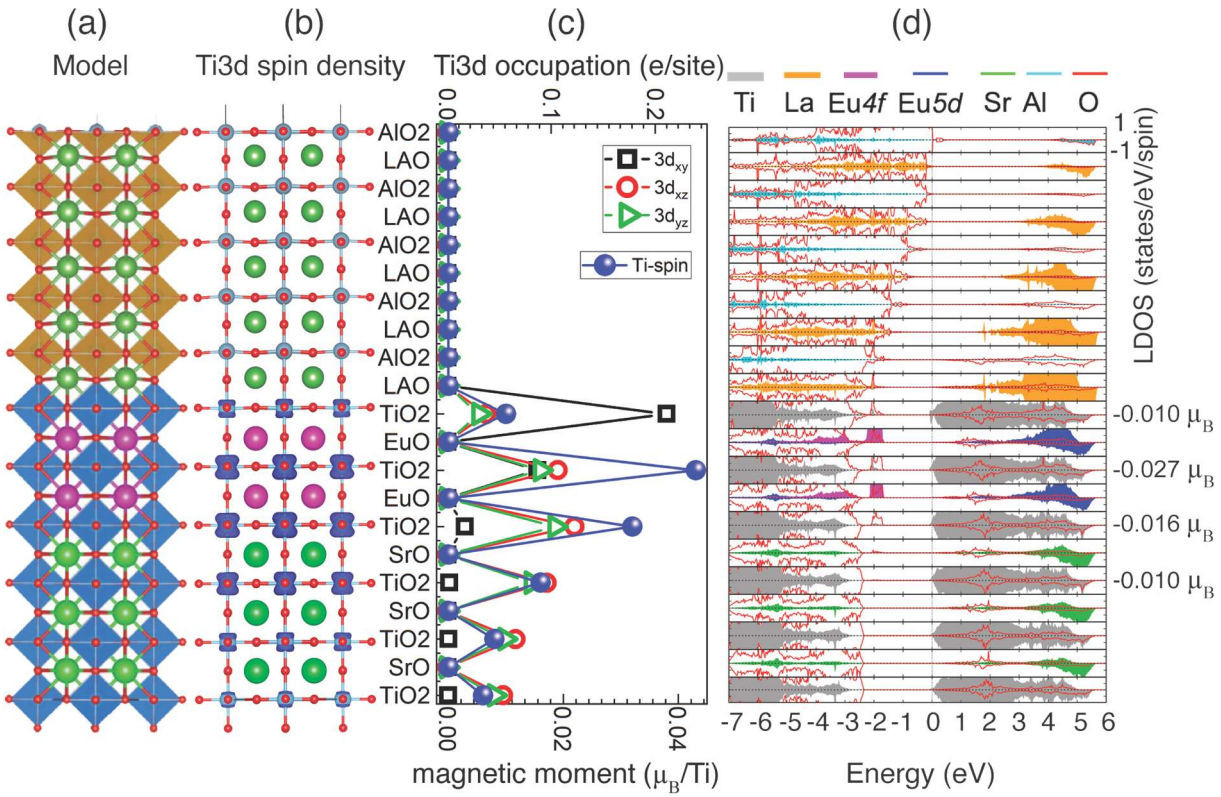

Fig. 5. DFT+U calculations: (a) Structural model of a c(2x2) LAO/ETO/STO(001) heterostructure; (b) integrated Ti-*3d* spin density plot with isovalue of 0.0004 e/Å^3 across the interface. (c) orbital and layer resolved Ti-*3d* occupation (upper scale; black squares, $3d_{xy}$; red circles, $3d_{xz}$, green triangles, $3d_{yz}$) and Ti-*3d* magnetic moment (lower scale; blue circles) obtained by integrating the density of states between -0.3 eV and E_F. d) Layer-, spin- and element- resolved density of states. The color code for the partial LDOS contribution of different ions is indicated on top of the figure. On the right side of the figure, we also indicate the values of the calculated oxygen-*2p* magnetic moment in the corresponding interfacial TiO_2 layers.

In Fig. 5 we show the Ti-*3d* spin density (Fig. 5b), the orbitally resolved Ti-*3d* occupation and magnetic moments (Fig. 5c), and the layer, atomic and spin resolved, local density of states (LDOS, Fig. 5d) across the interface. According to the DFT+*U* results, the q2DEG at the LAO/ETO/STO interface is formed through the transfer of electrons from the AlO_2 surface layer of LAO to the Ti-states in the ETO and STO layers in order to eliminate the polar discontinuity at the LAO/ETO interface. This is evidenced by the overlap between the energy positions of the O-*2p* band of the AlO_2 surface and of the interfacial TiO_2 *3d*-conduction bands in Fig. 5d, analogously to what happens in LAO/STO bilayers. We underline that ETO planes are formally neutral along the (001) direction alike STO, as Eu is mostly in Eu^{2+} valence state. Figure 5c shows that the q2DEG is characterized by a high occupation of Ti-*3d* states within the ETO layer, which goes to zero within few unit cells of STO. $3d_{xy}$ bands are the first to be occupied at the interface and are mostly localized into the ETO film.

The bands are spin-polarized, with the highest polarization within the ETO layers, which exhibit also the largest electron occupation. In particular, the model shows that most of the electrons filling the STO unit cells have a $3d_{xz,yz}$ orbital character, reflecting the wider distribution of these carriers, as also observed in (001) STO [30]. The Ti-*3d* magnetic moment, obtained by integrating the spin-resolved density of states in the range between -0.3eV and E_F (i.e. the contribution from spin-polarized conduction bands) is maximum in the second ETO layer, and then goes to zero within the first three-unit cells of STO (Figure 5c). Consequently, both ETO and topmost STO unit cells host electrons which are spin-polarized. The associated magnetic moment is parallel to the large spin-moment of Eu^{2+} states (6.97 μ_B). The layer resolved map in Figure 5d shows also a finite spin-polarized electron density of Ti-*3d,* Eu-*5d* and O-*2p* states at the position of the Eu^{2+} peak, demonstrating a hybridization between Eu-*4f*, Eu-*5d*, O-*2p* and Ti-*3d* states, in agreement with RESPES data. Moreover, O-*2p* states in the TiO_2 layers of ETO also acquire a finite spin-moment, opposite to the Ti-$3d^1$ and Eu-$4f^7$ magnetic moments. This can explain the two components of the XMCD spectra, one related to the Ti-$3d^0$ +CT states, with a negative exchange interaction with the Eu^{2+} *4f* states, and the other from Ti-$3d^1$ spin-polarized electrons, parallel to the overall magnetization direction.

To shed light on the bands contributing to the q2DEG, we show in Fig. 6a the calculated, spin resolved, band structure of LAO/ETO/STO (001) in the FM ground state in a large energy range around E_F, including the Eu^{2+}-*4f* state around -2 eV. Theory predicts several non-spin-polarized bands in the -1.5 eV to E_F binding energy range deriving from the LAO contribution to the density of states, including a (hole-) band (green line in the

figure) crossing the Fermi level associated with the AlO_2 surface state (LAO SS). The LAO related bands are not observed in the RESPES data, in agreement with previous studies on standard LAO/STO interfaces [32-34], indicating that the LAO exposed surface is not ideal and can be passivated by adsorbates, in particular after ambient exposure.

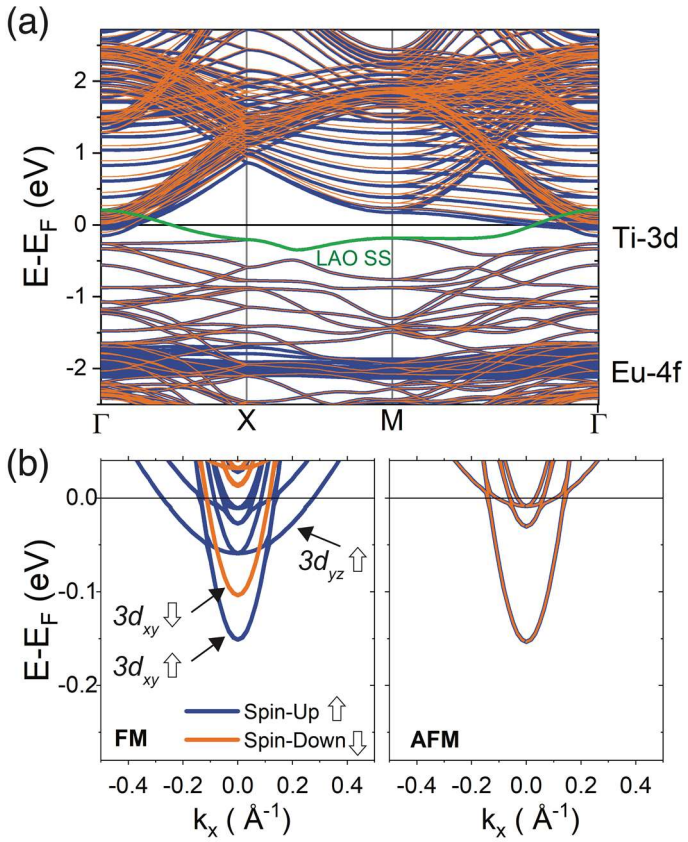

Fig. 6. Spin-resolved band structure from the DFT+*U* calculations: (a) Band structure DFT+*U* calculations on LAO/ETO/STO system in the FM ground state (lowest energy configuration). Spin-up/spin-down bands are denoted in blue/orange. The LAO surface state (LAO SS) is outlined as a green line. The Eu-*4f* band around -2 eV is fully spin-polarized. In the figure Γ-X-M refer to the c(2x2) unit-cell notation (Note that Γ–M in the c(2x2) unit cell is equivalent to Γ–X in the (1x1) unit cell). (b) Spin-resolved band structure calculations of the Ti-*3d* bands around the Γ-point in a small energy range in the FM (left panel) and AFM (right panel) solutions of the model. Note that in the FM solution, the spin-up $3d_{yz}$ band shift to lower energy and crosses the Fermi level, while the $3d_{xy}$ spin down bands shifts-up, giving rise to an overall spin-polarization of the q2DEG.

In order to compare the experimentally determined band structure shown in Fig. 4 with DFT+*U* calculations, and to highlight the differences between the conduction bands in the FM (the ground state) and AFM solutions of the model, we show in Fig. 6b the calculated Ti-*3d* band structure in the two cases (left panel FM, right panel AFM) in a small energy region around the Fermi level. In the case of the AFM state, we have forced a (G-type)

ordering of the Eu-spin moments. It turns out that the calculated band structures are qualitatively consistent with the main characteristics of the experimentally determined band properties shown in Fig. 4. In both the FM (Fig.6b, left panel) and AFM (Fig.6b, right panel) solutions, the lowest lying Ti-*3d* band crossing E_F is a dispersive parabolic band with d_{xy} orbital character, which switches at larger momentum into a much flatter band indicating an avoided crossing with the heavy bands with d_{xz}, d_{yz} orbital character. The higher-lying bands around Γ are replicas from different layers due to the confinement of the q2DEG. In the FM solution of the model, spin-up (blue) and spin-down (orange) bands, both of the d_{xy}, and $d_{xz,yz}$ main orbital character, are split in the whole energy range and cross the Fermi level, showing a prevalence of majority spin-polarized electrons in the system, in full agreement with all the experimental evidences of FM correlations in the q2DEG. In the AFM case the spin-degenerate $3d_{xy}$ bands arrange in the same energy region as the spin-up band of the FM phase, while $3d_{xz,yz}$ bands are lifted above the Fermi level. Thus, the conduction band minimum, associated with the lowest $3d_{xy}$ band is the same in both AFM and FM phases, but all the other bands are shifted in the FM solution. DFT+*U* calculations in particular show a down-shift of the spin-up $3d_{xz,yz}$ bands and more importantly a filling of these bands taking place only in the FM ground state. Thus, ferromagnetism appears simultaneously with the orbital selective filling of $3d_{xz,yz}$ electrons at the Fermi level, confirming their crucial role in establishing FM correlations in the q2DEG as earlier suggested in ref. [12].

Discussion

The experimental and theoretical results on LAO/ETO/STO (001) heterostructure show an interaction between Eu^{2+}-*4f* and Ti-*3d* states. This is rather surprising considering the large value of the Hubbard parameter on the $4f^7$ orbitals, and their strong electron localization, rendering them not far from a configuration with electrons frozen in the core.

In bulk $EuTiO_3$, the establishment of a FM ground state, instead of an AFM one, is believed to be due to a delicate balance between the different exchange interactions among Eu^{2+} magnetic moments in the system: i) Direct FM exchange between Eu^{2+}, which is very weak due to the almost null overlap between Eu-*4f* states; ii) an AFM super-exchange interaction mediated by O-*2p* states: iii) an AFM super-exchange interaction mediated by Ti-*3d* states; iv) a carriers mediated Ruderman-Kittel-Kasuya-Yoshida (RKKY)-like indirect FM-exchange, proposed for La-doped FM ETO films [18], due to an overlap between (filled) t_{2g} Ti-*3d* states and Eu *4f*-orbitals; and v) an indirect exchange interaction via Eu-*5d* t_{2g} states, which play an important role in Eu-chalcogenides (e.g.

EuO). It has been proposed that the filling of the Ti-*3d* bands reverts the indirect exchange via the Eu-*5d* t_{2g} states from AFM to FM through the coupling between t_{2g} Eu-*5d* and Ti-*3d* electrons [43, 44]. Our experimental XMCD data confirm that the super-exchange between Eu^{2+} magnetic moments through O-*2p* and Ti-*3d* states is negative, thus the only two mechanisms which could effectively give rise to ferromagnetism are FM-couplings mediated by itinerant carriers (without any role of Eu-*5d* states) or mediated by Eu-*5d* hybridized with Ti-*3d* states [44].

In order to verify if the latter can effectively play a role in our heterostructures, in Fig. 7a we show the average spin-resolved LDOS of the ETO layers in the FM ground state. The calculations are compared to the LDOS in the AFM configuration (Fig.7b). We find that Eu-*5d* states, while in general characterized by a much weaker spectral weight than the O-*2p* and Ti-*3d* contributions, have a strong overlap with Ti-*3d* t_{2g} bands in the FM ground state close and above the Fermi level. Furthermore, there is also a substantial overlap with the Eu-*4f* state around -2 eV, where these states also show a clear spin-polarization. On the other hand, in the AFM solution the Eu-*5d* states are at higher energy, have a lower spectral weight compared to the FM-case, and their overlap with Ti-*3d* states is substantially reduced. These results suggest that the FM-ordering of Eu^{2+} is mostly due to a FM interaction mediated by Eu-*5d*/Ti-*3d* hybridized states as suggested earlier [44], although it is not possible to fully exclude a role of a carrier mediated RKKY- FM interaction [18].

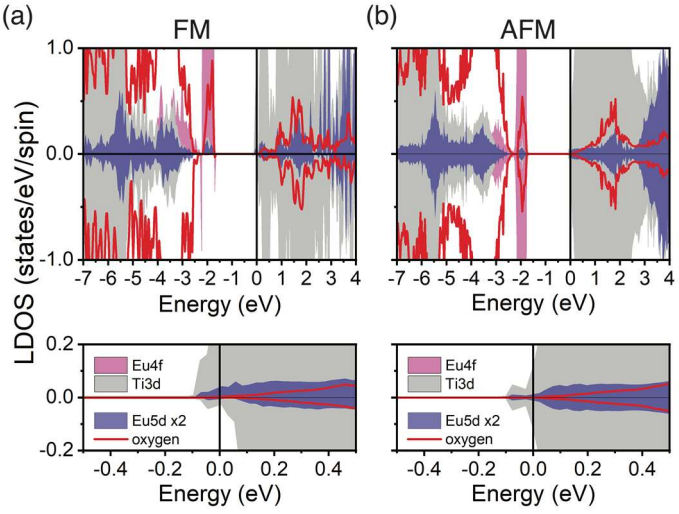

Fig. 7. Comparison between AFM and FM solutions of the model: (a)-(b) Element and spin-resolved density of states from the DFT+*U* calculations for $EuTiO_3$ layers (average) with (a) FM and (b) AFM coupling. In the FM solution we do observe a substantial spin-polarization at -2 eV of both Eu-*4f* (magenta) and Eu-*5d* (blue) states, and an overlap between Ti-*3d* states (grey) and Eu-*5d* states near and above the Fermi level, absent in the AFM case.

Very interestingly the calculations also demonstrate that the filling of Ti-$3d_{xz,yz}$ bands and FM-order appear at the same time, as shown in Fig.6b. Therefore, Ti-$3d_{xz,yz}$ electrons have the main role in the establishing a FM-coupling among Eu^{2+} magnetic moments in the confined heterostructure, while $3d_{xy}$ electrons seems less effective in mediating a dominant FM interaction in this system.

Conclusions

In conclusion, in this work we combined different experimental methods and theoretical calculations to analyze and clarify the origin and properties of the spin-polarized q2DEG at the LAO/ETO/STO oxide interface. The DFT+*U* calculations show that a FM and spin-polarized q2DEG is formed at the (001) LAO/ETO/STO heterostructure in a defect-free interfaces. At the same time, theory explains some crucial properties of this q2DEG revealed by x-ray spectroscopy and electrical transport results. In particular, it is shown why the filling of $3d_{xz,yz}$ bands, inferred from the experimental results, is simultaneous to the transition to a FM state, thus explaining why the q2DEG is spin-polarized only above the Lifshitz transition. Moreover, spin-polarized $3d_{xz,yz}$ electrons created at the LAO/ETO interface leak also into the first layers of STO, explaining the contribution from STO to the Ti-*3d* magnetic moment found in previous investigations [12].

Our results show that the LAO/ETO/STO system provides a platform for the study of novel quantum phenomena where superconductivity, magnetism and spin-orbit coupling are fully entangled, and is a clear example on how new functional properties can be created in oxide 2D-systems by atomic interface engineering.

More generally, the combination of electrical transport and spectroscopy measurements with band structure calculations reported in this work is a powerful tool to obtain a deeper understanding of complex heterostructures characterized by unexpected novel functional properties. Such a combined approach is becoming essential to gain detailed understanding of novel heterostructures showing exceptional properties.

Materials and Methods

LAO(n)/ETO(2)/STO(001) heterostructures were fabricated by pulsed laser deposition (PLD) assisted by Reflection High Energy Electron Diffraction (RHEED) from sintered $Eu_2Ti_2O_7$ and crystalline LAO targets onto TiO_2-terminated (001) STO substrates. The samples were deposited at a temperature of 700 °C in a background O_2 pressure of 8×10^{-5} mbar and cooled down in the same conditions to room temperature with a rate of 5°C/min. We used an excimer laser (Lambda Physics, 248 nm wavelength) and 1.3 J/cm^2

fluence, 1Hz of repetition, resulting in a rate of 0.05 unit cell/pulse (20 pulses for each unit cells). A q2DEG is formed when n> 4 unit-cells (uc).

We have used polarization dependent x-ray absorption spectroscopy (XAS) across the Eu $M_{4,5}$ and the Ti-$L_{2,3}$ edge to probe directly the magnetic and orbital properties of Eu and Ti at the interface. The experiments were performed at the beamline X-Treme of the Swiss Light Source [23]. XAS performed with circularly or linearly polarized photons can detect the magnetic moments and the *3d* orbital energy splitting, respectively. The two techniques, usually known as x-ray magnetic circular dichroism (XMCD) and x-ray linear dichroism (XLD) are so sensitive that they can be used on single interfaces. The Eu $M_{4,5}$ edge and the Ti $L_{2,3}$ XMCD spectra were obtained as difference between the average of 8 and 16 (respectively) XAS spectra acquired with magnetic field parallel and antiparallel to the photon-helicity vector orientations. The 16 and 32 XAS data needed for each XMCD were collected in a sequence alternating reversal of field and polarization at each spectrum. This procedure ensures the best cancellation of spurious effects. The magnetic field dependent magnetization loops, as those shown in Fig.1, were obtained by measuring, at each field, the difference between the TEY intensity at the M_5-Eu edge peak, normalized by the intensity below the absorption edge, obtained with two different helicities (combination with polarization and field direction).

SQUID data were collected by using a Quantum Design MPMS3. Magnetization measurements as a function of magnetic field were acquired on both LAO/ETO//STO heterostructure and bare STO substrates that suffered the same heating process mimicking the LAO/ETO growth process to confirm and exclude the absence of ferromagnetic impurities stemming from the substrate itself. Data were corrected for the diamagnetism of the substrate substrating the linear contribution acquired at high magnetic fields.

RESPES Measurements were carried out at a pressure of 5×10^{-10} mbar and at base temperature of ≈ 12 K (above the FM Tc) on LAO(5)/ETO(2uc)/STO samples. This technique, employing soft-energy x-rays resonant with the absorption of the relevant ions in the system, enables access to buried systems, and it is, therefore, suitable for the investigation of the q2DEG at the LAO/ETO/STO interface. To reduce any influence of contaminants and to preserve as much as possible the surface of the ex-situ grown samples, they were transferred, just after the deposition, into a sample-carrier vessel filled by inert Ar-gas. However, an exposure (limited in time) to ambient atmosphere was unavoidable for the sample mounting into the experimental station. During the measurements we moved the beam position around the region investigated in order to

avoid variations of the surface and interfacial oxygen by photon irradiation, to which LAO/STO samples of certain preparation protocols have demonstrated some sensitivity at low temperature [28]. As matter of fact, by raster scanning the beam on the sample, we did not detect any buildup of the Ti^{3+} spectral weight in the core level x-ray photoemission (XPS) and XAS spectra, nor in the valence band (VB).

DFT+*U* calculations were performed with the Vienna *ab initio* simulation package (VASP) (39, 40) [37][38] with the projector augmented wave (PAW) basis [39][40]. The ionic positions were fully relaxed until the forces were less than 0.001 eV/Å. The generalized gradient approximation was used for the exchange correlation functional in the implementation of Perdew, Burke and Ernzerhof [41] and an on-site effective Hubbard parameter [42], *U* = 4 eV, 7.5 eV and 8 eV were applied on the Ti-*3d*, Eu-*4f* and *La-4f* states, respectively. Analogous to the ETO (001) surface state [12], the choice of *U* for the Eu-*4f* states, and partially for the Ti-*3d* states, is dictated by the need to reproduce the position of the experimental Eu^{2+} peak in the valence band at ~2eV. In general, lower values of *U* for Eu-*4f* only shift the position of the Eu-*4f* band to energies closer to the Fermi level. The results shown here for *U*=4 eV for the Ti-*3d* states give the best agreement with the experimental data, and in particular concerning the position of Eu-*4f* band. Calculations with *U* ranging from 1 eV to 4.5 eV show the main conclusions are not dependent on the choice of *U* for Ti-3*d* states. Further results from the calculations are shown in the Supplementary Materials, from page 24.

References

[1] A. Ohtomo, H.Y. Hwang, A high-mobility electron gas at the $LaAlO_3/SrTiO_3$ heterointerface, Nature 427, 423-426 (2004).

[2] S. Thiel, G. Hammerl, A. Schmehl, C.W. Schneider, and J. Mannhart, Tunable quasi–two-dimensional electron gases in oxide heterostructures, Science 313, 1942–1946 (2006).

[3] A.D. Caviglia, M. Gabay, S. Gariglio, N. Reyren, C. Cancellieri, J.-M. Triscone, Tunable Rashba Spin-Orbit Interaction at Oxide Interfaces, Phys. Rev. Lett. 104, 126803 1-4 (2010).

[4] D. Stornaiuolo, S. Gariglio, A. Fête, M. Gabay, D. Li, D. Massarotti, J.-M. Triscone, Weak localization and spin-orbit interaction in side-gate field effect devices at the $LaAlO_3/SrTiO_3$ interface, Phys. Rev. B 90, 235426 1-5 (2014).

[5] A.D. Caviglia, S. Gariglio, N. Reyren, D. Jaccard, T. Schneider, M. Gabay, S. Thiel,G. Hammerl, J. Mannhart, J.-M. Triscone, Electric field control of the $LaAlO_3/SrTiO_3$ interface ground state, Nature 456, 624–627 (2008).

[6] C. Richter, H. Boschker, W. Dietsche, E. Fillis-Tsirakis, R. Jany, F. Loder, L.F. Kourkoutis, D.A. Muller, J.R. Kirtley, C.W. Schneider, J. Mannhart, Interface superconductor with gap behaviour like a high-temperature superconductor, Nature 502, 528-531 (2013).

[7] D. Stornaiuolo, D. Massarotti, R. Di Capua, P. Lucignano, G.P. Pepe, M. Salluzzo, F. Tafuri, Signatures of unconventional superconductivity in the $LaAlO_3/SrTiO_3$ two-dimensional system, Phys. Rev. B 95, 140502(R) 1-5 (2017).

[8] A. Brinkman, M. Huijben, M. van Zalk, J. Huijben, U. Zeitler, J.C. Maan, W.G.van der Wiel, G. Rijnders, D.H.A. Blank, H. Hilgenkamp, Magnetic effects at the interface between non-magnetic oxides, Nature Mater. 6, 493–496 (2007).

[9] E. Lesne, Y. Fu, S. Oyarzun, J.C. Rojas-Sánchez, D.C. Vaz, H. Naganuma, G. Sicoli, J. -P. Attané, M. Jamet, E. Jacquet, , J. -M. George, A. Barthélémy, H. Jaffrès, A. Fert, M. Bibes, L. Vila, Highly efficient and tunable spin-to-charge conversion through Rashba coupling at oxide interfaces. Nature Mater. 15, 1261–1266 (2016).

[10] M. Salluzzo, S. Gariglio, D. Stornaiuolo, V. Sessi, S. Rusponi, C. Piamonteze, G. M. De Luca, M. Minola, D. Marrè, A. Gadaleta, H. Brune, F. Nolting, N. B. Brookes, and G. Ghiringhelli, Origin of Interface Magnetism in $BiMnO_3/SrTiO_3$ and $LaAlO_3/SrTiO_3$ Heterostructures, Phys. Rev. Lett. 111, 087204 (2013).

[11] G. M. De Luca, R. Di Capua, E. Di Gennaro, F. Miletto Granozio, D. Stornaiuolo, M. Salluzzo, A. Gadaleta, I. Pallecchi, D. Marrè, C. Piamonteze, M. Radovic, Z. Ristic, S. Rusponi, Transport properties of a quasi-two-dimensional electron system formed in $LaAlO_3/EuTiO_3/SrTiO_3$ heterostructures, Phys. Rev. B 89, 224413 1-6 (2014).

[12] D. Stornaiuolo, C. Cantoni, G.M. De Luca, R. Di Capua, E. Di. Gennaro, G. Ghiringhelli, B. Jouault, D. Marrè, D. Massarotti, F. Miletto Granozio, I. Pallecchi, C. Piamonteze, S. Rusponi, F. Tafuri, M. Salluzzo, Tunable spin polarization and superconductivity in engineered oxide interfaces , Nat. Mater. 15, 278-284 (2016).

[13] H. R. Zhang, Y. Zhang, H. Zhang, J. Zhang, X. Shen, X. X. Guan, Y. Z. Chen, R. C. Yu, N. Pryds, Y. S. Chen, B. G. Shen, and J. R. Sun, Magnetic two-dimensional electron gas at the manganite-buffered $LaAlO_3/SrTiO_3$ interface, Phys. Rev. B 96, 195167 1-7 (2017).

[14] P. Moetakef, J. Y. Zhang, A. Kozhanov, B. Jalan, R. Seshadri, S. J. Allen, and S. Stemmer, Electrostatic carrier doping of $GdTiO_3/SrTiO_3$ interfaces, Appl. Phys. Lett.

98, 112110 1-4 (2011).

[15] F. Gunkel, C. Bell, H. Inoue, B. Kim, A. G. Swartz, T. A. Merz, Y. Hikita, S. Harashima, H. K. Sato, M. Minohara, S. Hoffmann-Eifert, R. Dittmann, and H. Y. Hwang, Defect-control of conventional and anomalous electron transport at complex oxide interfaces, Phys. Rev. X 6, 031035 1-15 (2016).

[16] K. J. Kormondy, L. Gao, X. Li, S. Lu, A. B. Posadas, S. Shen, M. Tsoi, M. R. McCartney, D. J. Smith, J. Zhou, L. L. Lev, M.-A. Husanu, V. N. Strocov, and A. A. Demkov, Large positive linear magnetoresistance in the two-dimensional t 2g electron gas at the EuO/$SrTiO_3$ interface, Sci. Rep. 8, 1-9 (2018).

[17] Y. Gan, D. V. Christensen, Y. Zhang, H. Zhang, D. Krishnan, Z. Zhong, W. Niu, D. J. Carrad, K. Norrman, M. von Soosten, T. S. Jespersen, B. Shen, N. Gauquelin, J. Verbeeck, J. Sun, N. Pryds, and Y. Chen, Diluted Oxide Interfaces with Tunable Ground States, Adv. Mater. 31, 1805970 1-9 (2019).

[18] T. Katsufuji, Y. Tokura, Transport and magnetic properties of a ferromagnetic metal: $Eu_{1-x}R_xTiO_3$, Phys. Rev. B 60, R15021- R15023 (1999).

[19] K. S. Takahashi, M. Onoda, M. Kawasaki, N. Nagaosa, and Y. Tokura, Control of the Anomalous Hall Effect by Doping in $Eu_{1-x}La_xTiO_3$ Thin Films, Phys. Rev. Lett. 103, 057204 (2009).

[20] K. S. Takahashi, H. Ishizuka, T. Murata, Q. Y. Wang, Y. Tokura, N. Nagaosa, and M. Kawasaki, Anomalous Hall effect derived from multiple Weyl nodes in high-mobility $EuTiO_3$ films, Science Advances 4, eaar7880 1-8 (2018).

[21] K. Ahadi, Z. Gui, Z. Porter, J. W. Lynn, Z. Xu, S. D. Wilson, A. Janotti, and S. Stemmer, Carrier density control of magnetism and Berry phases in doped $EuTiO_3$, APL Materials 6, 056105 1-7 (2018).

[22] J. H. Lee, L. Fang, E. Vlahos, X.Ke, Y.W. Jung, L. F.Kourkoutis, J.-W. Kim, P. J. Ryan, T. Heeg, M. Roeckerath, V. Goian, M. Bernhagen, R. Uecker, P. C. Hammel, K. M. Rabe, S. Kambal, J. Schubert, J.W. Freeland, D. A. Muller, C. J. Fennie, P. Schiffer, V. Gopalan, E. Johnston-Halperin, D.G. Schlom, A strong ferroelectric ferromagnet created by means of spin-lattice coupling, Nature 466, 954-958 (2010).

[23] C. Piamonteze, U. Flechsig, S. Rusponi, J. Dreiser, J. Heidler, M. Schmidt, R. Wetter, M. Calvi, T. Schmidt, H. Pruchova, J. Krempasky, C. Quitmann, H. Brune, and F. Nolting, X-Treme beamline at SLS: X-ray magnetic circular and linear dichroism at high field and low temperature, J. Synchrotron Radiat. 19, 661 (2012).

[24] Eli Stavitski and Frank M.F. de Groot, The CTM4XAS program for EELS and XAS spectral shape analysis of transition metal L edges, Micron 41 687–694 (2010).

[25] Cinthia Piamonteze, Piter Miedema and Frank M. F. de Groot, Accuracy of the spin sum rule in XMCD for the transition-metal L edges from manganese to copper, Phys. Rev. B 81, 214422 (2009).

[26] N. Nagaosa, J. Sinova, S. Onoda, A. H. MacDonald, and N. P. Ong, Anomalous Hall effect, Rev. Mod. Phys. 82, 1539-1592 (2010).

[27] V. N. Strocov, T. Schmitt, U. Flechsig, T. Schmidt, A. Imhof, Q. Chen, J. Raabe, R. Betemps, D. Zimoch, J. Krempasky, X. Wang, M. Grioni, A. Piazzalunga, L. Patthey, High-resolution soft X-ray beamline ADRESS at the Swiss Light Source for resonant inelastic X-ray scattering and angle-resolved photoelectron spectroscopies, J. Synchrotron Rad. 17, 631-643 (2010).

[28] A. Chikina, F. Lechermann, M.-A. Husanu, M. Caputo, C. Cancellieri, X. Wang, T. Schmitt, M. Radovic & V. N. Strocov. Orbital ordering of the mobile and localized electrons at oxygen-deficient $LaAlO_3/SrTiO_3$ interfaces, ACS Nano 12 7927 (2018).

[29] M. Haverkort, Z. Hu, A. Tanaka, G. Ghiringhelli, H. Roth, M. Cwik, T. Lorenz, C. Schüßler-Langeheine, S. Streltsov, A. Mylnikova, V. Anisimov, C. de Nadai, N. Brookes, H. Hsieh, H. J. Lin, C. Chen, T. Mizokawa, Y. Taguchi, Y. Tokura, D. Khomskii, and L. Tjeng, Determination of the Orbital Moment and Crystal-Field Splitting in $LaTiO_3$, Phys. Rev. Lett. 94, 056401 1-4 (2005).

[30] N. C. Plumb, M. Salluzzo, E. Razzoli, M. Månsson, M. Falub, J. Krempasky, C. E. Matt, J. Chang, M. Schulte, J. Braun, H. Ebert, J. Minár, B. Delley, K. J. Zhou, T. Schmitt, M. Shi, J. Mesot, L. Patthey, and M. Radović, Mixed dimensionality of confined conducting electrons in the surface region of $SrTiO_3$, Phys. Rev. Lett. 113, 086801 1-5 (2014).

[31] Z. Wang, S. McKeown Walker, A. Tamai, Y. Wang, Z. Ristic, F. Y. Bruno, A. de la Torre, S. Riccò, N. C. Plumb, M. Shi, P. Hlawenka, J. Sanchez-Barriga, A. Varykhalov, T. K. Kim, M. Hoesch, P. D. C. King, W. Meevasana, U. Diebold, J. Mesot, B. Moritz, T. P. Devereaux, M. Radović, and F. Baumberger, Tailoring the nature and strength of electron–phonon interactions in the $SrTiO_3$(001) 2D electron liquid, Nature Mater. 15, 835-840 (2016).

[32] G. Berner, M. Sing, H. Fujiwara, A. Yasui, Y. Saitoh, A. Yamasaki, Y. Nishitani, A. Sekiyama, N. Pavlenko, T. Kopp, C. Richter, J. Mannhart, S. Suga, and R. Claessen, Direct k-Space Mapping of the Electronic Structure in an Oxide-Oxide Interface, Phys. Rev. Lett. 110, 247601 1-5 (2013).

[33] C. Cancellieri, M. L. Reinle-Schmitt, M. Kobayashi, V. N. Strokov, P. R. Wilmott, Wilmott, D. Fontaine, A. Fontaine, P. Ghosez, A. Filippetti, P. Delugas, and V.

Fiorentini, Doping-dependent band structure of $LaAlO_3/SrTiO_3$ interfaces by soft x-ray polarization-controlled resonant angle-resolved photoemission, Phys. Rev. B 89, 121412 (R) 1-6 (2014).

[34] C. Cancellieri, A. S. Mishchenko, U. Aschauer, A. Filippetti, C. Faber, O. S. Barišić, V. A. Rogalev, T. Schmitt, N. Nagaosa, and V. N. Strocov, Polaronic metal state at the $LaAlO_3/SrTiO_3$ interface, Nature Commun. 7, 10386 1-7 (2016).

[35] R. Di Capua, M. Radovic, N. C. Plumb, J. H. Dil, Z. Ristic, E. B. Guedes, G. M. De Luca, Z. Wang, M. Verma, A. P. Weber, R. Pentcheva, M. Salluzzo, A two-dimensional electron gas at the (001) surface of ferromagnetic $EuTiO_3$, arXiv:2003.05494 [cond-mat.mtrl-sci]

[36] P. Zhang, P. Richard, T. Qian, Y. M. Xu, X. Dai, and H. Ding, A precise method for visualizing dispersive features in image plots, Rev. Sci. Instrum. 82, 043712 (2011).

[37] G. Kresse and J. Hafner, *Ab initio* molecular dynamics for liquid metals, Phys. Rev. B 47, 558-561 (1993).

[38] G. Kresse and J. Furthmüller, Efficiency of ab-initio total energy calculations for metals and semiconductors using a plane-wave basis set, Comput. Mater. Sci. 6, 15-50 (1996).

[39] P. E. Blöchl, Projector augmented-wave method, Phys. Rev. B 50, 17953-17979 (1994).

[40] G. Kresse and D. Joubert, From ultrasoft pseudopotentials to the projector augmented-wave method, Phys. Rev. B 59, 1758-1775 (1999).

[41] J. P. Perdew, K. Burke, and M. Ernzerhof, Generalized Gradient Approximation Made Simple, Phys. Rev. Lett. 77, 3865-3868 (1996).

[42] S. L. Dudarev, G. A. Botton, S. Y. Savrasov, C. J. Humphreys, and A. P. Sutton, Electron-energy-loss spectra and the structural stability of nickel oxide: An LSDA+U study, Phys. Rev. B 57, 1505-1509 (1998).

[43] H. Akamatsu, Y. Kumagai, F. Oba, K. Fujita, H. Murakami, K. Tanaka, and I. Tanaka, Antiferromagnetic superexchange via 3d states of titanium in $EuTiO_3$ as seen from hybrid Hartree-Fock density functional calculations, Phys. Rev. B 83, 214421 1-6 (2011).

[44] Z. Gui and A. Janotti, Carrier-Density-Induced Ferromagnetism in $EuTiO_3$ Bulk and Heterostructures, Phys. Rev. Lett. 123, 127201 1-6 (2019).

Acknowledgements

The Authors acknowledge funding from ERA-NET QUANTERA European Union's Horizon H2020 project QUANTOX under Grant Agreement No. 731473, Ministero dell'Istruzione, dell'Università e della Ricerca (MIUR) for the PRIN project TOP-SPIN (Grant No. PRIN 20177SL7HC) and for the PRIN 2010-11 project (Grant No. PRIN 2010-11–OXIDE), the EU COST program CA16218 (Nanocohybri), the German Research Foundation (DFG) within CRC/TRR80 (project number 107745057, subproject C3), CRC1242 (project number 278162697, subproject C02), and Computation time at the Leibniz Rechenzentrum Garching, project pr87ro and supercomputer magnitUDE (DFG grants INST 20876/209-1 FUGG, INST 20876/243-1 FUGG).

Author contributions:

Conceptualization: RDC, DS, GG, MS

Methodology: -

Sample preparation: AS, EDG, FMG, YC, MS

Transport measurements and Analysis: BJ, DS, YC, MDA

RESPES Experiment and Analysis: RDC, VNS, MS, MR, EG, EDG, FMG

ARPES Experiment: MR, GMDL, RDC, BG, NP, MS

XMCD Experiment: and Analysis: CP, MS, GG, GMDL, DP

SQUID Experiment: DP

DFT+U Calculations: MV, RP

Supervision: MS, RDC

Writing: MS, RDC, DS

Writing-review & editing: all the Authors participated to the editing of the paper

Supplementary Materials

1. Details of XAS and XMCD analysis and supplementary data.

1.1 X-ray Absorption Spectroscopy and X-ray magnetic linear and circular dichroism experiment

X-ray Absorption spectra have been acquired using Total Electron Yield (TEY) method. The x-ray magnetic circular dichroism technique allows determining the projection of the magnetic moment associated to a specific ion in the structure along the photon beam direction. The circular polarization of the light carries a moment, which is transferred to the absorbing atom. Selection rules imply different XAS spectra for the two opposite (left and right) circular polarizations if the absorbing ion is characterized by a magnetic moment component along the beam direction.

In the TEY mode we measure a current that is proportional to the photo and Auger electrons created by the photo-absorption process. However, only the photo and Auger electrons created within the electron escape depth reach the surface after elastic and inelastic collisions. Overall, neutrality requires a current of electrons going from the ground to the sample. By measuring this current, we get a measure of the electrons leaving the samples. The electron escape depth is few nm's, and in the particular case of absorption from Ti-L_{23} edge, it is of the order of 1-2 nm.

In the case of transition metal oxides and for soft x-ray absorption processes,i.e. 2p->3d transition, sum rules can be applied to get a quantitative estimate of the effective spin (m_{Espin}) and orbital components (m_{orb}) of the magnetic moment. However, as discussed in details in ref.(25) of the main text, the application of the sum rules is powerful but needs some care in particular for light transition metals, like titanium.

The Equations to be used are the following (S1):

$$m_{Espin} = -\frac{6\int_{L_3}\left(I^+ - I^-\right)dE - 4\int_{L_3+L_2}\left(I^+ - I^-\right)dE}{\int_{L_3+L_2}\left(I^+ + I^-\right)dE}\left(10 - n_{3d}\right) \qquad \text{(eq. S1a)}$$

$$m_{orb} = -\frac{4}{3}\frac{\int_{L_3+L_2}\left(I^+ - I^-\right)dE}{\int_{L_3+L_2}\left(I^+ + I^-\right)dE}\left(10 - n_{3d}\right) \qquad \text{(eq. S1b)}$$

where I^+ and I^- are the XAS spectra acquired with the two circular polarizations, the magnetic dichroism is XMCD=I^+-I^-, and n_{3d} is the 3d electronic density. To evaluate eq. S1a it is necessary to separate the L_3 and L_2 edges in the experimental spectrum and calculate the following integrals:

$$q = \int_{L_3} \left(I^+ - I^- \right) dE$$

$$p = \int_{L_3+L_2} \left(I^+ - I^- \right) dE$$

However, the L_3 and L_2 contributions are mixed in the Ti XAS spectra, and it is not possible to establish a reliable procedure to separate them. Thus, the evaluation of the spin moment at Ti-edge is affected by an unknown error.

On the other hand, the orbital moment can be calculated safely, since there is no need to separate the integrals at the L_2 and L_3 edges and the relationship relating the orbital moment to the XMCD is exact.

1.2 X-ray Multiple scattering calculations and charge transfer

Simulations including charge transfer effects were done using charge transfer ligand field multiplet theory, implemented in the CTM4XAS software (24). The charge transfer is included in an Anderson impurity type of model where two parameters are necessary to describe the system: the energy difference between the Ti-*3d* and the ligand band (called Δ here) and the transfer integral which describes the overlap between metal and ligand bands and therefore gives the probability for the electron to be transferred. The Δ fitting the XAS data is 4 eV. The transfer integrals used were 2 and 1 for b_1, a_1 (d_{x2-y2}, d_{z2}) and b_2,e (d_{xy}, d_{xz}/d_{yz}) orbitals, respectively. This choice is commonly used for octahedral or close to octahedral systems and the reasoning behind is that the probability for electron transfer is higher (in this case two times higher) for orbitals pointing in the bond direction, as d_{x2-y2}, d_{z2}. We used U_{pd}-U_{dd}=2eV. The crystal field parameters were $10D_q$=2.3, D_s=-0.02, D_t=-0.002. A slightly larger value of $10D_q$ compared to the simulation for LAO/STO seems to fit better the energy difference between the double peaks at L_3 and L_2 edges. The Slater Integrals were reduced by 90% applied on the corrected Hartree-Fock values. This simulation gives a number of 3d holes equals to 9.65. The broadening used were 0.1 eV for the Gaussian broadening, to account for the energy resolution, and different Lorentzian broadening for each of the 4 peaks of the spectrum, namely half width at half maximum of 0.11 eV, 0.34 eV, 0.5 eV, and 0.65 eV for the four XAS peaks (from the first to the last).

Fig. S1 shows the comparison of the simulation with LAO/ETO/STO XAS data. The XAS data agreement is very good, except for the features around 470 eV and 475 eV.

In Fig. S2 we also show simulation for titanium in a Ti^{3+} configuration in D4h symmetry, which resemble the shape of the Constant Initial State (CIS) spectra obtained

by integrating the valence band RESPES results shown in Fig.3 of the manuscript. We used the same crystal field splitting parameters employed for Ti^{4+} spectra and CT parameters The charge transfer has the effect of increasing the valleys between the peaks. Δ =4 eV and U_{pd}-U_{dd}=2eV. In the simulations shown below we have also plotted different simulated spectra as function of the 10Dq value from 1.0 eV to 2.2 eV.

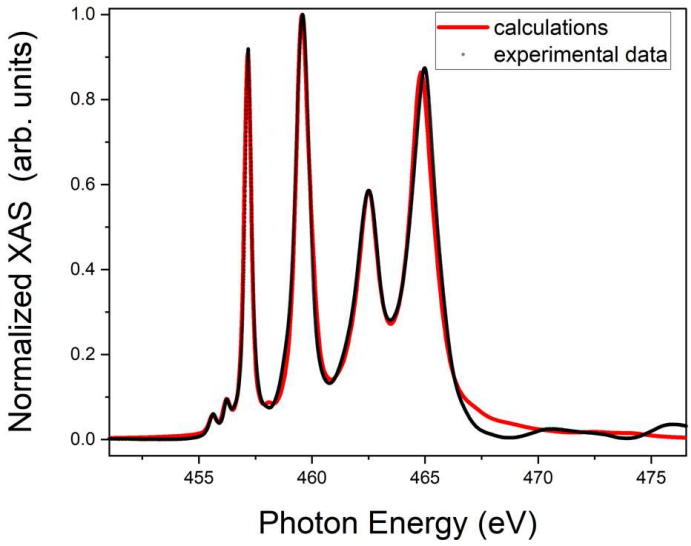

Fig. S1: Typical TEY Ti-$L_{2,3}$ edge XAS spectrum on LAO/ETO/STO system in C+ polarization (black circles) and atomic multiplet atomic splitting simulation (red line).

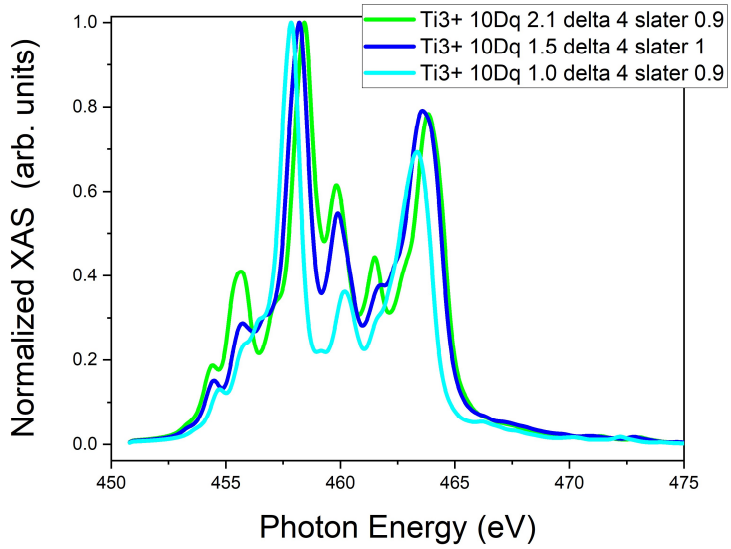

Fig. S2: Atomic multiplet splitting simulation assuming Ti^{3+} valence state with varying crystal field (10 Dq) and CT parameters.

S2. Tight binding fit of the band dispersion

The band-dispersion profiles were analyzed by combining the spectra acquired with different polarizations, and by fitting the Momentum Dispersion Curves (MDC) as function of the energy relative to the Fermi level E_F. Finally, the band profiles were compared to the two-dimensional(2D) curvature maps of the raw data (31), as further validation of the fitting process for the band identification.

Circular polarization (C+) *E vs.* k_x band dispersions include features associated to all the bands in the system, namely bands with $3d_{xz}$, $3d_{yz}$ and $3d_{xy}$ orbital characters; dataset recorded in *p-pol* configuration are mainly affected by the $3d_{xz}$ band, while *s-pol* configuration provides information about the $3d_{xy}$ and the $3d_{yz}$ bands. (d_{xy} indicates the light band, while d_{xz} and d_{yz} refer to the heavy bands along the short and the long diameters of the ellipse, respectively).

We assumed for simplicity three independent two-dimensional bands as described by eqs. S2:

$$E_{xy}(k_x, k_y) - E_F = 2V_{xy}(2 - cosk_x a_0 - cosk_y a_0) + E_{0xy} \quad \text{(eq. S2a)}$$

$$E_{xz}(k_x, k_y) - E_F = 2V_{xz}(1 - cosk_x a_0) + 2V_{yz}(1 - cosk_y a_0) + E_{0xz} \quad \text{(eq. S2b)}$$

$$E_{xz}(k_x, k_y) - E_F = 2V_{yz}(1 - cosk_x a_0) + 2V_{xz}(1 - cosk_y a_0) + E_{0yz} \quad \text{(eq. S2c)}$$

where a_0 is the lattice constant V_{xy}, V_{xz}, V_{yz} are the hopping parameters or so-called inner potentials, which determine the band-curvatures and the effective masses, E_F is the Fermi energy, and E_{0xy}, E_{0xz}, E_{0yz} are the $E - E_F$ value at k_x k_y = 0, i.e. the band bottom of each band (E_{0xz} *and* E_{0yz} are expected to have the same value inside the experimental error).

In our experimental configuration, recorded maps correspond to E vs. k_x curves at k_y = 0, so that eqs. (S2) read as:

$$E_{xy}(k_x) - E_F = 2V_{xy}(1 - cosk_x a_0) + E_{0xy} \quad \text{(eq. S3a)}$$

$$E_{xz}(k_x) - E_F = 2V_{xz}(1 - cosk_x a_0) + E_{0xz} \quad \text{(eq. S3b)}$$

$$E_{xy}(k_x) - E_F = 2V_{yz}(1 - cosk_x a_0) + E_{0yz} \quad \text{(eq. S3c)}$$

The experimental E vs. k_x datasets are obtained by deconvolving MDC intensity profiles of ARPES maps as superposition of Lorentzian contributions. The MDC profile corresponding to a given $\varepsilon = E - E_F$value is obtained by averaging ARPES intensity

values at each k_x over an energy window of 10 meV (centered on the chosen energy). At each given ε value, the central k_x of each Lorentzian contribution defines the (k_x, ε) point to be employed in the tight binding fitting procedure through eqs. (S3).

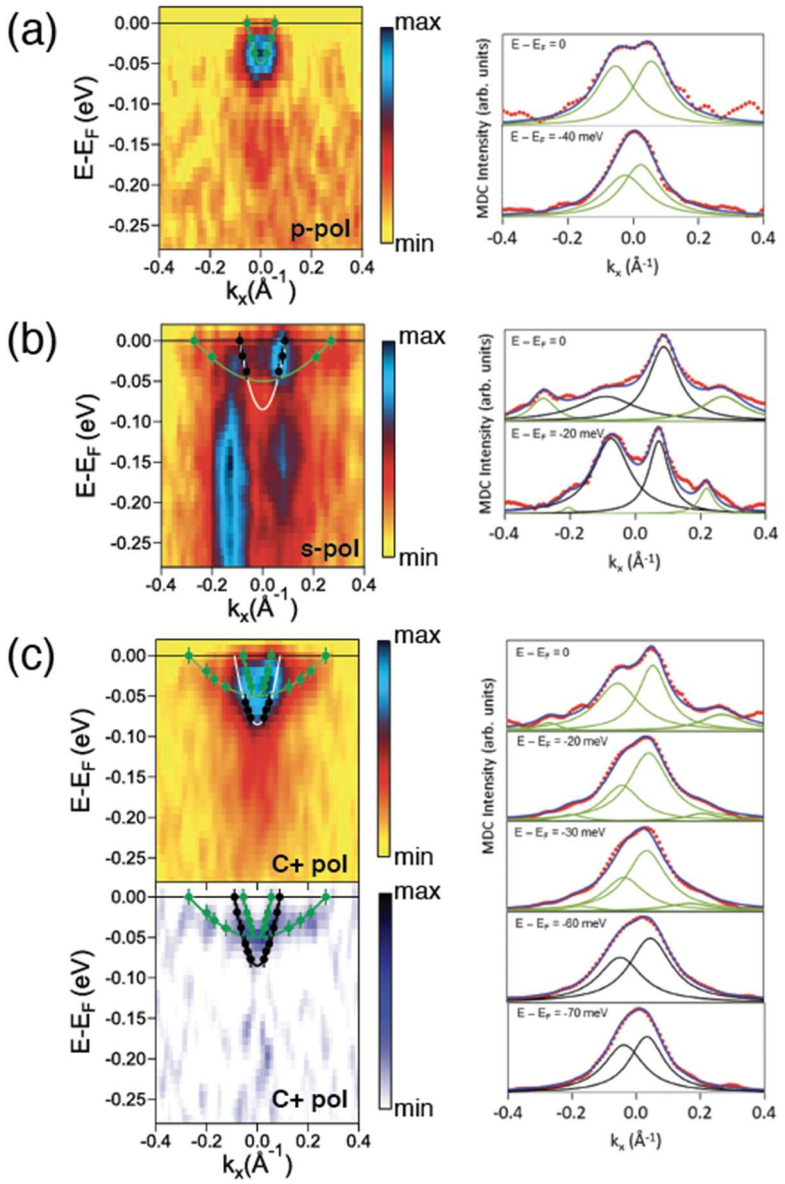

Fig. S3: Right panels: Band dispersion ARPES maps recorded with (a) p , (b) s , and (c) C+ polarizations of incident photons in the 2nd Bz. In panel (c) we show also the corresponding 2D curvature map of the C+ data. Left panels: some MDCs profiles at different binding energies (scatter data) extracted from each map and their Lorentzian deconvolutions as described in the text. The experimental points inferred from the deconvolution of the MDCs (black: d_{xy} "light" band; green: d_{xz} and d_{yz} "heavy" bands), as well as the tight binding best fit curves, are overlapped to the ARPES and curvature maps. Only points that could be clearly detected in the deconvolution and assigned were employed. The curves reported on different maps corresponding to the same band were estimated by a joint fit on all the points evaluated on the different maps.

The inferred (k_x, ε) points overlapped to ARPES maps (recorded at different polarizations of the incident photons) and to the 2D curvature map in C+ polarization, together with the band profiles as obtained from the fit procedure, are reported in Fig. S3. In the same figure, MDC profiles with their multiple Lorentzian fit are also shown; such Lorentzian deconvolutions provide the experimental points to be employed for the tight binding fit of the bands. For each experimental point, the error bar on the binding energy (vertical scale) is taken as the window of integration used to estimate the MDC curves (10 meV), while the error on the momentum (horizontal scale) is determined from the sensitivity of the corresponding Lorentzian deconvolution.

Finally, the error in the effective masses is determined by propagating the uncertainties associated to the estimation of the Fermi momentum and of the band bottoms of each band, as inferred from the tight binding fits.

In Table S1 we report all the parameters estimated from the fit.

Table S1: Fit parameters of the MDC data.

V_{xy} (eV)	V_{yz} (eV)	V_{xz} (eV)	E_{0xy} (meV)	E_{0xz}/E_{0yz} (meV)	$k_{F\,(xy)}$ (Å^{-1})	$k_{F\,(yz)}$ (Å^{-1})	$k_{F\,(xz)}$ (Å^{-1})
0.70±0.05	0.050±0.005	1.10±0.05	-85±5	-50±5	0.09±0.01	0.27±0.02	0.055±0.005

S3. Supplementary DFT+*U* calculations

In order to illustrate the role of the value of *U* for Ti-*3d* states we show in Fig. S4 a comparison between the band structure calculations in the ground state (FM) of (001) LAO/ETO/STO for Ti-*3d* values of *U*=2eV and *U*=4eV, using the same c(2x2) model described in the main text. One can see that the value of *U* of Ti-*3d* has an effect on the position of the Eu-*4f* peak, which shift to lower energy, around -1.6 eV for *U*=2eV, against the experimental value of -2 eV which is in very good agreement with the simulation done with *U*=4eV. Moreover, the *U*-value also has an effect on the band dispersions and on the FM splitting. The latter is sensibly smaller for *U*=2eV, still it is quite sizeable, thus a FM ground state is a very robust outcome of DFT+*U* calculations. Furthermore, the bottom of the lowest band, having a $3d_{xy}$ orbital character, is shifted to lower energy in the *U*=2eV case, and the $3d_{xz,yz}$ heavy band is shifted to higher energy. Both results give a splitting at Γ which is sensitively different from the experimental result (in both the FM and AFM (not shown) solution).

Thus, from the analysis of the effect of the Ti-*3d U* we conclude that a better agreement with the experimental results is obtained assuming *U*=4eV. On the other hand, the main result, i.e. the FM-ground state of the system, is independent on the choice of the *U*-value.

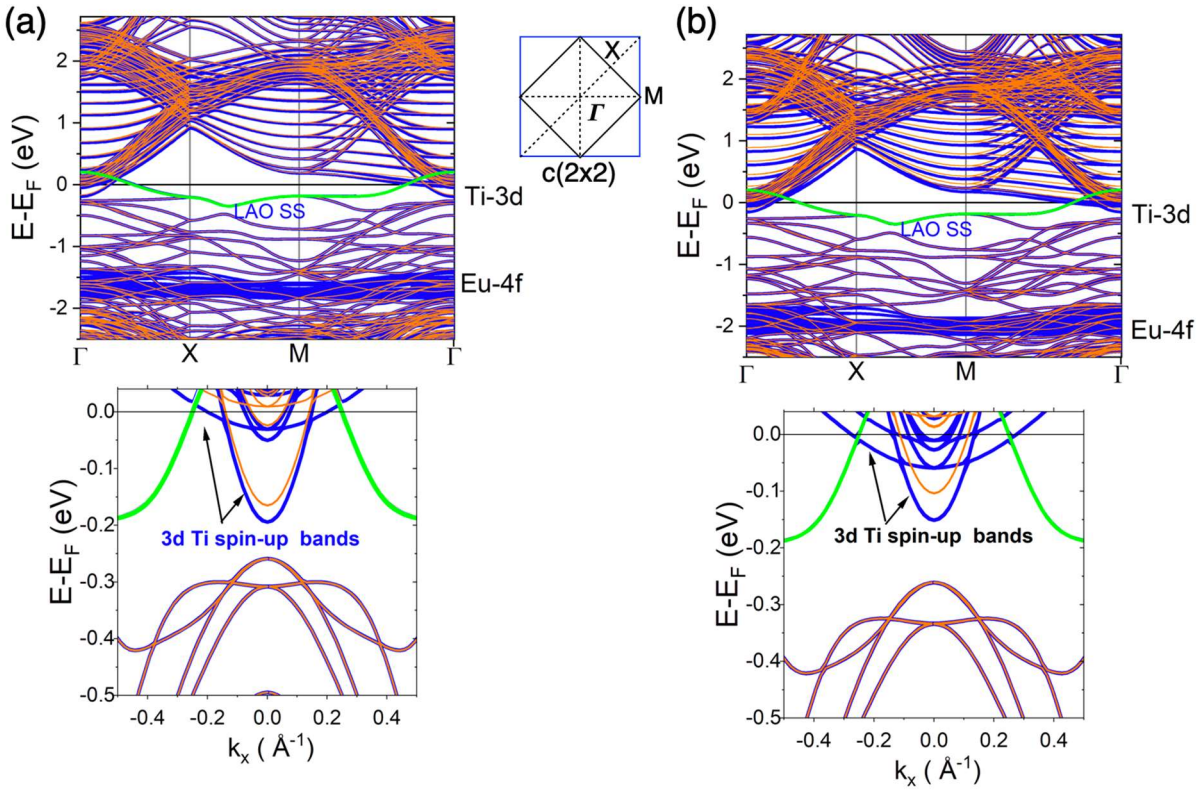

Fig. S4: Comparison between DFT+*U* calculations performed with Ti-*3d U* values of (a) 2eV and (b) 4eV.

ACKNOWLEDGEMENTS

It is a great pleasure for me to acknowledge and thank all the people who have accompanied, helped, supported and encouraged me during the past years.

First, I would like to express my deep and sincere gratitude to my supervisor, Prof. Daniela Stornaiuolo. Her patient guidance has steered my growth as a physicist. Her insight and technical expertise have been an invaluable help to my scientific steps in and out of the lab, not to mention her willingness to work together to overcome every my difficult.
Behind every successful Ph.D., there is an even greater Professor.

I would like to extend my gratitude to Dr Marco Salluzzo, for the interesting scientific discussions and for his rough but useful reproaches. I also wish to thank a former member of this team, Dr. Roberta Caruso. I owe a great deal to her, as her work has provided a solid ground for my scientific growth.
Furthermore I would like to thank Dr. Yu Chen for his continued kindness, friendliness and professionalism.

I want to thank Prof. Giampiero Pepe, Dr. Mikkel Ejrnaes, Prof. Loredana Parlato and Dr Daniela Salvoni to offer me the possibility to access the very interesting measurements at CNR of Pozzuoli.

I wish to extend my thanks also to the team of Prof. F. Tafuri, with special reference to Prof. D. Massarotti and my colleague and friend Halima G. Ahmad.

Moreover, I would like to enlarge my deepest gratitude to our Italian and international collaborators, for having given us the possibility to enrich and complete my work.

Many other people at University of Naples deserve my deepest gratitude for their valuable assistance and support to my Ph.D. I want to mention Felice, Roberta,

Martina, Alessandro, Luca, Mattia, Agostino, Luigi and Gianluca. A special thank to Mr Guido Celentano, for his constant and precise support for all the bureaucratic matters of my PhD and his friendliness.

Finally, I would like to express my gratitude to my loving boyfriend for every moments of last four years. Thank you for being by my side.

I want to thank from my heart my wonderful friends, who near or far have supported me.

Last but not least I must express my gratitude to my whole family that always stand by my side, to my mother for believing in me.

Acronyms

1S one side gate device.

2D Two-dimensional.

2DEG Two-dimensional electron gas.

2DES Two-dimensional electron gas system.

2S two pairs of side gate device.

a-LAO Amorphous-$LaAlO_3$.

AFM Antiferromagnet.

AHE Anomalous Hall Effect.

AMR Anisotropic magnetoresistance.

ARPES Angle-resolved photoemission spectroscopy.

BIA Bulk inversion asymmetry.

c-AFM Conductive atomic-force microscope.

CB conduction band.

DC direct current.

DFT Density Functional Theory.

DFT+U Density Functional Theory with on-site Hubbard terms.

EBL electron beam lithography.

FETs Semiconducting field effect transistors.

FM Ferromagnet.

FMR Ferromagnetic magnetic resonance.

He-FIB Helium Focused ion Beam.

HFI Hyperfine interaction.

ILP Iordanskii, Lyanda-Geller and Pikus model.

IR Infrared light.

JJs Josephson junctions.

LDOS Local density of states.

LED light emitting diode.

MESO Magneto-electric spin–orbit.

MF Maekawa-Fukuyama model.

MR Magnetoresistance.

PLD Pulsed laser deposition.

QPC Quantum point contact.

RESPES Resonant photoemission spectroscopy.

RHEED Reflection High Energy Electron Difraction.

SC Superconductivity.

SIA Structure inversion asymmetry.

SOC Spin-orbit coupling.

SQUIDs Superconducting quantum interference devices.

SSM Scanning SQUID microscopy.

TMOs Transition metal oxides.

UV Ultraviolet light.

VB valence band.

WAL Weak antilocalization.

WL Weak localization.

XAS X-ray absorption spectroscopy.

XMCD X-ray magnetic circular dichroism.

LIST OF FIGURES

FIGURE **Page**

BIBLIOGRAPHY

[1] Herbert Kroemer.
Nobel lecture: Quasielectric fields and band offsets: teaching electrons new tricks.
Rev. Mod. Phys., 73:783–793, Oct 2001.
doi: 10.1103/RevModPhys.73.783.

[2] Amit Dey and Sudhakar Yarlagadda.
Oxides: An answer to the qubit problem?
International Journal of Modern Physics B, 33(14):1930003, 2019.

[3] Yun-Yi Pai, Anthony Tylan-Tyler, Patrick Irvin, and Jeremy Levy.
Laalo _3/srtio _3: a tale of two magnetisms.
arXiv preprint arXiv:1610.00789, 2016.

[4] A Ohtomo and HY Hwang.
A high-mobility electron gas at the laalo 3/srtio 3 heterointerface.
Nature, 427(6973):423–426, 2004.

[5] Naoyuki Nakagawa, Harold Y Hwang, and David A Muller.
Why some interfaces cannot be sharp.
Nature materials, 5(3):204–209, 2006.

[6] Stefan Thiel, German Hammerl, Andreas Schmehl, Christof W Schneider, and Jochen Mannhart.
Tunable quasi-two-dimensional electron gases in oxide heterostructures.
Science, 313(5795):1942–1945, 2006.

[7] ML Reinle-Schmitt, C Cancellieri, Danfeng Li, Denis Fontaine, M Medarde, E Pomjakushina, CW Schneider, Stefano Gariglio, Ph Ghosez, J-M Triscone, et al.
Tunable conductivity threshold at polar oxide interfaces.
Nature communications, 3(1):1–6, 2012.

[8] Gervasi Herranz, Florencio Sánchez, Nico Dix, Mateusz Scigaj, and Josep Fontcuberta.
High mobility conduction at (110) and (111) laalo 3/srtio 3 interfaces.
Scientific reports, 2(1):1–5, 2012.

[9] Yunzhong Chen, Nini Pryds, Josée E Kleibeuker, Gertjan Koster, Jirong Sun, Eugen Stamate, Baogen Shen, Guus Rijnders, and Søren Linderoth.
Metallic and insulating interfaces of amorphous srtio3-based oxide heterostructures.
Nano letters, 11(9):3774–3778, 2011.

[10] ChengJian Li, YanPeng Hong, HongXia Xue, XinXin Wang, Yongchun Li, Kejian Liu, Weimin Jiang, Mingrui Liu, Lin He, RuiFen Dou, et al.
Formation of two-dimensional electron gas at amorphous/crystalline oxide interfaces.
Scientific reports, 8(1):1–9, 2018.

[11] M Salluzzo, JC Cezar, NB Brookes, V Bisogni, GM De Luca, Christoph Richter, Stefan Thiel, Jochen Mannhart, M Huijben, A Brinkman, et al.
Orbital reconstruction and the two-dimensional electron gas at the laalo 3/srtio 3 interface.
Physical review letters, 102(16):166804, 2009.

[12] AEM Smink, JC De Boer, MP Stehno, A Brinkman, WG Van Der Wiel, and H Hilgenkamp.
Gate-tunable band structure of the laalo 3- srti o 3 interface.
Physical review letters, 118(10):106401, 2017.

[13] Arjun Joshua, Sharon Pecker, Jonathan Ruhman, Ehud Altman, and Shahal Ilani.

A universal critical density underlying the physics of electrons at the laalo 3/srtio 3 interface.
Nature communications, 3(1):1–7, 2012.

[14] R Winkler, S Papadakis, E De Poortere, and M Shayegan.
Spin-Orbit Coupling in Two-Dimensional Electron and Hole Systems, volume 41.
Springer, 2003.

[15] Gene Dresselhaus.
Spin-orbit coupling effects in zinc blende structures.
Physical Review, 100(2):580, 1955.

[16] Yua A Bychkov.
Properties of 2d electron gas with lifted spectral degeneracy.
JETP lett., 39(2):78–81, 1984.

[17] AD Caviglia, M Gabay, Stefano Gariglio, Nicolas Reyren, Claudia Cancellieri, and J-M Triscone.
Tunable rashba spin-orbit interaction at oxide interfaces.
Physical review letters, 104(12):126803, 2010.

[18] Younghyun Kim, Roman M Lutchyn, and Chetan Nayak.
Origin and transport signatures of spin-orbit interactions in one-and two-dimensional srtio 3-based heterostructures.
Physical Review B, 87(24):245121, 2013.

[19] PDC King, S McKeown Walker, Anna Tamai, Alberto De La Torre, T Eknapakul, P Buaphet, S-K Mo, W Meevasana, MS Bahramy, and Félix Baumberger.
Quasiparticle dynamics and spin–orbital texture of the srtio 3 two-dimensional electron gas.
Nature communications, 5(1):1–7, 2014.

[20] Stefano Gariglio, M Gabay, and J-M Triscone.
Research update: Conductivity and beyond at the laalo3/srtio3 interface.
APL Materials, 4(6):060701, 2016.

[21] Nicolas Reyren, Stefan Thiel, AD Caviglia, L Fitting Kourkoutis, German Hammerl, Christoph Richter, Christof W Schneider, Thilo Kopp, A-S Rüetschi, Didier Jaccard, et al.
Superconducting interfaces between insulating oxides.
Science, 317(5842):1196–1199, 2007.

[22] AD Caviglia, Stefano Gariglio, Nicolas Reyren, Didier Jaccard, T Schneider, M Gabay, Stefan Thiel, German Hammerl, Jochen Mannhart, and J-M Triscone.
Electric field control of the laalo 3/srtio 3 interface ground state.
Nature, 456(7222):624–627, 2008.

[23] C Bell, S Harashima, Y Kozuka, M Kim, Bog G Kim, Y Hikita, and HY Hwang.
Dominant mobility modulation by the electric field effect at the laalo 3/srtio 3 interface.
Physical review letters, 103(22):226802, 2009.

[24] CH Ahn, A Bhattacharya, M Di Ventra, James N Eckstein, C Daniel Frisbie, ME Gershenson, AM Goldman, IH Inoue, Jochen Mannhart, Andrew J Millis, et al.
Electrostatic modification of novel materials.
Reviews of Modern Physics, 78(4):1185, 2006.

[25] Nicolas Reyren, Stefano Gariglio, AD Caviglia, Didier Jaccard, T Schneider, and J-M Triscone.
Anisotropy of the superconducting transport properties of the laalo 3/srtio 3 interface.
Applied Physics Letters, 94(11):112506, 2009.

[26] Karen Michaeli, Andrew C Potter, and Patrick A Lee.
Superconducting and ferromagnetic phases in srtio 3/laalo 3 oxide interface structures: possibility of finite momentum pairing.
Physical review letters, 108(11):117003, 2012.

[27] Mathias S Scheurer and Jörg Schmalian.

Topological superconductivity and unconventional pairing in oxide interfaces.
Nature communications, 6, 2015.

[28] Florian Loder, Arno P Kampf, and Thilo Kopp.
Route to topological superconductivity via magnetic field rotation.
Scientific reports, 5(1):1–10, 2015.

[29] Yuri Fukaya, Shun Tamura, Keiji Yada, Yukio Tanaka, Paola Gentile, and Mario Cuoco.
Interorbital topological superconductivity in spin-orbit coupled superconductors with inversion symmetry breaking.
Physical Review B, 97(17):174522, 2018.

[30] CA Perroni, V Cataudella, M Salluzzo, M Cuoco, and R Citro.
Evolution of topological superconductivity by orbital-selective confinement in oxide nanowires.
Physical Review B, 100(9):094526, 2019.

[31] Megan Briggeman, Michelle Tomczyk, Binbin Tian, Hyungwoo Lee, Jung-Woo Lee, Yuchi He, Anthony Tylan-Tyler, Mengchen Huang, Chang-Beom Eom, David Pekker, et al.
Pascal conductance series in ballistic one-dimensional laalo3/srtio3 channels.
Science, 367(6479):769–772, 2020.

[32] Lukas Kuerten, Christoph Richter, Narayan Mohanta, Thilo Kopp, Arno Kampf, Jochen Mannhart, and Hans Boschker.
In-gap states in superconducting laalo 3- srtio 3 interfaces observed by tunneling spectroscopy.
Physical Review B, 96(1):014513, 2017.

[33] D Stornaiuolo, D Massarotti, R Di Capua, P Lucignano, GP Pepe, M Salluzzo, and F Tafuri.
Signatures of unconventional superconductivity in the laalo 3/srtio 3 two-dimensional system.
Physical Review B, 95(14):140502, 2017.

[34] Alexander Brinkman, Mark Huijben, M Van Zalk, J Huijben, U Zeitler, JC Maan, Wilfred Gerard van der Wiel, GJHM Rijnders, David HA Blank, and H Hilgenkamp.
Magnetic effects at the interface between non-magnetic oxides.
Nature materials, 6(7):493–496, 2007.

[35] M Ben Shalom, CW Tai, Y Lereah, M Sachs, E Levy, D Rakhmilevitch, A Palevski, and Y Dagan.
Anisotropic magnetotransport at the srtio 3/laalo 3 interface.
Physical Review B, 80(14):140403, 2009.

[36] Lu Li, Christoph Richter, Jochen Mannhart, and RC Ashoori.
Coexistence of magnetic order and two-dimensional superconductivity at laalo 3/srtio 3 interfaces.
Nature physics, 7(10):762–766, 2011.

[37] Felix Gunkel, Chris Bell, Hisashi Inoue, Bongju Kim, Adrian G Swartz, Tyler A Merz, Yasuyuki Hikita, Satoshi Harashima, Hiroki K Sato, Makoto Minohara, et al.
Defect control of conventional and anomalous electron transport at complex oxide interfaces.
Physical Review X, 6(3):031035, 2016.

[38] Julie A Bert, Beena Kalisky, Christopher Bell, Minu Kim, Yasuyuki Hikita, Harold Y Hwang, and Kathryn A Moler.
Direct imaging of the coexistence of ferromagnetism and superconductivity at the laalo 3/srtio 3 interface.
Nature physics, 7(10):767–771, 2011.

[39] Rossitza Pentcheva and Warren E Pickett.
Charge localization or itineracy at la al o 3/ sr ti o 3 interfaces: Hole polarons, oxygen vacancies, and mobile electrons.
Physical Review B, 74(3):035112, 2006.

[40] Gang Chen and Leon Balents.
Ferromagnetism in itinerant two-dimensional t 2 g systems.

Physical review letters, 110(20):206401, 2013.

[41] L Weston, XY Cui, SP Ringer, and C Stampfl.
Density-functional prediction of a surface magnetic phase in srtio 3/laalo 3 heterostructures induced by al vacancies.
Physical review letters, 113(18):186401, 2014.

[42] Natalia Pavlenko, Thilo Kopp, and Jochen Mannhart.
Emerging magnetism and electronic phase separation at titanate interfaces.
Physical Review B, 88(20):201104, 2013.

[43] P. Wittlich, H. Boschker, T. Asaba, L. Li, H. M. L. Noad, C. A. Watson, K. A. Moler, D. Daraselia, D. Japaridze, A. Shengelaya, J. Wang, J. Xia, and J. Mannhart.
Exploring possible ferromagnetism of the $LaAlo_3/SrTio_3$ interface.
Phys. Rev. Materials, 3:104418, Oct 2019.

[44] Øyvind Johansen and Arne Brataas.
Spin pumping and inverse spin hall voltages from dynamical antiferromagnets.
Phys. Rev. B, 95:220408, Jun 2017.
doi: 10.1103/PhysRevB.95.220408.
URL `https://link.aps.org/doi/10.1103/PhysRevB.95.220408`.

[45] Yun-Yi Pai, Anthony Tylan-Tyler, Patrick Irvin, and Jeremy Levy.
Physics of srtio3-based heterostructures and nanostructures: a review.
Reports on Progress in Physics, 81(3):036503, 2018.

[46] H Nakamura and T Kimura.
Electric field tuning of spin-orbit coupling in ktao 3 field-effect transistors.
Physical Review B, 80(12):121308, 2009.

[47] Anil Annadi, Guanglei Cheng, Hyungwoo Lee, Jung-Woo Lee, Shicheng Lu, Anthony Tylan-Tyler, Megan Briggeman, Michelle Tomczyk, Mengchen Huang, David Pekker, et al.
Quantized ballistic transport of electrons and electron pairs in laalo3/srtio3 nanowires.

Nano letters, 18(7):4473–4481, 2018.

[48] Srijit Goswami, Emre Mulazimoglu, Ana MRVL Monteiro, Roman Wölbing, Dieter Koelle, Reinhold Kleiner, Ya M Blanter, Lieven MK Vandersypen, and Andrea D Caviglia.
Quantum interference in an interfacial superconductor.
Nature nanotechnology, 11(10):861–865, 2016.

[49] Felix Trier, Guenevere E. D. K. Prawiroatmodjo, Zhicheng Zhong, Dennis Valbjørn Christensen, Merlin von Soosten, Arghya Bhowmik, Juan Maria García Lastra, Yunzhong Chen, Thomas Sand Jespersen, and Nini Pryds.
Quantization of hall resistance at the metallic interface between an oxide insulator and $srtio_3$.
Phys. Rev. Lett., 117:096804, Aug 2016.

[50] Evgeny Mikheev, Ilan T. Rosen, and David Goldhaber-Gordon.
Quantized critical supercurrent in srtio₃-based quantum point contacts.
Science Advances, 7(40):eabi6520, 2021.
doi: 10.1126/sciadv.abi6520.

[51] Megan Briggeman, Hyungwoo Lee, Jung-Woo Lee, Kitae Eom, François Damanet, Elliott Mansfield, Jianan Li, Mengchen Huang, Andrew J Daley, Chang-Beom Eom, et al.
One-dimensional kronig–penney superlattices at the laalo 3/srtio 3 interface.
Nature Physics, pages 1–6, 2021.

[52] Daniela Stornaiuolo, Stefano Gariglio, NJG Couto, Alexandre Fête, AD Caviglia, Gabriel Seyfarth, Didier Jaccard, AF Morpurgo, and J-M Triscone.
In-plane electronic confinement in superconducting laalo 3/srtio 3 nanostructures.
Applied Physics Letters, 101(22):222601, 2012.

[53] D Massarotti, A Miano, F Tafuri, and D Stornaiuolo.

High efficiency superconducting field effect devices for oxide electronic applications.
Superconductor Science and Technology, 33(3):034007, 2020.

[54] Alexis Jouan, G Singh, Edouard Lesne, DC Vaz, Manuel Bibes, Agnès Barthélémy, Christian Ulysse, Daniela Stornaiuolo, M Salluzzo, Simon Hurand, et al.
Quantized conductance in a one-dimensional ballistic oxide nanodevice.
Nature Electronics, 3(4):201–206, 2020.

[55] SA Wolf, DD Awschalom, RA Buhrman, JM Daughton, von S von Molnár, ML Roukes, A Yu Chtchelkanova, and DM Treger.
Spintronics: a spin-based electronics vision for the future.
science, 294(5546):1488–1495, 2001.

[56] Wei Niu, Xuefeng Wang, Yongbing Xu, and Rong Zhang.
Recent advances on spin-polarized two-dimensional electron gases at oxide interfaces.
ACS Applied Electronic Materials, 3(1):128–144, 2021.

[57] Supriyo Datta and Biswajit Das.
Electronic analog of the electro-optic modulator.
Applied Physics Letters, 56(7):665–667, 1990.

[58] E Lesne, Yu Fu, S Oyarzun, JC Rojas-Sánchez, DC Vaz, H Naganuma, G Sicoli, J-P Attané, M Jamet, E Jacquet, et al.
Highly efficient and tunable spin-to-charge conversion through rashba coupling at oxide interfaces.
Nature materials, 15(12):1261–1266, 2016.

[59] Yi Wang, Rajagopalan Ramaswamy, Mallikarjuna Motapothula, Kulothungasagaran Narayanapillai, Dapeng Zhu, Jiawei Yu, Thirumalai Venkatesan, and Hyunsoo Yang.
Room-temperature giant charge-to-spin conversion at the srtio3–laalo3 oxide interface.
Nano letters, 17(12):7659–7664, 2017.

[60] Felix Trier, Diogo C Vaz, Pierre Bruneel, Paul Noël, Albert Fert, Laurent Vila, Jean-Philippe Attané, Agnès Barthélémy, Marc Gabay, Henri Jaffrès, et al.
Electric-field control of spin current generation and detection in ferromagnet-free srtio3-based nanodevices.
Nano letters, 20(1):395–401, 2019.

[61] Mi-Jin Jin, Seon Young Moon, Jungmin Park, Vijayakumar Modepalli, Junhyeon Jo, Shin-Ik Kim, Hyun Cheol Koo, Byoung-Chul Min, Hyun-Woo Lee, Seung-Hyub Baek, et al.
Nonlocal spin diffusion driven by giant spin hall effect at oxide heterointerfaces.
Nano letters, 17(1):36–43, 2017.

[62] Paul Noël, Felix Trier, Luis M Vicente Arche, Julien Bréhin, Diogo C Vaz, Vincent Garcia, Stéphane Fusil, Agnès Barthélémy, Laurent Vila, Manuel Bibes, et al.
Non-volatile electric control of spin–charge conversion in a srtio 3 rashba system.
Nature, 580(7804):483–486, 2020.

[63] Sasikanth Manipatruni, Dmitri E Nikonov, Chia-Ching Lin, Tanay A Gosavi, Huichu Liu, Bhagwati Prasad, Yen-Lin Huang, Everton Bonturim, Ramamoorthy Ramesh, and Ian A Young.
Scalable energy-efficient magnetoelectric spin–orbit logic.
Nature, 565(7737):35–42, 2019.

[64] Bernard et al. Dieny.
Opportunities and challenges for spintronics in the microelectronic industry.
Nature Electronics, 3:446, August 2020.
doi: 10.1038/s41928-020-0461-5.
URL `https://hal.archives-ouvertes.fr/hal-02917378`.
Review written by the SpinFactory European Consortium.

[65] Atsufumi Hirohata, Keisuke Yamada, Yoshinobu Nakatani, Ioan-Lucian Prejbeanu, Bernard Diény, Philipp Pirro, and Burkard Hillebrands.

Review on spintronics: Principles and device applications.
Journal of Magnetism and Magnetic Materials, 509:166711, 2020.
ISSN 0304-8853.
doi: https://doi.org/10.1016/j.jmmm.2020.166711.
URL https://www.sciencedirect.com/science/article/pii/S0304885320302353.

[66] A. Manchon, H. C. Koo, J. Nitta, S. M. Frolov, and R. A. Duine.
New perspectives for rashba spin-orbit coupling.
Nature Materials, 14(9):871–882, August 2015.
ISSN 1476-1122.
doi: 10.1038/nmat4360.
Copyright: Copyright 2017 Elsevier B.V., All rights reserved.

[67] Lior Kornblum.
Conductive oxide interfaces for field effect devices.
Advanced Materials Interfaces, 6(15):1900480, 2019.

[68] Lu Chen, Erin Sutton, Hyungwoo Lee, Jung-Woo Lee, Jianan Li, Chang-Beom Eom, Patrick Irvin, and Jeremy Levy.
Over 100-thz bandwidth selective difference frequency generation at laalo 3/srtio 3 nanojunctions.
Light: Science & Applications, 8(1):1–7, 2019.

[69] Weitao Dai, Yi Liang, Ming Yang, Dustin Schrecongost, Prakash Gajurel, Hyungwoo Lee, Jung-Woo Lee, Jun Chen, Chang-Beom Eom, and Cheng Cen.
Large and reconfigurable infrared photothermoelectric effect at oxide interfaces.
Nano letters, 19(10):7149–7154, 2019.

[70] R Di Capua, M Verma, M Radovic, VN Strocov, C Piamonteze, EB Guedes, N Plumb, Yu Chen, M d'Antuono, GM De Luca, et al.
Orbital selective switching of ferromagnetism in an oxide quasi two-dimensional electron gas.

arXiv preprint arXiv:2109.06138, 2021.

[71] GM De Luca, R Di Capua, E Di Gennaro, F Miletto Granozio, D Stornaiuolo, M Salluzzo, A Gadaleta, I Pallecchi, D Marrè, C Piamonteze, et al.
Transport properties of a quasi-two-dimensional electron system formed in $laalo_3/eutio_3/srtio_3$ heterostructures.
Physical Review B, 89(22):224413, 2014.

[72] Daniela Stornaiuolo, C Cantoni, GM De Luca, R Di Capua, E Di Gennaro, G Ghiringhelli, Benoit Jouault, D Marrè, D Massarotti, F Miletto Granozio, et al.
Tunable spin polarization and superconductivity in engineered oxide interfaces.
Nature materials, 15(3):278–283, 2016.

[73] TR McGuire, MW Shafer, RJ Joenk, HA Alperin, and SJ Pickart.
Magnetic structure of eutio3.
Journal of Applied Physics, 37(3):981–982, 1966.

[74] A Bussmann-Holder, J Köhler, RK Kremer, and JM Law.
Relation between structural instabilities in eutio 3 and srtio 3.
Physical Review B, 83(21):212102, 2011.

[75] D Bessas, KZ Rushchanskii, M Kachlik, S Disch, O Gourdon, J Bednarcik, K Maca, I Sergueev, S Kamba, M Ležaić, et al.
Lattice instabilities in bulk eutio 3.
Physical Review B, 88(14):144308, 2013.

[76] Takuro Katsufuji and H Takagi.
Coupling between magnetism and dielectric properties in quantum paraelectric eutio 3.
Physical Review B, 64(5):054415, 2001.

[77] Jason Schiemer, Leszek J Spalek, Siddharth S Saxena, Christos Panagopoulos, Takuro Katsufuji, Annette Bussmann-Holder, Jürgen Köhler, and Michael A Carpenter.

Magnetic field and in situ stress dependence of elastic behavior in eutio 3 from resonant ultrasound spectroscopy.
Physical Review B, 93(5):054108, 2016.

[78] M Salluzzo, Stefano Gariglio, Daniela Stornaiuolo, V Sessi, S Rusponi, C Piamonteze, GM De Luca, M Minola, D Marré, A Gadaleta, et al.
Origin of interface magnetism in bimno 3/srtio 3 and laalo 3/srtio 3 heterostructures.
Physical Review Letters, 111(8):087204, 2013.

[79] Naoto Nagaosa, Jairo Sinova, Shigeki Onoda, Allan H MacDonald, and Nai Phuan Ong.
Anomalous hall effect.
Reviews of modern physics, 82(2):1539, 2010.

[80] Emerson M Pugh.
Hall effect and the magnetic properties of some ferromagnetic materials.
Physical Review, 36(9):1503, 1930.

[81] EM Pugh and TW Lippert.
Hall emf and intensity of magnetization.
Physical Review, 42(5):709, 1932.

[82] J Smit.
The spontaneous hall effect in ferromagnetics i.
Physica, 21(6-10):877–887, 1955.

[83] Jan Smit.
The spontaneous hall effect in ferromagnetics ii.
Physica, 24(1-5):39–51, 1958.

[84] Luc Berger.
Side-jump mechanism for the hall effect of ferromagnets.
Physical Review B, 2(11):4559, 1970.

[85] Robert Karplus and JM Luttinger.
Hall effect in ferromagnetics.

Physical Review, 95(5):1154, 1954.

[86] T Jungwirth, Qian Niu, and AH MacDonald.
Anomalous hall effect in ferromagnetic semiconductors.
Physical review letters, 88(20):207208, 2002.

[87] FDM Haldane.
Berry curvature on the fermi surface: Anomalous hall effect as a topological fermi-liquid property.
Physical review letters, 93(20):206602, 2004.

[88] Shigeki Onoda, Naoyuki Sugimoto, and Naoto Nagaosa.
Quantum transport theory of anomalous electric, thermoelectric, and thermal hall effects in ferromagnets.
Phys. Rev. B, 77:165103, Apr 2008.
doi: 10.1103/PhysRevB.77.165103.
URL `https://link.aps.org/doi/10.1103/PhysRevB.77.165103`.

[89] NA Sinitsyn, AH MacDonald, T Jungwirth, VK Dugaev, and Jairo Sinova.
Anomalous hall effect in a two-dimensional dirac band: The link between the kubo-streda formula and the semiclassical boltzmann equation approach.
Physical Review B, 75(4):045315, 2007.

[90] NA Sinitsyn.
Semiclassical theories of the anomalous hall effect.
Journal of Physics: Condensed Matter, 20(2):023201, 2007.

[91] Adeline Crépieux and Patrick Bruno.
Theory of the anomalous hall effect from the kubo formula and the dirac equation.
Physical Review B, 64(1):014416, 2001.

[92] Shigeki Onoda, Naoyuki Sugimoto, and Naoto Nagaosa.
Theory of non-equilibirum states driven by constant electromagnetic fields: —non-commutative quantum mechanics in the keldysh formalism—.
Progress of theoretical physics, 116(1):61–86, 2006.

[93] Kei S Takahashi, Hiroaki Ishizuka, Tomoki Murata, Qing Y Wang, Yoshinori Tokura, Naoto Nagaosa, and Masashi Kawasaki.
Anomalous hall effect derived from multiple weyl nodes in high-mobility eutio3 films.
Science advances, 4(7):eaar7880, 2018.

[94] D Stornaiuolo, Benoit Jouault, E Di Gennaro, A Sambri, M d'Antuono, D Massarotti, F Miletto Granozio, R Di Capua, GM De Luca, GP Pepe, et al.
Interplay between spin-orbit coupling and ferromagnetism in magnetotransport properties of a spin-polarized oxide two-dimensional electron system.
Physical Review B, 98(7):075409, 2018.

[95] Gerd Bergmann.
Weak localization in thin films: a time-of-flight experiment with conduction electrons.
Physics Reports, 107(1):1–58, 1984.

[96] SV Iordanskii, Yu B Lyanda-Geller, and GE Pikus.
Weak localization in quantum wells with spin-orbit interaction.
ZhETF Pisma Redaktsiiu, 60:199, 1994.

[97] D. Stornaiuolo, S. Gariglio, A. Fête, M. Gabay, D. Li, D. Massarotti, and J.-M. Triscone.
Weak localization and spin-orbit interaction in side-gate field effect devices at the $laalo_3/srtio_3$ interface.
Phys. Rev. B, 90:235426, Dec 2014.

[98] Sumilan Banerjee, Onur Erten, and Mohit Randeria.
Ferromagnetic exchange, spin–orbit coupling and spiral magnetism at the laalo 3/srtio 3 interface.
Nature physics, 9(10):626–630, 2013.

[99] Dennis Valbjørn Christensen, Felix Trier, Wei Niu, Yulin Gan, Yu Zhang, Thomas Sand Jespersen, Yunzhong Chen, and Nini Pryds.
Stimulating oxide heterostructures: A review on controlling srtio3-based heterointerfaces with external stimuli.

Advanced Materials Interfaces, 6(21):1900772, 2019.

[100] Daniela Stornaiuolo, Stefano Gariglio, Alexandre Fete, M Gabay, Danfeng Li, D Massarotti, and J-M Triscone.
Weak localization and spin-orbit interaction in side-gate field effect devices at the laalo 3/srtio 3 interface.
Physical Review B, 90(23):235426, 2014.

[101] B Förg, Christoph Richter, and Jochen Mannhart.
Field-effect devices utilizing laalo3-srtio3 interfaces.
Applied Physics Letters, 100(5):053506, 2012.

[102] T Sakudo and H Unoki.
Dielectric properties of srti o 3 at low temperatures.
Physical review letters, 26(14):851, 1971.

[103] Srijit Goswami, Emre Mulazimoglu, Lieven MK Vandersypen, and Andrea D Caviglia.
Nanoscale electrostatic control of oxide interfaces.
Nano Letters, 15(4):2627–2632, 2015.

[104] Masayuki Hosoda, Yasuyuki Hikita, Harold Y Hwang, and Christopher Bell.
Transistor operation and mobility enhancement in top-gated laalo3/srtio3 heterostructures.
Applied Physics Letters, 103(10):103507, 2013.

[105] Wei Liu, Stefano Gariglio, Alexandre Fête, Danfeng Li, Margherita Boselli, Daniela Stornaiuolo, and J-M Triscone.
Magneto-transport study of top-and back-gated laalo3/srtio3 heterostructures.
APL materials, 3(6):062805, 2015.

[106] S Hurand, A Jouan, C Feuillet-Palma, G Singh, J Biscaras, E Lesne, N Reyren, Alain Barthélémy, M Bibes, JE Villegas, et al.
Field-effect control of superconductivity and rashba spin-orbit coupling in top-gated laalo 3/srtio 3 devices.
Scientific reports, 5(1):1–9, 2015.

[107] Shengwei Zeng, Weiming Lu, Zhen Huang, Zhiqi Liu, Kun Han, Kalon Gopinadhan, Changjian Li, Rui Guo, Wenxiong Zhou, Haijiao Harsan Ma, et al.
Liquid-gated high mobility and quantum oscillation of the two-dimensional electron gas at an oxide interface.
ACS nano, 10(4):4532–4537, 2016.

[108] Christof W Schneider, Stefan Thiel, German Hammerl, Christoph Richter, and Jochen Mannhart.
Microlithography of electron gases formed at interfaces in oxide heterostructures.
Applied physics letters, 89(12):122101, 2006.

[109] C Woltmann, T Harada, H Boschker, V Srot, PA Van Aken, H Klauk, and J Mannhart.
Field-effect transistors with submicrometer gate lengths fabricated from laalo 3- srtio 3-based heterostructures.
Physical Review Applied, 4(6):064003, 2015.

[110] Rainer Jany, Christoph Richter, Carsten Woltmann, Georg Pfanzelt, Benjamin Förg, Marcus Rommel, Thomas Reindl, Ulrike Waizmann, Jürgen Weis, Julia A Mundy, et al.
Monolithically integrated circuits from functional oxides.
Advanced Materials Interfaces, 1(1):1300031, 2014.

[111] Pier Paolo Aurino, Alexey Kalabukhov, Nikolina Tuzla, Eva Olsson, Tord Claeson, and Dag Winkler.
Nano-patterning of the electron gas at the laalo3/srtio3 interface using low-energy ion beam irradiation.
Applied Physics Letters, 102(20):201610, 2013.

[112] Pier Paolo Aurino, A Kalabukhov, Nikolina Tuzla, Eva Olsson, A Klein, Paul Erhart, YA Boikov, IT Serenkov, VI Sakharov, Tord Claeson, et al.
Reversible metal-insulator transition of ar-irradiated laal o 3/srti o 3 interfaces.

Physical Review B, 92(15):155130, 2015.

[113] Cheng Cen, Stefan Thiel, German Hammerl, Christof W Schneider, KE Andersen, C Stephen Hellberg, Jochen Mannhart, and J Levy.
Nanoscale control of an interfacial metal–insulator transition at room temperature.
Nature materials, 7(4):298–302, 2008.

[114] Mengchen Huang, Feng Bi, Sangwoo Ryu, Chang-Beom Eom, Patrick Irvin, and Jeremy Levy.
Direct imaging of laalo3/srtio3 nanostructures using piezoresponse force microscopy.
APL Materials, 1(5):052110, 2013.

[115] M D'Antuono, A Kalaboukhov, R Caruso, S Wissberg, S Weitz Sobelman, B Kalisky, G Ausanio, M Salluzzo, and D Stornaiuolo.
Nanopatterning of oxide 2-dimensional electron systems using low-temperature ion milling.
Nanotechnology, 33(8):085301, 2021.

[116] Daisuke Kan, Takahito Terashima, Ryoko Kanda, Atsunobu Masuno, Kazunori Tanaka, Shucheng Chu, Hirofumi Kan, Atsushi Ishizumi, Yoshihiko Kanemitsu, Yuichi Shimakawa, et al.
Blue-light emission at room temperature from ar+-irradiated srtio 3.
Nature materials, 4(11):816–819, 2005.

[117] D Stornaiuolo, G Rotoli, D Massarotti, F Carillo, L Longobardi, F Beltram, and F Tafuri.
Resolving the effects of frequency-dependent damping and quantum phase diffusion in yba 2 cu 3 o 7- x josephson junctions.
Physical Review B, 87(13):134517, 2013.

[118] A Fragneto, GM De Luca, R Di Capua, U Scotti di Uccio, M Salluzzo, X Torrelles, Tien-Lin Lee, and J Zegenhagen.
Ti-and sr-rich surfaces of sr ti o 3 studied by grazing incidence x-ray diffraction.

Applied Physics Letters, 91(10):101910, 2007.

[119] M Salluzzo, Stefano Gariglio, X Torrelles, Zoran Ristic, R Di Capua, J Drnec, M Moretti Sala, G Ghiringhelli, R Felici, and NB Brookes.
Structural and electronic reconstructions at the laalo3/srtio3 interface.
Advanced Materials, 25(16):2333–2338, 2013.

[120] Beena Kalisky, Eric M Spanton, Hilary Noad, John R Kirtley, Katja C Nowack, Christopher Bell, Hiroki K Sato, Masayuki Hosoda, Yanwu Xie, Yasuyuki Hikita, et al.
Locally enhanced conductivity due to the tetragonal domain structure in laalo 3/srtio 3 heterointerfaces.
Nature materials, 12(12):1091–1095, 2013.

[121] Eylon Persky and Beena Kalisky.
Scanning squid view of oxide interfaces.
Advanced Materials, 30(41):1706653, 2018.

[122] Dennis V Christensen, Merlin von Soosten, Felix Trier, Thomas S Jespersen, Anders Smith, Yunzhong Chen, and Nini Pryds.
Controlling the carrier density of srtio3-based heterostructures with annealing.
Advanced Electronic Materials, 3(8):1700026, 2017.

[123] MZ Minhas, HH Blaschek, F Heyroth, and G Schmidt.
Sidewall depletion in nano-patterned lao/sto heterostructures.
Aip Advances, 6(3):035002, 2016.

[124] B. Müller, M. Karrer, F. Limberger, M. Becker, B. Schröppel, C.J. Burkhardt, R. Kleiner, E. Goldobin, and D. Koelle.
Josephson junctions and squids created by focused helium-ion-beam irradiation of $yba_2cu_3o_7$.
Phys. Rev. Applied, 11:044082, Apr 2019.

[125] KX Jin, W Lin, BC Luo, and Tao Wu.
Photoinduced modulation and relaxation characteristics in laalo 3/srtio 3 heterointerface.

Scientific reports, 5(1):1–6, 2015.

[126] Antonello Tebano, Emiliana Fabbri, Daniele Pergolesi, Giuseppe Balestrino, and Enrico Traversa.
Room-temperature giant persistent photoconductivity in srtio3/laalo3 heterostructures.
Acs Nano, 6(2):1278–1283, 2012.

[127] VK Guduru, A Granados del Aguila, Sander Wenderich, MK Kruize, A McCollam, PCM Christianen, U Zeitler, Alexander Brinkman, G Rijnders, H Hilgenkamp, et al.
Optically excited multi-band conduction in laalo3/srtio3 heterostructures.
Applied physics letters, 102(5):051604, 2013.

[128] Long Cheng, Laiming Wei, Haixing Liang, Yuedong Yan, Guanghui Cheng, Meng Lv, Tie Lin, Tingting Kang, Guolin Yu, Junhao Chu, et al.
Optical manipulation of rashba spin–orbit coupling at srtio3-based oxide interfaces.
Nano letters, 17(11):6534–6539, 2017.

[129] A Rastogi, JJ Pulikkotil, S Auluck, Z Hossain, and RC Budhani.
Photoconducting state and its perturbation by electrostatic fields in oxide-based two-dimensional electron gas.
Physical Review B, 86(7):075127, 2012.

[130] Emiliano Di Gennaro, Umberto Scotti di Uccio, Carmela Aruta, Claudia Cantoni, Alessandro Gadaleta, Andrew R Lupini, Davide Maccariello, Daniele Marré, Ilaria Pallecchi, Domenico Paparo, et al.
Persistent photoconductivity in 2d electron gases at different oxide interfaces.
Advanced Optical Materials, 1(11):834–843, 2013.

[131] Hong-Liang Lu, Liang Zhang, Xiu-Mei Ma, Gui-Jun Lian, Jin-Bo Yang, Da-Peng Yu, and Zhi-Min Liao.
Photoelectrical properties of insulating laalo 3–srtio 3 interfaces.
Nanoscale, 6(2):736–740, 2014.

[132] Marianne C Tarun, Farida A Selim, and Matthew D McCluskey.
Persistent photoconductivity in strontium titanate.
Physical Review Letters, 111(18):187403, 2013.

[133] Giovanni Drera, Francesco Banfi, F Federici Canova, P Borghetti, L Sangaletti, F Bondino, E Magnano, J Huijben, Mark Huijben, G Rijnders, et al.
Spectroscopic evidence of in-gap states at the srtio 3/laalo 3 ultrathin interfaces.
Applied physics letters, 98(5):052907, 2011.

[134] Z Ristic, R Di Capua, F Chiarella, GM De Luca, I Maggio-Aprile, M Radovic, and M Salluzzo.
Photodoping and in-gap interface states across the metal-insulator transition in laalo 3/srtio 3 heterostructures.
Physical Review B, 86(4):045127, 2012.

[135] HJ Queisser and DE Theodorou.
Decay kinetics of persistent photoconductivity in semiconductors.
Physical Review B, 33(6):4027, 1986.

[136] Hong Yan, Zhaoting Zhang, Shuanhu Wang, and Kexin Jin.
Review of photoresponsive properties at srtio3-based heterointerfaces.
Chinese Physics B, 27(11):117804, 2018.

[137] Hong-Liang Lu, Zhi-Min Liao, Liang Zhang, Wen-Tao Yuan, Yong Wang, Xiu-Mei Ma, and Da-Peng Yu.
Reversible insulator-metal transition of laalo 3/srtio 3 interface for nonvolatile memory.
Scientific reports, 3(1):1–6, 2013.

[138] Alexandre Fête, Stefano Gariglio, AD Caviglia, J-M Triscone, and M Gabay.
Rashba induced magnetoconductance oscillations in the laalo 3-srtio 3 heterostructure.
Physical Review B, 86(20):201105, 2012.

[139] Manuel Bibes, Javier E Villegas, and Agnes Barthelemy.
Ultrathin oxide films and interfaces for electronics and spintronics.
Advances in Physics, 60(1):5–84, 2011.

[140] M Bibes, N Reyren, E Lesne, J-M George, C Deranlot, S Collin, A Barthélémy, and H Jaffrès.
Towards electrical spin injection into laalo3–srtio3.
Philosophical Transactions of the Royal Society A: Mathematical, Physical and Engineering Sciences, 370(1977):4958–4971, 2012.

[141] Julian P Velev, Kirill D Belashchenko, Derek A Stewart, Mark van Schilfgaarde, SS Jaswal, and Evgeny Y Tsymbal.
Negative spin polarization and large tunneling magnetoresistance in epitaxial co| srtio 3| co magnetic tunnel junctions.
Physical review letters, 95(21):216601, 2005.

[142] Wenxu Zhang, Qiuru Wang, Bin Peng, Huizhong Zeng, Wee Tee Soh, Chong Kim Ong, and Wanli Zhang.
Spin galvanic effect at the conducting srtio3 surfaces.
Applied Physics Letters, 109(26):262402, 2016.

[143] Diogo C Vaz, Paul Noël, Annika Johansson, Börge Göbel, Flavio Y Bruno, Gyanendra Singh, Siobhan Mckeown-Walker, Felix Trier, Luis M Vicente-Arche, Anke Sander, et al.
Mapping spin–charge conversion to the band structure in a topological oxide two-dimensional electron gas.
Nature materials, 18(11):1187–1193, 2019.

[144] Huaiwen Yang, Boyu Zhang, Xueying Zhang, Xi Yan, Wenlong Cai, Yinglin Zhao, Jirong Sun, Kang L Wang, Dapeng Zhu, and Weisheng Zhao.
Giant charge-to-spin conversion efficiency in sr ti o 3-based electron gas interface.
Physical Review Applied, 12(3):034004, 2019.

[145] Mi-Jin Jin, Doo-Seung Um, Kohei Ohnishi, Sachio Komori, Nadia Stelmashenko, Daeseong Choe, Jung-Woo Yoo, and Jason WA Robinson.

Pure spin currents driven by colossal spin–orbit coupling on two-dimensional surface conducting srtio3.
Nano Letters, 21(15):6511–6517, 2021.

[146] Yumeng Yang, Ziyan Luo, Haijun Wu, Yanjun Xu, Run-Wei Li, Stephen J Pennycook, Shufeng Zhang, and Yihong Wu.
Anomalous hall magnetoresistance in a ferromagnet.
Nature communications, 9(1):1–9, 2018.

[147] Vasfi Burak Özdöl, Vesna Srot, and Peter A van Aken.
Sample preparation techniques for transmission electron microscopy.
Handbook of Nanoscopy, pages 473–498, 2012.

[148] Gertjan Koster, Boike L Kropman, Guus JHM Rijnders, Dave HA Blank, and Horst Rogalla.
Quasi-ideal strontium titanate crystal surfaces through formation of strontium hydroxide.
Applied Physics Letters, 73(20):2920–2922, 1998.